Classical and Quantum Chaos in Spin Glass Shards Models

Classical and Quantum Chaos in Spin Glass Shards Models

Master thesis

for the purpose of obtaining the degree of Master of Science
at Delft University of Technology to be defended publicly on
Tuesday January 6th at 13:30 o'clock

by

Emiel Huisman

Student number:	5135591
Master programme:	Applied Physics
Specialisation:	Physics for Quantum Devices and Quantum Computing
Faculty:	Applied Sciences
Thesis committee:	Dr. V.V. Dobrovitski
	Dr. B. Janssens
	Prof. dr. A.F. Otte

For Pleun (of course)

CONTENTS

ABSTRACT

We study how global system parameters and local realizations of quenched disorder shape the dynamics of a classical many-body spin system and how classical indicators of chaos, Lyapunov's exponents, relate to quantum signatures of chaos. In particular, we focus on the classical analogue of the quantum spin glass shards model in a random transverse magnetic field studied by Georgeot and Shepelyansky. The classical spin phase space is constructed as a symplectic manifold and we evolve trajectories with a second-order Suzuki–Trotter integrator. This symplectic structure-preserving scheme enables reliable computation of Lyapunov's exponents via standard repeated QR-based orthogonalization of tangent vectors, yielding accurate finite-time Lyapunov spectra for trajectories in different regions of phase space.

Using these tools, we examine the dynamics of trajectories sampled from different regions of phase space while varying two global system parameters: the relative strength of the spin-spin coupling and the transverse magnetic field. We find that both the strong spin-spin coupling and strong magnetic field limits are nearly integrable, with maximal chaos emerging at intermediate coupling–field ratios. When initial spin configurations are sampled uniformly over the Bloch sphere, different disorder realizations do not qualitatively change whether dynamics are chaotic or integrable, while configurations concentrated near the x- or z-axis are highly sensitive to the specific disorder realization and can exhibit either almost fully integrable or strongly chaotic behavior under identical global parameters.

For 17 spins, all observed trajectories in the classical system are chaotic when the spin-spin coupling is approximately three times stronger than the transverse field. A comparison with the quantum level-spacing statistics of the corresponding quantum model shows qualitative agreement regarding which choices of global parameters lead to integrable or chaotic dynamics. However, there is a quantitative mismatch in which global parameter values produce the strongest chaotic dynamics. This demonstrates that the relationship between classical Lyapunov exponents and quantum energy-level spacing statistics is complex and non-trivial.

1

INTRODUCTION

Many foundational subjects in statistical physics can be formulated within the framework of classical Hamiltonian dynamics [Khi49; Tol38], and a central one is:

"*Under what conditions on the microscopic Hamiltonian dynamics does the long-time values of macroscopic observables coincide with the predictions of equilibrium statistical ensembles?*"

Statistical physics assumes that equilibrium values of physical observables are obtained as averages over an appropriate statistical ensemble, such as the microcanonical ensemble [LL80]. Thermalization refers to this process by which, after some time, the values of macroscopic observables relax to stationary values that can be described by an equilibrium ensemble, and become essentially independent of the detailed initial conditions, except through conserved quantities such as energy [Rei08]. The justification for this process is given by the ergodic hypothesis, which assumes that a Hamiltonian system evolves so that a typical trajectory effectively explores the whole constant-energy surface in phase space, spending time in each region in proportion to the total available phase-space. Since Hamiltonian dynamics preserves phase-space volume, this implies that the infinite-time average of any reasonable observable coincides with its microcanonical ensemble average [Khi49].

Nonlinearity is generally associated with more complex dynamical behavior: individual solutions no longer combine by simple superposition, and small perturbations of the initial conditions can lead to large differences in the long-time evolution, as illustrated by the standard (Chirikov–Taylor) map [Zas07]. By contrast, in a linear system any solution can be written as a sum of independent solutions that evolve without influencing one another, so the motion generally remains periodic or quasi-periodic and typically explores only a restricted region of the energy shell in phase space. With this perspective, Fermi, Pasta, Ulam, and Tsingou (FPUT) designed their famous experiment to test whether introducing weak nonlinearities would be sufficient to drive a many-body system toward equilibrium [Fer+55]. Instead, they observed long-lived quasiperiodic dynamics and a lack of energy equipartition. This unexpected result triggered a substantial body of subsequent work, reshaping our understanding of thermalization and leading to major developments in statistical physics and nonlinear dynamics [For92; Gal08].

A major conceptual advance in understanding such observations came with the development of Kolmogorov–Arnold–Moser (KAM) theory [Arn63; Kol54; Mos62]. KAM theory shows that, for Hamiltonian systems that are small perturbations of integrable ones, a large measure of invariant tori survives, carrying quasiperiodic motion with slightly deformed frequencies. As a consequence, the phase-space dynamics can remain largely confined, and energy exchange between different degrees of freedom is absent, even in the presence of nonlinearity. This provides a explanation for the persistence of quasiperiodic behaviour and the lack of

equipartition seen in the FPUT experiment, and offers one possible answer to why weakly nonlinear many-body systems may fail to thermalize on certain time scales [BP23].

In the quantum setting, the situation is even more subtle. The underlying quantum dynamics are linear and do not exhibit sensitive dependence on initial conditions in the classical sense, so the usual trajectory-based notion of chaos is not applicable. As a result, there is no universally accepted, dynamical definition of quantum chaos. Instead, one characterizes quantum systems as chaotic or integrable through indirect signatures, such as random-matrix energy-level statistics, properties of eigenstates, or the growth of certain correlation functions [Haa10]. These developments have led to a rich theory of quantum chaos that parallels, but also fundamentally differs from, the classical picture based on nonlinear equations of motion and invariant structures in phase space [Gha+20; GMW98; Stö99].

There remain, however, important conceptual links between classical and quantum chaos and, more broadly, between dynamical systems and ergodic theory. Spectral statistics of quantum systems retain imprints of the underlying classical phase-space structure: integrable classical dynamics is typically associated with Poissonian energy-level statistics, as conjectured by Berry and Tabor [BT77a], whereas classically chaotic, ergodic dynamics is associated with Wigner–Dyson statistics as in random-matrix theory. This correspondence is encapsulated in the Berry–Tabor conjecture for integrable systems and the Bohigas–Giannoni–Schmit conjecture for fully chaotic systems [BGS84], which together postulate that quantum systems inherit spectral statistics from the nature of their underlying classical dynamics. However, explicit counterexamples to both conjectures have been constructed [Bar+08; BSS92]. The stated conjectures about the link between classical dynamics and quantum spectral statistics can therefore no longer be regarded as universally valid, but rather as characterizations in suitably generic systems.

In this thesis, we examine this link between chaos in a classical and quantum system by focusing on a concrete classical and quantum many-body model: the spin glass shards in a random transverse magnetic field studied by Georgeot and Shepelyansky [GS98]. In this model, the microscopic couplings are drawn from a random distribution, so each realization corresponds to a specific choice of local interactions, while the overall behavior is governed by a smaller set of global control parameters, such as the strength of the transverse field and the distribution of couplings. By tuning these global parameters, the system exhibits a crossover in its energy-level spacing statistics from Poissonian behavior, characteristic of integrable or weakly interacting regimes, to Wigner–Dyson behavior, which are indicators of quantum chaos and strong level repulsion. Our strategy is to construct and simulate the corresponding classical Hamiltonian system, generating the same disordered structure at the local level, and to examine whether its phase-space dynamics shows a similar transition, for example from quasi-integrable motion to strongly chaotic. For this purpose, we compute the Lyapunov exponents of the classical dynamics and compare their behavior across different disorder realizations and different choices of the global control parameters, using the methods introduced in [Ben+80a; Ben+80b]. By comparing these exponents with the quantum spectral statistics across many realizations of disorder, we aim to identify how changing the global control parameters and the local disorder affects both the onset of Wigner–Dyson statistics in the quantum system and the onset of strong classical chaos in the classical system, as reflected in the Lyapunov exponents, and to identify regions in phase space that are effectively integrable or chaotic and how these regions are influenced by the system parameters.

This thesis is organized as follows. In Chapter 2, we introduce several examples of classical determistic Hamiltonian chaos, such as the kicked rotator, the Fermi–Pasta–Ulam–Tsingou chain, classical limaçon billiards, and classical spin-chain models, and use them to illustrate how integrable and chaotic dynamics emerge in the classical regime. Chapter 3 then reviews several signatures of quantum chaos, level-spacing statistics and Loschmidt echoes, reviews the quantum limaçon billiards model, and introduces the quantum spin glass shards model whose classical analogue we research for the remainder of the thesis. In Chapter 4, we develop the geometric formulation of classical spin dynamics as Hamiltonian flows on a symplectic manifold, introduce the second-order Suzuki-Trotter integrator and present the numerical framework for computing Lyapunov spectra in classical spin systems. Chapter 5 applies this framework to the classical spin glass shards model we research, validates the numerical implementation, and analyzes Lyapunov spectra for individual trajectories, phase space ensembles, and quenched disorder realizations as functions of the spin-spin coupling and transverse magnetic field strength. Finally, Chapter 6 discusses the implications of these results and the observed relation between classical and quantum chaos in spin glass shards, while Chapter 7 summarizes the main conclusions and outlines possible directions for future work.

2

CLASSICAL CHAOS

Whether a classical Hamiltonian system is integrable or chaotic controls how a system explores its phase space and therefore whether it thermalizes in the way statistical mechanics assumes [Khi49; Tol38]. Integrable systems have many conserved quantities and confined motions. Chaotic systems, by contrast, exhibit sensitive dependence on initial conditions and strong mixing, which underpins ergodicity and the emergence of standard thermodynamic behavior. This distinction between chaos and integrability is central for understanding when and whether a system will thermalize.

Formally, a Hamiltonian system with N degrees of freedom is defined by N pairs of generalised coordinates $(q_1, \dots, q_N)$ and momentums $(p_1, \dots p_N)$ together with a Hamiltonian function $H(p, q) \equiv H(p_1, q_1, \dots, p_N, q_N)$ [Zas07, Section 1.1]. These satisfy the Hamiltonian equations of motion

$$\dot{p}_i = -\frac{\partial H}{\partial q_i}, \quad \dot{q}_i = \frac{\partial H}{\partial p_i}, \quad (i = 1, \dots, N).$$

We will (optionally) consider Hamiltonian functions that depend on time and are time-periodic with period $T = 2\pi/\nu$. That is,

$$H(p, q; t + T) = H(p, q; t). \tag{2.1}$$

Due to the time variable being an additional canonical variable we define the system (2.1) as having $N + 1/2$ degrees of freedom.

For a Hamiltonian system $H(p_1, q_1; t)$ with $1 + 1/2$ degrees of freedom, one canonical pair (q_1, p_1) and an explicit periodic time dependence with period T, it is convenient to describe the dynamics using a Poincaré map. Instead of following the continuous-time trajectory $(p_1(t), q_1(t))$, we record its state at discrete times

$$t_n = t_0 + nT, \qquad n \in \mathbb{N},$$

that is, once every driving period. The Poincaré map then sends the phase-space point at time t_n to the one at time t_{n+1}, and the trajectory is represented in the two-dimensional phase plane by the sequence of points

$$\big(p_1(t_n), q_1(t_n)\big).$$

In this way, the continuous Hamiltonian flow is reduced to an area-preserving map on the (p_1, q_1) plane. Intuitively, one may think of this as taking stroboscopic snapshots of the system.

Even for such low-dimensional systems, the Poincaré map can display a rich mixture of dynamical behaviors, such as invariant curves corresponding to integrable motion coexist and scattered points filling regions associated with chaotic trajectories.

To distinguish between integrable and chaotic regions, we compute Lyapunov's exponents, which measure the mean exponential rate at which nearby trajectories separate. For a periodically driven Hamiltonian system with $1+1/2$ degrees of freedom, the stroboscopic dynamics are described by a two-dimensional Poincaré map

$$z_{n+1} = F(z_n), \qquad z_n = (p_1(t_n), q_1(t_n)) \in \mathbb{R}^2,$$

which is area-preserving. Equivalently, its Jacobian satisfies $\det DF(z) = 1$ for all z. As a consequence, the two Lyapunov's exponents of the map, λ_+ and λ_-, must sum to zero and therefore occur as a pair

$$\{\lambda_+, \lambda_-\} = \{\lambda, -\lambda\}.$$

Here $\lambda > 0$ measures the mean exponential rate at which nearby trajectories separate along the most unstable direction, while $-\lambda$ describes the compensating contraction along a transverse direction required by area preservation.

To make this precise, consider two nearby initial conditions z_0 and $z_0 + \delta z_0$, where $\delta z_0 \neq 0$ is infinitesimal. Linearizing the map around z_0 gives

$$F(z_0 + \delta z_0) \approx F(z_0) + DF(z_0)\,\delta z_0,$$

so after one iteration the deviation evolves as $\delta z_1 \approx DF(z_0)\delta z_0$. Iterating these linearized dynamics yields

$$\delta z_n \approx DF(z_{n-1}) \cdots DF(z_1)\,DF(z_0)\,\delta z_0 \equiv M_n\,\delta z_0,$$

where M_n is the product of Jacobians along the trajectory.

If the deviation typically grows (or shrinks) exponentially with n, we are led to define the finite-time Lyapunov's exponent

$$\lambda^{(n)}(\delta z_0) = \frac{1}{n} \ln \frac{\|M_n\,\delta z_0\|}{\|\delta z_0\|}. \tag{2.2}$$

Taking $n \to \infty$ defines the (asymptotic) Lyapunov's exponent

$$\lambda(\delta z_0) = \lim_{n\to\infty} \frac{1}{n} \ln \frac{\|M_n\,\delta z_0\|}{\|\delta z_0\|}, \tag{2.3}$$

whenever the limit exists. By Oseledets' multiplicative ergodic theorem [Ose68], for every nonzero δz_0 this limit exists and can only take one of the two values λ or $-\lambda$, depending on whether δz_0 has a component along the expanding or contracting Oseledets direction.

In numerical computations, repeatedly multiplying by Jacobians tends to align δz_0 with the most expanding direction, so (2.3) typically yields the largest Lyapunov's exponent λ [Ben+80a; Ben+80b]. A positive λ indicates sensitive dependence on initial conditions and is a standard diagnostic of chaos.

One of the standard examples where the Poincaré map exhibits coexisting regular islands and chaotic seas is the kicked rotator model, which we introduce next.

2.1. KICKED ROTATOR

The kicked rotator describes a free rotor subjected to a sequence of kicks and admits a description in terms of a two-dimensional Poincaré map, the standard (Chirikov–Taylor) map [Chi79]. In what follows we derive this map from the time-dependent Hamiltonian and briefly summarise its main dynamical regimes as a function of the kick strength K and calculate the Lyapunov's exponent for the standard map.

The kicked rotator model is a Hamiltonian system with $1+1/2$ degrees of freedom defined by the Hamiltonian

$$H(p,q;t) = \frac{1}{2}p^2 - K\cos(q)\sum_{n=-\infty}^{\infty}\delta(\frac{t}{T}-n). \tag{2.4}$$

This model can be interpreted as an unperturbed Hamiltonian

$$H_0 = \frac{1}{2}p^2$$

that is perturbed by a periodic sequence of delta-peaks with period $T = 2\pi/\nu$ and amplitude proportional to the scalar $K\cos(q)$ [Zas07, Section 1.2]. When the variable q is taken to be cyclic, i.e. $q \in (0, 2\pi)$, this model corresponds to a free rotator. The derived equations of motion from (2.4) are

$$\dot{p} = -K\sin(q)\sum_{n=-\infty}^{\infty}\delta(\frac{t}{T}-n), \quad \dot{q} = p.$$

We observe that $p = \text{const}$ and $q = pt + \text{const}$ in between consecutive delta-peaks. Let $0 < \epsilon < T$ and observe that

$$p(nT+\epsilon) - p(nT-\epsilon) = \int_{nT-\epsilon}^{nT+\epsilon}\dot{p}dt$$

$$= -K\int_{nT-\epsilon}^{nT+\epsilon}\sin(q)\sum_{n=-\infty}^{\infty}\delta(\frac{t}{T}-n)dt = -K\sin(q).$$

By taking the limit $\epsilon \to 0$ we observe that p change by the value $-K\sin(q)$ right after a delta-peak at $t = nT$, while q remains continuous.

We can construct a Poincaré map by defining (p_n, q_n) as the values of (p, q) in time right before the n-th delta-pulse. The derived equations of motion are

$$p_{n+1} = p_n - K\sin(q_n), \quad q_{n+1} = q_n + p_{n+1}.$$

This map is called the standard map, also known as the Chirikov–Taylor map. For $K = 0$, this is a simple linear map for which there exist only periodic and quasi-periodic orbits. For increasing values of K, more non-linearity is introduced to the map, which allows for the existence of chaotic dynamics in certain regions of phase space. Figure 2.1 illustrates the progression from a near-integrable to a strongly chaotic regime as K increases. For $K = 0.5$, most trajectories remain confined to smooth, closed invariant curves. For $K = 1.0$, thin stochastic layers form near separatrices. For $K = 1.5$, widespread torus breakup yields a large chaotic sea punctuated by stable islands; For $K = 3.0$, the dynamics are mostly chaotic, with only one visible surviving elliptic island.

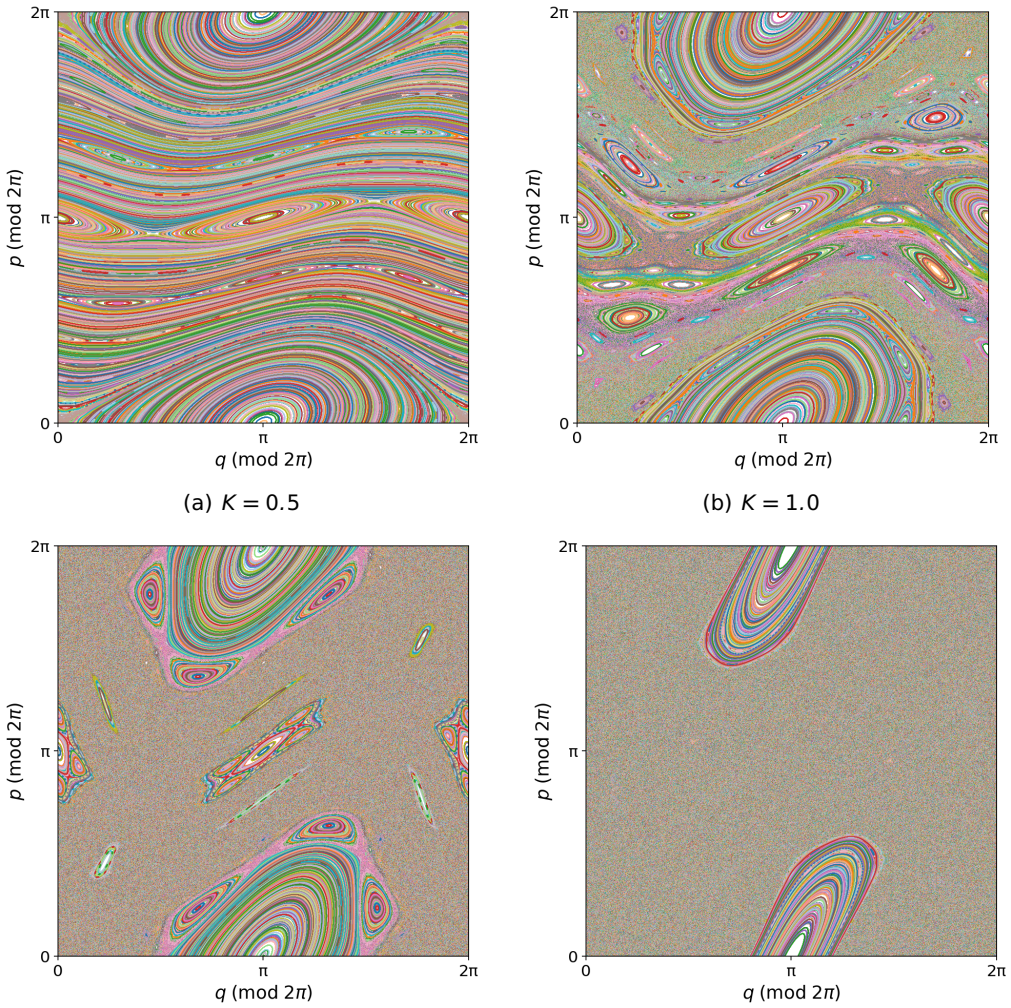

(a) $K = 0.5$ (b) $K = 1.0$

(c) $K = 1.5$ (d) $K = 3.0$

Figure 2.1.: Phase–space portraits of the standard map showing how increasing nonlinearity K transforms the dynamics. Each panel plots 2000 orbits in the coordinates $(q, p) \mod 2\pi$ (distinct colors denote different initial conditions only).

To calculate the Lyapunov's exponent for the standard map, we first calculate the Jacobian $DF(z_k)$ at $z_k = (p_k, q_k)$

$$DF(z_k) = \begin{pmatrix} \frac{\partial p_{k+1}}{\partial p_k} & \frac{\partial p_{k+1}}{\partial q_k} \\ \frac{\partial q_{k+1}}{\partial p_k} & \frac{\partial q_{k+1}}{\partial q_k} \end{pmatrix} = \begin{pmatrix} 1 & K\cos q_k \\ 1 & 1 + K\cos q_k \end{pmatrix}.$$

Observe that $\det(DF(z_k)) = 1$ for all values of k, so the Poincaré map is area-preserving.

Inserting this expression in (2.3) allows us to construct figure 2.2 and compare it with figure 2.1c, observe how the phase-space of the standard map model, for

$K = 1.5$, is clearly divided into stable integrable islands ($\lambda \approx 0$) and chaotic seas ($\lambda > 0$).

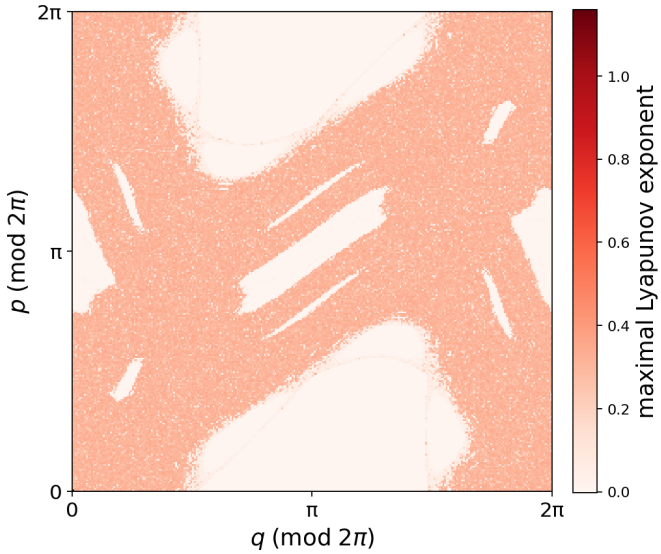

Figure 2.2.: Phase–space portraits of the standard map, for $K = 1.5$, showing how the maximum Lyapunov's exponent varies over the entire phase-space.

2.2. FERMI-PASTA-ULAM-TSINGOU CHAIN

The Fermi-Pasta-Ulam-Tsingou (FPUT) chain describes a one-dimensional periodic chain of particles with weak nearest-neighbour interactions and was originally introduced as a numerical experiment to test how quickly such systems approach equipartition of energy among normal modes. We recall the standard FPUT model, summarise the original paradoxical numerical observations, and explain how they can be understood by viewing the FPUT chain as a small perturbation of the integrable periodic Toda lattice.

Introduced in 1955 [Fer+55], the Fermi-Pasta-Ulam-Tsingou (FPUT) chain model is a Hamiltonian system with N degrees of freedom defined by

$$H(p, q) = \sum_{j=1}^{N} \frac{1}{2} p_j^2 + \Phi(q_{j+1} - q_j),$$

where $q_{N+1} \equiv q_1$ and

$$\Phi(z) = \frac{1}{2} z^2 + \frac{\alpha}{3} z^3 + \frac{\beta}{4} z^4.$$

When $\beta = 0$ ($\alpha = 0$) this model is called the FPUT-α (FPUT-β) model. It represents a periodic chain of particles linked by Hooke's law and a non-linear correction, which is quadratic for the FPUT-α model and cubic for the FPUT-β model.

In 1955, the original research project [Fer+55] tested the expectation that the weak non-linear interactions cause energy to disperse among normal modes until an equilibrium is reached, which is a central assumption of statistical mechanics. However, the numerical results deviated from this expectation, as can be seen in figure 2.3. Starting with a single linear normal mode, energy leaked into other

modes only partially and then returned near the original mode after a sufficiently long time.

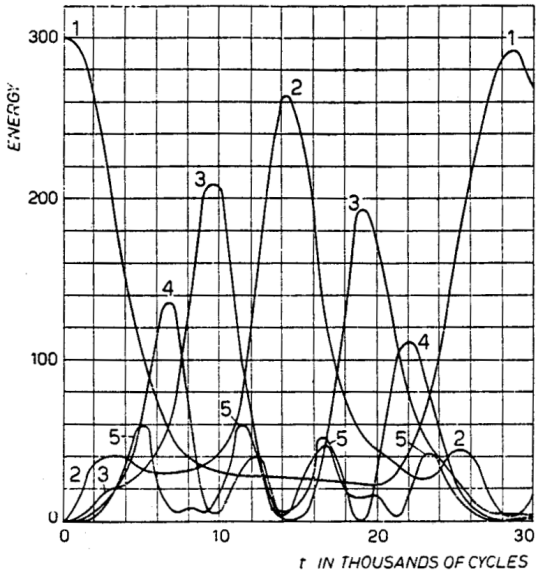

Figure 2.3.: Energy of the normal modes during the time evolution of the FPUT-α chain model with $N = 32; \alpha = 0.25;$. The initial shape of the chain was a single sine wave. Image sourced from the original project [Fer+55].

This result challenges the usual picture of macroscopic irreversibility that underlies the second law of thermodynamics. In the microcanonical framework, irreversibility is explained by assuming that, for a typical initial condition, the Hamiltonian trajectory explores the entire constant energy shell in phase space and is most present in the region corresponding to the equilibrium macrostate. In that case, time averages of observables coincide with microcanonical ensemble averages, and energy effectively spreads over all normal modes. The near-recurrence observed in the FPUT chain indicates that the dynamics remains confined to a much smaller portion of the energy shell, repeatedly returning close to the initial nonequilibrium configuration. This failure to efficiently explore the full energy shell prevents the system from exhibiting the expected macroscopic irreversibility and thermalization. Insights from the FPUT project show that this relaxation is more complex than expected, and not guaranteed by non-linear influences in the Hamiltonian. They support the idea of a prethermalization phase in which certain systems, that are nearly integrable or are slow mixing, approach equilibrium in two steps. First the system quickly reaches a quasi-stationary state where macroscopic observables appear frozen. Then, on much longer timescales, those observables slowly drift to their true thermodynamic values. More details on prethermalization can be found in [BBW04].

To better understand this phenomena, it is instructive to view the FPUT model not as an altered harmonic chain but as a perturbation of the periodic Toda lattice model. Introduced in 1967 [Tod67], the periodic Toda lattice system is a non-linear

Hamiltonian system with 2 degrees of freedom defined by

$$H(p,q)=\sum_{j=1}^{N}\frac{1}{2}p_j^2+\Psi(q_{j+1}-q_j),$$

where $q_{N+1}\equiv q_1$ and

$$\Psi(z)=A(e^{-Bz}+Bz-1).$$

Moreover, the periodic Toda lattice model is completely integrable. By choosing $A=\frac{1}{4\alpha^2}$ and $B=-2\alpha$ we can observe that

$$\Phi(z)-\Psi(z)=(\frac{\beta}{4}-\frac{\alpha^2}{6})z^4+\mathcal{O}(z^5).$$

Thus, at small perturbations $|z|\ll 1$, the FPUT model is indeed an analytic perturbation of the integrable Toda lattice model of size $\mathcal{O}(z^4)$.

Perturbations of integrable Hamiltonian systems can be written (after a suitable transformation) in the form

$$H(I,\theta)=H_0(I)+\varepsilon H_1(I,\theta),\qquad 0<\varepsilon\ll 1,$$

where H_0 is integrable, I are so called action variables, θ are angles, and ε measures the strength of the perturbation. KAM theory states, roughly speaking, that for sufficiently small ε most nonresonant invariant tori of the integrable system survive as slightly deformed invariant tori of the perturbed system. On these tori the motion remains quasi-periodic. Nekhoroshev's theorem addresses what happens to the actions $I(t)$ even in regions where resonances and small chaotic layers appear, under suitable nondegeneracy and convexity conditions one has

$$||I(t)-I(0)||\le C_1\varepsilon^b \quad \text{for all } |t|\le \exp(C_2\varepsilon^{-a}),$$

for some positive constants a, b, C_1, C_2 [Nek77]. Thus, away from strong resonances, the actions can drift only very slowly, remaining close to their initial values for times that are exponentially long in ε^{-1}. Together, KAM theory and Nekhoroshev's theorem provide an explanation for quasi-integrable behavior in weakly perturbed Hamiltonian systems.

For the periodic Toda lattice, global action–angle coordinates are constructed in [HK08] for which the Hamiltonian is a function of the actions alone and verify the nondegeneracy/convexity conditions that permit the application of KAM theory on (almost) all parts of phase space to small Hamiltonian perturbations of the periodic Toda lattice. Consequently, for actions on open regions away from resonances, the corresponding invariant tori persist and the motion remains quasi-periodic.

Moreover, by proving strict convexity of the periodic Toda lattice Hamiltonian in [HK09], it follows on (almost) all parts of phase space Nekhoroshev's theorem applies to sufficiently small perturbations, implying exponentially slow drift of the actions for exponentially long times. Viewing the low-energy FPUT chain as a small perturbation of the periodic Toda lattice, these results together motivate the persistence of quasi-periodic tori due to KAM theory and exponentially long stability of actions away from resonances due to Nekhoroshev's theorem, which underlies the observed long-lived prethermalization plateau in the FPUT model [BP23].

From this perspective, the FPUT chain shows how macroscopic irreversibility can fail, or at least be strongly delayed, in nearly integrable systems. The usual argument for irreversible relaxation to equilibrium assumes that the microscopic dynamics efficiently explores the entire energy surface in phase space, so that macroscopic observables rapidly forget their initial conditions. In contrast, for the

FPUT chain, the system can remain trapped for very long times in a quasi-integrable region where macroscopic observables appear stationary, the prethermal plateau, and only on much longer, typically exponential, time scales do the microstates explores the entire energy surface in phase space and restore the effective irreversibility expected from thermodynamics.

2.3. CLASSICAL LIMAÇON BILLIARDS

Billiards form another key class of systems whose dynamics span integrable motion, mixed regimes, and fully developed chaos. Billiard models provide a minimal, mechanics-only setting to examine how macroscopic phenomena, such as diffusion and heat conduction, emerge from microscopic dynamics. A billiard system describes a point particle that moves along straight lines inside a chosen two-dimensional domain Ω and reflects elastically off the domain's boundary $\partial\Omega$. The geometry can make motion integrable or strongly chaotic.

A particularly important example in this class is the Sinai billiard, consisting of a point particle moving in a square with a circular disk removed from the interior. This model provides a clear example of deterministic chaos, it is known to be ergodic, mixing, and a K-system [Sin70]. Physically, it can be interpreted as a simple Lorentz gas, where a particle moves freely between elastic collisions with fixed circular scatterers. As such, Sinai billiards serve as a prototype for understanding how macroscopic irreversibility and transport can emerge from microscopic, time-reversible dynamics. Moreover, this model motivates the study of other billiard families in which the onset of chaos can be tuned by continuously changing the geometry of the billiard domain.

Another billiard model that illustrates this tuning principle particularly well is the limaçon billiard model which is, for some $\epsilon \in [0, 1]$, defined in polar coordinates by the domain

$$\Omega \equiv \{(1 + \epsilon \cos(\phi), \phi) | \phi \in [0, 2\pi)\}. \tag{2.5}$$

Figure 2.4 illustrates how the extremes of this model either correspond with an integrable system, for which the domain is circular ($\epsilon = 0$), or a system that is ergodic, mixing, a K-system and a Bernoulli system for which the domain is a cardioid ($\epsilon = 1$) [Woj86; Szá92; Mar93; LW95; CH96].

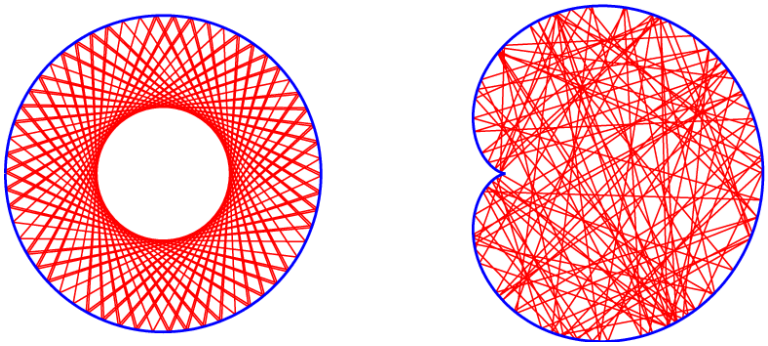

Figure 2.4.: Regular motion in a circular billiard ($\epsilon = 0$) contrasted with chaotic motion in a cardioid billiard ($\epsilon = 1$). Image sourced from [Bäc07].

To study the transition between these type of dynamics it is worthwhile to construct a Poincaré map that takes a snapshot of the billiard every time it collides with the boundary of the domain. Let $\mathcal{L}$ denote the length of the boundary $\partial\Omega$. We

introduce the coordinate of the n-th collision as (s_n, u_n). Here $s_n \in [0, \mathcal{L}]$ denotes the arclength along the boundary $\partial\Omega$ and $u_n = \langle v, T(p) \rangle$ is the projection of the unit velocity vector v after the reflection along the unit normal vector $T(p)$ at the n-th collision point $p \in \partial\Omega$. Figure 2.5 illustrates the progression from a near-integrable to a strongly chaotic regime as ϵ increases. For $\epsilon = 0.1$, most trajectories remain confined to smooth, closed invariant curves. For $\epsilon = 0.2$, thin stochastic layers form near separatrices. For $\epsilon = 0.3$, widespread torus breakup yields a large chaotic sea punctuated by stable islands; For $\epsilon = 0.4$, the dynamics are predominantly chaotic, with a small amount of surviving stable islands.

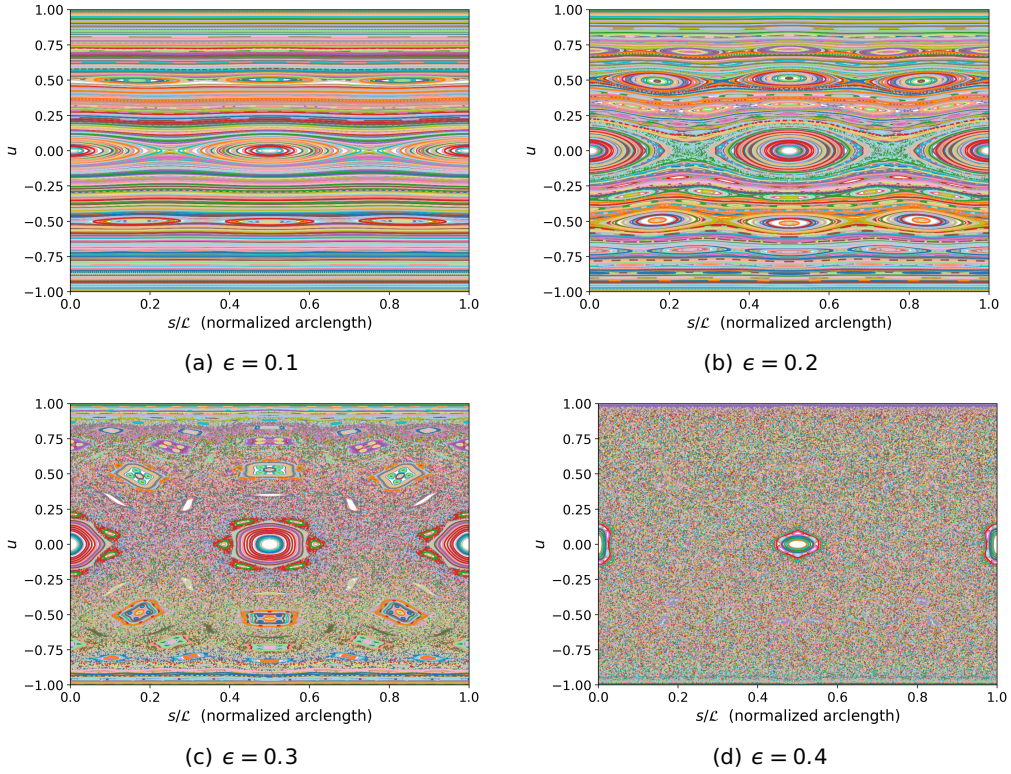

(a) $\epsilon = 0.1$ (b) $\epsilon = 0.2$

(c) $\epsilon = 0.3$ (d) $\epsilon = 0.4$

Figure 2.5.: Phase–space portraits of the limaçon billiard model showing how the changing domain transforms the dynamics. Each panel plots 2000 orbits in the coordinates $(s/\mathcal{L}, u)$ (distinct colors denote different initial conditions only).

2.4. SPIN CHAIN MODELS

Classical spin chains provide a setting to study nonlinear many-body dynamics and chaos. Different choices of spin interactions lead to qualitatively distinct dynamical behaviours, ranging from fully chaotic to exactly integrable. In this section we focus on two examples: the non-integrable classical Heisenberg chain, which models an isotropic ferromagnet, and the integrable Ishimori chain, which supports an infinite amount of conservation laws while featuring strongly nonlinear spin interactions.

A classical spin model describing N spins is defined by N three-dimensional vectors $\mathbf{S}_i = (\mathbf{S}_i^x, \mathbf{S}_i^y, \mathbf{S}_i^z)$ with length $||\mathbf{S}_i|| = 1$. The equations of motion for these

spins are given by

$$\dot{\mathbf{S}}_i = \frac{\partial H}{\partial \mathbf{S}_i} \times \mathbf{S}_i,$$

for some Hamiltonian $H(\mathbf{S}_1, \ldots, \mathbf{S}_N)$. The classical non-integrable Heisenberg chain model describes an isotropic ferromagnet and is one of the simplest dynamical models of magnetism. It is defined by the Hamiltonian

$$H = -J \sum_i (\mathbf{S}_i \cdot \mathbf{S}_{i+1} - 1), \tag{2.6}$$

where the constant $J > 0$ denotes the strength of the nearest-neighbour interaction. Unlike integrable spin chains, the Heisenberg chain model appears to possess only a small set of conserved quantities (energy, total magnetization, and total momentum).

The classical Ishimori chain model is described by the Hamiltonian

$$H = -2J \sum_i \ln\left(\frac{1 + \mathbf{S}_i \cdot \mathbf{S}_{i+1}}{2}\right). \tag{2.7}$$

This model is, in contrast to the Heisenberg chain model, an example of a strongly non-linear yet exactly integrable system, it admits an infinite set of local conserved quantities in addition to energy and total magnetization [Ish82]. The conserved quantities are implied by the existence of an infinite amount of exact soliton solutions $\mathbf{S}_i(t)$, which are spin configurations defined for some arbitrary real parameters ω, ν, that evolve in time without changing shape according to the relation

$$\mathbf{S}_{i+n}(t + \frac{n}{\nu}) = R_z(\frac{n\omega}{\nu})\mathbf{S}_i(t),$$

where R_z denotes a rotation around the z-axis, for all integers n.

3

QUANTUM CHAOS

There is no single, universally accepted criterion for what should count as quantum chaos. Because the Schrödinger evolution is linear and unitary, the usual trajectory-based definition of chaos simply does not carry over. Instead, one diagnoses chaotic versus integrable behavior indirectly, for example through the random-matrix character of energy-level statistics, the structure and delocalization properties of eigenstates, or the growth of correlation functions [Haa10]. One of the more popular of these signatures is defined in terms of the statistical properties of the energy levels of the Hamiltonian.

3.1. LEVEL-SPACING STATISTICS

Historically, the level-spacing statistics signature was developed in the research of describing the level repulsion observed in neutron scattering. In 1951, Wigner postulated that the associated Hamiltonian is modeled as a large real symmetric random matrix whose entries are independent, up to the symmetry constraint, and Gaussian-distributed [Wig51]. This results in the following probability distribution

$$P(H) \propto \exp(-c\,\mathrm{Tr}(H^2)), \quad c > 0,$$

which is equivalent with the Gaussian orthogonal ensemble (GOE). To compare different systems in this ensemble, the nearest-neighbor level spacings are constructed as

$$s_n = E_{n+1} - E_n \geq 0,$$

where $\{E_n\}$ is the sequence of energies of the system ordered monotonically. One then studies the probability density $P(s)$ of these spacings, with the convention that $\langle s \rangle = 1$. For the GOE, this level-spacing distribution is well approximated by the Wigner surmise

$$P(s) = \frac{\pi}{2}\, s \exp\left(-\frac{\pi}{4} s^2\right), \qquad s \geq 0,$$

which exhibits level repulsion at small spacings. This distribution turned out to describe the level repulsion observed in neutron scattering remarkably well. An illustrative example how the assumption that the Hamiltonian is Gaussian-distributed leads to the GOE distribution is provided in Appendix A.1.

For different symmetries, different random-matrix ensembles need to be applied. If the Hamiltonian is modeled as a complex Hermitian matrix with independently distributed Gaussian entries. This defines the Gaussian unitary ensemble (GUE), whose level-spacing distribution (again with $\langle s \rangle = 1$) is described by

$$P_{\mathrm{GUE}}(s) = \frac{32}{\pi^2}\, s^2 \exp\left(-\frac{4}{\pi} s^2\right), \qquad s \geq 0.$$

A third class appears when the Hamiltonian is represented by self-adjoint matrices with independently distributed Gaussian quaternions as elements. This leads to the Gaussian symplectic ensemble (GSE), with the level-spacing distribution

$$P_{\mathrm{GSE}}(s) = \left(\frac{64}{9\pi}\right)^3 s^4 \exp\left(-\frac{64}{9\pi}s^2\right), \qquad s \geq 0.$$

In this thesis we will not analyze the GUE or GSE cases further, since the Hamiltonian of interest is real and symmetric and therefore belongs to the GOE class.

In contrast, for an integrable quantum system there exists a complete set of mutually commuting conserved operators $\{Q_i\}$ with $[H, Q_i] = 0$ and $[Q_i, Q_j] = 0$ for all i, j. One can then choose a basis $\{|\alpha\rangle\}$ of simultaneous eigenstates of H and all $\{Q_i\}$ [SN20, Section 1.4.3], defined by

$$H|\alpha\rangle = E_\alpha|\alpha\rangle, \qquad Q_i|\alpha\rangle = q_{i,\alpha}|\alpha\rangle. \tag{3.1}$$

If the Hamiltonian depends on some external parameter λ which can vary while preserving the commutation relations $[H(\lambda), Q_i] = 0$ for all i, then the eigenstates can be labeled by the same eigenvalues $q_{i,\alpha}$ for every λ. Additionally, because of $[H(\lambda), Q_i] = 0$ we have

$$\langle\alpha|Q_i H(\lambda)|\beta\rangle = \langle\alpha|H(\lambda)Q_i|\beta\rangle. \tag{3.2}$$

Using $Q_i|\alpha\rangle = q_{i,\alpha}|\alpha\rangle$ and $Q_i|\beta\rangle = q_{i,\beta}|\beta\rangle$ this becomes

$$q_{i,\alpha}\langle\alpha|H(\lambda)|\beta\rangle = q_{i,\beta}\langle\alpha|H(\lambda)|\beta\rangle, \tag{3.3}$$

so that

$$(q_{i,\alpha} - q_{i,\beta})\langle\alpha|H(\lambda)|\beta\rangle = 0. \tag{3.4}$$

Hence, if $q_{i,\alpha} \neq q_{i,\beta}$ for some i, it follows that $\langle\alpha|H(\lambda)|\beta\rangle = 0$, which implies that there are no matrix elements of H between states with different sets $\{q_{i,\alpha}\}$. The corresponding eigenvalues $E_\alpha(\lambda)$ therefore change independently as functions of λ, and whenever $E_\alpha(\lambda) = E_\beta(\lambda)$ for $\alpha \neq \beta$ the associated levels simply cross rather than repelling each other. Thus, level crossings are common and there is no tendency for nearby levels to push each other apart. This implies that the energy levels behave approximately like independent random points on a line. Such an uncorrelated sequence of points with constant average density defines a Poisson point process, whose nearest-neighbour spacing distribution is $P_{\mathrm{Poisson}}(s) = \exp(-s)$ after setting the mean level spacing $\langle s\rangle = 1$ [BT77b].

3.2. Loschmidt echoes

The Loschmidt echo is another signature of quantum chaos and quantifies how well a many–body quantum system can be time–reversed in the presence of small imperfections. One prepares a localized spin excitation $|\psi\rangle$ at time $t = 0$ and lets it evolve under a many–spin Hamiltonian H_0, during which the excitation spreads through the lattice via spin diffusion [Sli90]. At a later time t, a sequence of radiofrequency pulses is applied that ideally reverses the sign of the Hamiltonian. In practice, this pulse sequence generates an effective backward evolution under $-(H_0 + \Sigma)$, where the perturbation Σ accounts for pulse imperfections and residual interactions. Such time–reversal protocols were first realized for dipolar–coupled spins by Rhim, Pines, and Waugh [RPW71].

After evolving forward under H_0 and then backward under $-(H_0+\Sigma)$, one probes how close the system returns to its initial state at the echo time $2t$ by measuring the return probability to $|\psi\rangle$. This is the Loschmidt echo,

$$M(t) = \left| \langle\psi| \exp\left(\frac{i(H_0+\Sigma)t}{\hbar}\right) \exp\left(-\frac{iH_0 t}{\hbar}\right) |\psi\rangle \right|^2, \tag{3.5}$$

which directly measures how sensitive the many–body dynamics is to the small perturbation Σ and thus to imperfections of the attempted time reversal [JP01].

For systems whose classical counterparts are chaotic, one typically finds an exponential decay of the echo over a broad time window when the perturbation Σ is small. The corresponding decay rate can be related to the classical Lyapunov exponents [Gor+06; JP01]. By contrast, integrable or otherwise nonergodic dynamics usually lead to a slower decay of $M(t)$. These slower decays reflect long–lived correlations in the underlying dynamics and the absence of strong phase–space mixing [Pro02; PŽ02].

In the semiclassical regime of a quantum–chaotic system, Silvestrov, Tworzydło, and Beenakker showed a more detailed connection between the Loschmidt echo and classical chaos [STB03]. The time evolution under two slightly different Hamiltonians can be viewed as the motion of two initially nearby wave packets in classical phase space. Their separation and deformation are controlled by the classical Lyapunov exponent λ, with typical separations growing as $e^{\lambda t}$. The Loschmidt echo essentially probes the phase–space overlap of these two packets. For generic initial states in a quantum–chaotic system, this leads to a characteristic double–exponential decay of the form

$$M(t) \propto \exp\left(-C\, e^{2\lambda t}\right), \tag{3.6}$$

where $C > 0$ is some constant. In this way, the classical Lyapunov exponent λ appears explicitly in the time dependence of $M(t)$, making the Loschmidt echo a direct indicator of classical–like exponential instability in the semiclassical limit.

The case of interacting spin systems provides another example of how classical and quantum notions of chaos can differ. Fine et al. studied Loschmidt–echo–type responses in both chaotic lattices of classical spins and nonintegrable systems of quantum spins 1/2, using the recovered total magnetization after an imperfect time–reversal protocol as the Loschmidt echo [Fin+14]. For classical spin systems with chaotic dynamics, they showed that the deviation from perfect reversal,

$$1 - F(t) \propto \exp\left(2\lambda t\right), \tag{3.7}$$

grows exponentially in an intermediate time window, where $F(t)$ is an appropriately normalized magnetization echo and λ is the largest Lyapunov exponent of the underlying classical dynamics. This result demonstrates that λ can, in principle, be extracted from a macroscopic observable in a many–spin system.

In striking contrast, for quantum spin–1/2 systems, which display GOE level-spacing statistics, Fine et al. found only a power–law sensitivity of the magnetization echo to small perturbations, with no exponential growth regime. This means that one cannot define a Lyapunov's exponent from the echo dynamics of the quantum spin-1/2 system.

3.3. Quantum limaçon billiards

Having introduced two signatures of quantum chaos, we now turn to a concrete model that illustrates how chaotic and integrable dynamics are reflected in the

level-spacing statistic. In the quantum regime, the state of a particle with mass m at position $\mathbf{r}$ and time t is described by a complex-valued wave function ψ that evolves according to the Schrödinger equation

$$i\hbar\frac{\partial}{\partial t}\psi(\mathbf{r},t) = -\frac{\hbar^2}{2m}\Delta\psi(\mathbf{r},t) + V(x,t)\psi(\mathbf{r},t), \tag{3.8}$$

where $V(\mathbf{r},t)$ is the potential energy function of the environment and Δ denotes the Laplacian operator. The quantum variant of the limaçon billiard model is once again defined by the two-dimensional domain

$$\Omega \equiv \{(r(\phi),\phi) | \phi \in [0, 2\pi)\}, \tag{3.9}$$

where $\epsilon \in [0,1]$ and $r(\theta) = 1 + \epsilon\cos(\phi)$. The environment of this model is represented by the potential function

$$V_{\text{Billiards}}(\mathbf{r}) \equiv \begin{cases} 0, & \mathbf{r} \in \Omega \\ \infty, & \mathbf{r} \notin \Omega \end{cases}.$$

The energy levels E_n of the stationary solutions ψ_n of (3.8) are governed by

$$-\frac{\hbar^2}{2m}\Delta\psi_n(\mathbf{r}) = E_n\psi_n(\mathbf{r}), \quad \mathbf{r} \in \Omega \tag{3.10}$$

combined with the Dirichlet boundary condition $\psi_n|_{\partial\Omega} = 0$. Note that due to enforcing the mean level spacing $\langle s\rangle$ to be 1 the factor $\hbar^2/2m$ is irrelevant in the eventual level spacing statistics. We choose units such that $\hbar^2/2m = 1$ so that (3.10) reduces to the Helmholtz equation

$$(-\Delta - k_n^2)\psi_n(\mathbf{r}) = 0, \quad \mathbf{r} \in \Omega, \tag{3.11}$$

where $E_n = k_n^2$. Analytic solutions of (3.11) are available only for a limited class of domains, such as rectangles and disks. For more general shapes of Ω, we must resort to numerical methods to compute the corresponding eigenvalues and eigenfunctions of (3.11), of which we numerically can only calculate a finite amount N.

Having obtained N eigenvalues and eigenfunctions of (3.11), we can construct the level spacing statistic through constructing the histogram of the energy level spacings $s_n = E_n - E_{n+1}$, which are normalized such that the mean level spacing $\langle s\rangle$ is 1. These histograms are show in figure 3.1 for the circle billiard ($\epsilon = 0$) and cardioid billiard ($\epsilon = 1$). We observe how the level spacing statistic distribution is described by the Poisson distribution for the circle billiard, which corresponds with the expected distribution for an integrable system. In contrast, observe how the level spacing statistic distribution for the cardioid billiard is described by the GOE distribution (A.1) for the cardioid billiards, which is characteristic for systems with chaotic dynamics and energy level repulsion.

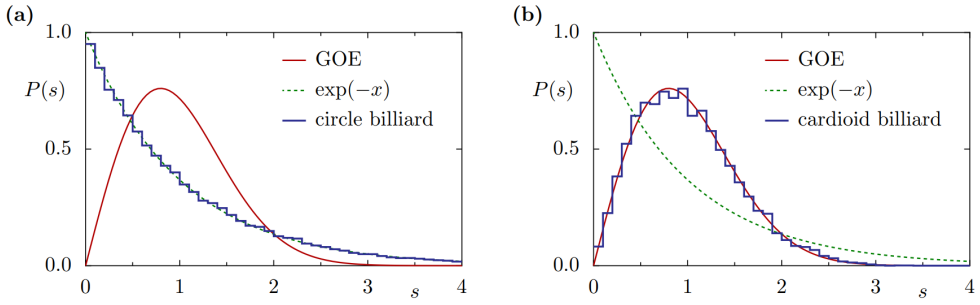

Figure 3.1.: Level–spacing distribution for (a) circle billiard (100000 eigenvalues; $\epsilon = 0$) and (b) cardioid billiard (11000 eigenvalues; $\epsilon = 1$). Image sourced from [Bäc07].

In figure 3.2, we also observe for the circle billiard that the probability density is concentrated in certain subregions of the domain, while in the chaotic cardioid case it is, aside from fluctuations, distributed over the entire domain.

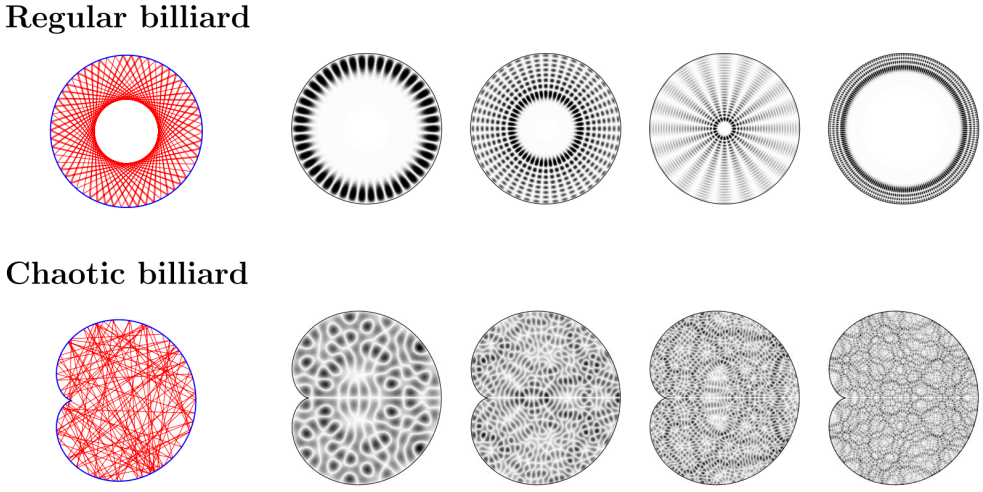

Figure 3.2.: Classical trajectories (first column) and probability densities $|\psi_n(\mathbf{r})|^2$ of eigenfunctions (other columns) of (3.11) for the circle billiard (top row) and the cardioid billiard (bottom row). From left to right, the eigenfunctions shown correspond to the indices $n = 100$, $n = 1000$, $n = 1500$ and $n = 2000$. Sourced from [Bäc07].

3.4. SPIN GLASS SHARDS

The term spin glass shard refers to a finite cluster of strongly interacting spins embedded in a larger system. These finite clusters can be modeled by a fully connected spin-glass Hamiltonian in a random transverse field, and provide a setting to study level spacing statistics. The spin glass shards model we are studying can be viewed as the Sherrington–Kirkpatrick model subject to a transverse magnetic field. This model allows us to analyse the crossover from integrable to chaotic

quantum dynamics as the strength of the field changes.

Now, we will introduce the quantum system whose classical analogue we will study in this thesis. The model is defined, for N spins in the quantum regime, by the Hamiltonian

$$H = \sum_{i<j} J_{ij}\, \sigma_x^i \sigma_x^j + \sum_{i=1}^{N} \Gamma_i\, \sigma_i^z, \tag{3.12}$$

where σ_x^i and σ_z^i are the Pauli matrices for the i-th spin, and the first sum runs over all distinct spin pairs [GS98]. The local transverse magnetic field is represented by the coefficients Γ_i which are drawn independently from a uniform distribution in the interval $[0, \Gamma]$. The exchange interactions J_{ij} are taken to be independent random variables uniformly distributed in the interval $[-J/\sqrt{N}, J/\sqrt{N}]$. The $1/\sqrt{N}$ factor ensures the variance of the local field stays finite rather than diverging with system size. In this way one obtains a well-defined thermodynamic limit as $N \to \infty$.

In this model the randomness is quenched: the couplings J_{ij} and local fields Γ_i are randomly drawn once and then kept fixed during the time evolution. Physically, they represent static imperfections of the sample, such as fixed positions of magnetic ions or defects in a solid, which do not fluctuate on the timescale of the spin dynamics. A single choice of all $\{J_{ij}\}$ and $\{\Gamma_i\}$ at fixed $J, \Gamma > 0$ is called a realization of disorder. Because the couplings J_{ij} have random signs, the system is generally frustrated due to it generally not being possible to choose spin orientations that simultaneously minimize all pairwise interaction terms. As a result, there is usually no simple ferromagnetic or antiferromagnetic ground state, unless $\Gamma \gg J$.

When constructing the level-spacing statistics we must also account for the symmetries of the Hamiltonian. In particular, H is invariant under the global spin-flip operation generated by $P = \prod_{i=1}^{N} \sigma_z^i$, which flips all $\sigma_x^i \to -\sigma_x^i$ while leaving H unchanged. Since $[H, P] = 0$, the Hilbert space splits into two independent symmetry sectors, S_1 and S_2, corresponding to the eigenvalues $P = +1$ and $P = -1$, respectively. In the σ_z basis this means that states in S_1 are superpositions of basis states with an even number of spins up, whereas states in S_2 are superpositions of basis states with an odd number of spins up. Thus the Hamiltonian is block diagonal $H = H_{S_1} \oplus H_{S_2}$, with H_{S_1} acting only on the sector S_1 and H_{S_2} only on S_2. The eigenvalues in S_1 and S_2 therefore come from two independent blocks. To obtain meaningful level-spacing statistics, we therefore restrict ourselves to a single block, S_1 or S_2.

The model contains two simple integrable limits. For $J/\Gamma \to 0$ ($J/(J+\Gamma) \to 0$), the Hamiltonian reduces to a sum of terms proportional to σ_i^z. In this case, there are N conserved quantities given by the commuting operators σ_i^z, and the Hamiltonian is diagonal in the σ^z basis. The level spacings between many-body eigenvalues are then uncorrelated. Consequently, in this integrable regime the level spacing distribution $P(s)$ is expected to be Poissonian, $P(s) = P_{\text{Poisson}}(s)$.

As the ratio J/Γ is increased from zero, the interaction term $\sum_{i<j} J_{ij} \sigma_x^i \sigma_x^j$ mixes the states that are eigenstates of the transverse magnetic field term, destroying the set of conserved quantities associated with σ_i^z. One then expects a progressive breakdown of integrability and the onset of quantum chaos. In this regime the level spacings should exhibit level repulsion and be well described by the GOE distribution, with $P(s)$ approaching $P_{\text{GOE}}(s)$ characteristic of chaotic dynamics.

However, in the opposite limit $J/\Gamma \to \infty$ ($J/(J+\Gamma) \to 1$), the transverse magnetic field becomes negligible compared to the spin-spin interaction term. The Hamiltonian then commutes with all N operators σ_x^i and is diagonal in the σ^x basis. This again yields a set of conserved quantities and an integrable many-body system. As a result, the level statistics in this limit returns to the Poisson distribution $P_{\text{Poisson}}(s)$.

Thus, as a function of J/Γ ($J/(J+\Gamma)$) the system exhibits two crossovers from Poissonian to GOE statistics, as can be seen in figure 3.3.

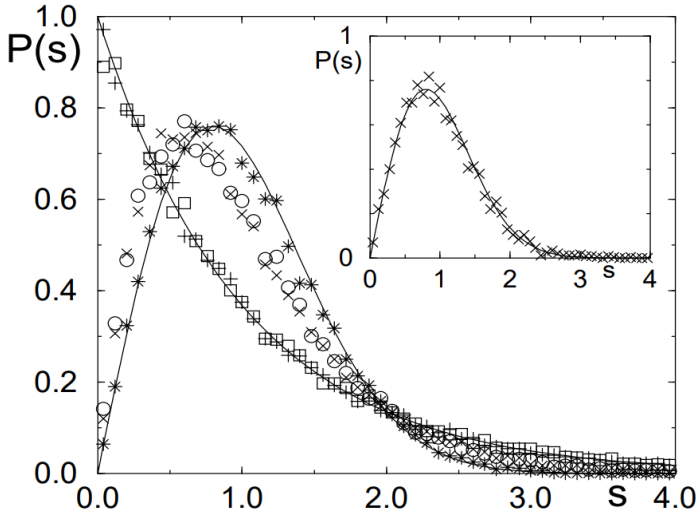

Figure 3.3.: Crossover from Poissonian to GOE statistics in the model for the states in the middle of the energy band (±12.5% around the center) for $N = 12$: $J = 0$, $\eta = 0.984$ (+); $J/\Gamma = 0.38$, $\eta = 0.3$ (×); $J/\Gamma = 0.866$, $\eta = 0.027$ (*); $J/\Gamma = 6.15$, $\eta = 0.3$ (∘); $\Gamma = 0$, $\eta = 0.99$ (□). Full curves show the Poisson and GOE distributions. Total statistics (NS) is more than 3×10^4; s is in units of mean level spacing. Inset shows $P(s)$ for the first excitation from the ground state in the chaotic regime for $N = 15$, $J/\Gamma = 0.465$, $\eta_0 = 0.018$ ($NS = 3000$) (×); the full line shows $P_{\mathrm{GOE}}(s)$. Data are for S_2 symmetry. Sourced from [GS98].

To quantify the crossover from Poissonian to GOE statistics it is convenient to introduce the dimensionless parameter

$$\eta = \frac{\int_0^{s_0} \left(P(s) - P_{\mathrm{GOE}}(s)\right) ds}{\int_0^{s_0} \left(P_{\mathrm{Poisson}}(s) - P_{\mathrm{GOE}}(s)\right) ds}, \tag{3.13}$$

where s denotes the level spacing measured in units of the mean spacing, and $s_0 \approx 0.4729$ is the intersection point of the Poisson and GOE distributions, i.e. the solution of $P_{\mathrm{Poisson}}(s_0) = P_{\mathrm{GOE}}(s_0)$. By construction, $\eta = 1$ when $P(s)$ coincides with the Poisson distribution (integrable limit) and $\eta = 0$ when $P(s)$ is equal to the GOE distribution (chaotic limit). For intermediate values of J/Γ ($J/(J+\Gamma)$), $0 < \eta < 1$ provides a convenient single-parameter measure of how close the spectrum is to either integrable or chaotic behavior. As J/Γ ($J/(J+\Gamma)$) is tuned, η tracks the approach to GOE statistics and its subsequent return towards Poissonian statistics as the system crosses between the integrable magnetic, chaotic, and integrable spin-spin regimes, see figure 3.4.

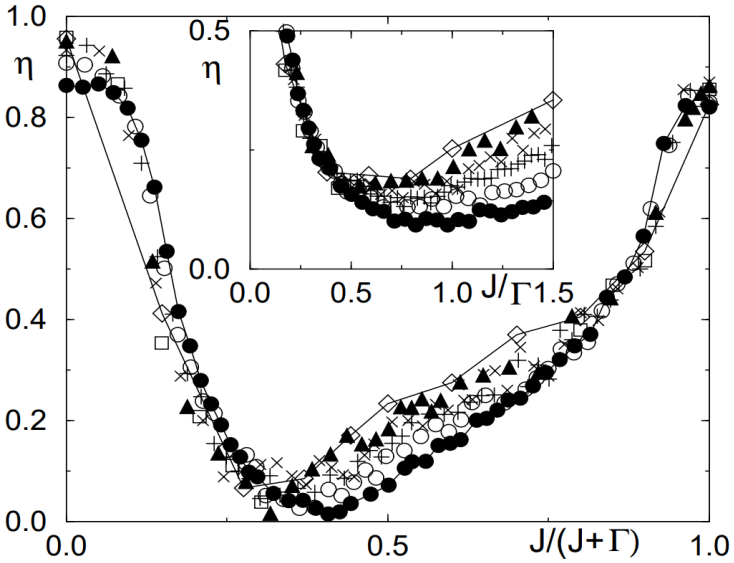

Figure 3.4.: Dependence of η on $\tilde{J} = J/(J+\Gamma)$: $n = 7$ (full circles), $n = 9$ ($\circ$), $n = 11$ ($+$), $n = 13$ ($\times$), $n = 15$ (full triangles), $n = 17$ ($\diamond$), $n = 19$ ($\square$); $2000 \leq NS \leq 30000$. Full curves connect data for $n = 7, 17$. Inset shows η_1 in the region near $J/\Gamma \approx 0.5$ in more detail; $6000 \leq NS \leq 90000$. Data are for S_1 symmetry. Sourced from [GS98].

4

HAMILTONIAN DYNAMICS AND LYAPUNOV'S EXPONENTS

Classical mechanics knows several equivalent formulations. Historically, the initial introduction of forces in Newtonian mechanics enabled the study of planetary trajectories [New87]. However, one is required to go through a rather laborious process to analyze complex systems. In 1788, Joseph-Louis Lagrange introduced the equivalent Lagrangian mechanics, which defines the Lagrangian $\mathcal{L}$ from which the time evolution can be derived through the Euler–Lagrange equation [Lag88]. In 1834, Sir William Rowan Hamilton introduced Hamiltonian mechanics which introduced the Hamiltonian $\mathcal{H}$ [Ham34]. This formulation made use of the Poisson bracket operation $\{\cdot,\cdot\}$, defined earlier by Siméon Denis Poisson in 1809 [Poi09], to establish the time evolution equation of any observable f as

$$\frac{df}{dt} = \{f, \mathcal{H}\} + \frac{\partial f}{\partial t}. \tag{4.1}$$

Under suitable conditions, one usually defines $\mathcal{L} = T - V$ and $\mathcal{H} = T + V$, where T and V respectively denote the kinetic energy and potential energy of the system. For a modern treatment of classical mechanics in its Newtonian, Lagrangian, and Hamiltonian formulations, see [GPS02]. To define Hamiltonian dynamics on more exotic phase spaces, one requires the concept of symplectic manifolds. In ordinary Hamiltonian mechanics this structure is the usual phase space $\mathbb{R}^{2n}$, but for more exotic phase spaces, such as motion on a sphere, it becomes essential. Symplectic manifolds are precisely the spaces on which Hamiltonian time evolution is defined and captures geometric features like Liouville's theorem.

4.1. SMOOTH MANIFOLDS

Firstly, to properly describe Hamiltonian dynamics on symplectic manifolds some additional mathematical concepts are required. The definitions and basic results on smooth manifolds, tangent spaces, and symplectic manifolds used in this section are adapted from [Arn89; Lee97; Lee13]. The full mathematical definitions and results mentioned in this section are provided in Appendix A.2. Firstly, one is required to introduce the concept of a smooth manifold M. In general, a smooth manifold M is an n-dimensional space that locally looks like $\mathbb{R}^n$ and we can do calculus on, so that we can define derivatives.

The tangent space T_pM at a point p on a manifold M is the collection of all possible velocity vectors of smooth curves passing through that point, organized into a linear space. The set of all such vectors forms the tangent space.

The tangent space behaves like the optimal linear approximation of the manifold near a point p, so that even though the manifold may be curved or complicated

globally, in the tangent space you can use linear algebra and calculus as if you were in an ordinary vector space.

To perform calculations on a manifold, it is necessary to introduce local coordinates. A coordinate system around a point $p \in M$ is given by a map $\varphi : U \subset M \to \mathbb{R}^n$ from a neighbourhood U of p into Euclidean space. In these coordinates, the point p is described by $(x^1, \dots, x^n)$, and tangent vectors at p can be represented by their components with respect to differentiating in these coordinate directions $\frac{\partial}{\partial x^i}$. This allows one to temporarily replace the structure of M near p by familiar multivariable calculus on $\mathbb{R}^n$, perform computations there, and then interpret the results back on the manifold.

To measure the size of tangent vectors, one can define an additional Riemannian metric g on M. A Riemannian metric g on M is a smoothly varying inner product on the tangent spaces. For each point $p \in M$ it defines a bilinear, symmetric, positive definite map

$$g_p : T_pM \times T_pM \to \mathbb{R},$$

depending smoothly on p. This inner product induces a norm on each tangent space via

$$||v||_g := \sqrt{g_p(v, v)}, \qquad v \in T_pM.$$

The Riemannian metric also induces a distance between points on M. Given a smooth curve $\gamma : [0, 1] \to M$ with $\gamma(0) = p$ and $\gamma(1) = q$, its length with respect to g is defined by

$$L_g(\gamma) = \int_0^1 ||\dot\gamma(t)||_g \, dt = \int_0^1 \sqrt{g_{\gamma(t)}\big(\dot\gamma(t), \dot\gamma(t)\big)}\, dt.$$

The Riemannian distance between two points $p, q \in M$ is then defined as the infinimum of L_g over all possible smooth curves $\gamma : [0, 1] \to M$ with $\gamma(0) = p$ and $\gamma(1) = q$. With this distance function (M, d_g) becomes a metric space, and curves that locally minimize L_g are called geodesics.

4.2. SYMPLECTIC MANIFOLDS

A symplectic manifold is a smooth, even-dimensional manifold M with an additional geometric structure called a symplectic form ω. Intuitively, the symplectic form ω takes two tangent vectors in T_pM at a point p on the manifold M and returns a real number measuring an oriented infinitesimal area spanned by those tangent vectors. This pairing is bilinear, antisymmetric, closed and non-degenerate. Moreover, this structure varies smoothly from point to point. On a symplectic complex manifold one can always define a Riemannian metric g that is compatible with the symplectic form ω [dSil01, Corollary 12.7], so that the Riemannian volume coincides, up to a constant factor, with the Liouville volume.

Building on this, a vector field X_H arises when one specifies a smooth function $H : M \to \mathbb{R}$, typically interpreted as the total energy of the system on the symplectic manifold M. The differential $dH : T_pM \to \mathbb{R}$ tells you how H changes along any tangent direction at a point p, the symplectic form ω allows you to transform this into a vector field X_H on M, assigning to each $p \in M$ a tangent vector $X_H(p) \in T_pM$.

Once you have a vector field, you can interpret it as describing how points in phase space move in time under the dynamics generated by a function. Given a smooth function $f : M \to \mathbb{R}$, its vector field X_f assigns to each point p a tangent vector $X_f(p)$ that describes the direction the system will move in if it is at p. Letting the system evolve according to X_f traces out trajectories in M.

Now take another function $g : M \to \mathbb{R}$, representing some observable of the system (for example, a position component, momentum component, or some other derived

quantity). As the system moves along the trajectories determined by X_f, the value of g will generally change in time. The Poisson bracket $\{\cdot,\cdot\}$ is defined as the antisymmetric bilinear operation

$$\{g, f\} := X_f(g),$$

and can be read as the instantaneous rate of change of g when the system evolves according to the dynamics generated by f. Intuitively, the Poisson bracket tells you how much the observable g changes when the system follows the motion prescribed by f. Additionally, the Poisson bracket satisfies the Leibniz rule

$$\{f, gh\} = g\{f, h\} + \{f, g\}h.$$

When f is chosen to be the Hamiltonian H, the Poisson bracket directly encodes the time evolution of any observable g. In this case, the Hamiltonian vector field X_H generates the actual physical motion of the system in phase space, so the rate of change of g along a trajectory is given by

$$\frac{d}{dt}g = X_H(g) = \{g, H\}.$$

Thus, the Poisson bracket with H tells you how fast an observable g changes in time under the dynamics determined by the Hamiltonian. Additionally, it immediately implies that the Hamiltonian H is conserved in time due to $\frac{d}{dt}H = \{H, H\} = 0$. In this sense, the Poisson bracket provides a way to express the equations of motion for all observables of the system.

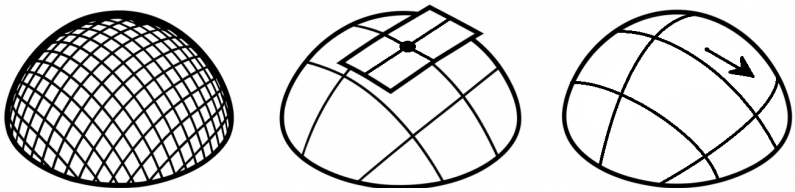

Figure 4.1.: From left to right: A graphical representation of a spherical manifold M, tangent space T_pM at a $p \in M$, and the Hamiltonian vector field X_H evaluated at p, i.e. $X(p) \in T_pM$.

4.3. Classical spin systems as symplectic manifolds

For a system of N classical spins, the phase space is no longer a space of positions and momenta but a product of spheres. Each spin $\mathbf{S}_i \in \mathbb{R}^3$ is a normalized vector ($|\mathbf{S}_i| = 1$) and lies on a 2-sphere S^2. It is convenient to describe a single spin $\mathbf{S} = (S^x, S^y, S^z)$ using spherical coordinates (θ, φ), with

$$S^x = \sin\theta\cos\varphi, \qquad S^y = \sin\theta\sin\varphi, \qquad S^z = \cos\theta.$$

On S^2, the standard area form, which we choose to be the symplectic form, is

$$\omega_{S^2} = \sin\theta\, d\theta \wedge d\varphi.$$

Moreover, S^2 is a complex manifold [Van08, Example 2.1]. We equip S^2 with the standard Riemannian metric [Lee97, Exercise 5.5.7]

$$g_{S^2} = d\theta^2 + \sin^2\theta\, d\varphi^2.$$

Its Riemannian volume form is

$$\mathrm{vol}_{g_{S^2}} = \sin\theta\, d\theta \wedge d\varphi = \omega_{S^2},$$

so the Riemannian volume coincides with the Louiville volume. In this sense g_{S^2} is compatible with the symplectic form ω_{S^2}. On S^2, the induced geodesic distance between two points $\mathbf{u}, \mathbf{v} \in S^2$ is the angle between them,

$$\mathrm{dist}_{S^2}(\mathbf{u}, \mathbf{v}) = \arccos(\mathbf{u} \cdot \mathbf{v}),$$

where the Euclidean inner product on $\mathbb{R}^3$ is used [Lee97, Proposition 5.5.13].

Using the coordinate expression for the Poisson bracket associated with this symplectic form (Appendix A.2, Definition 25), one finds that for observables $f(\theta, \varphi)$ and $g(\theta, \varphi)$ on S^2 the Poisson bracket is

$$\{f, g\} = \frac{1}{\sin\theta}\left(\frac{\partial f}{\partial \theta}\frac{\partial g}{\partial \varphi} - \frac{\partial f}{\partial \varphi}\frac{\partial g}{\partial \theta}\right).$$

To relate this to observables written as functions of the Cartesian spin components S^x, S^y, S^z, we use the chain rule and find that

$$\{S^x, S^y\} = S_z, \quad \{S^x, S^y\} = S_z, \quad \{S^z, S^x\} = S^y.$$

These relations can be compactly written as

$$\dot{S^\alpha} = \{S^\alpha, S^\beta\} = \varepsilon^{\alpha\beta\gamma} S^\gamma, \qquad \alpha, \beta, \gamma \in \{x, y, z\},$$

where $\varepsilon^{\alpha\beta\gamma}$ is the Levi-Civita symbol. For a system of N spins, the entire phase space is the product manifold $(S^2)^N$, which is also complex [Lee24, Example 1.8], and the symplectic form is the sum of the area forms on each sphere,

$$\omega = \sum_{i=1}^{N} \sin\theta_i\, d\theta_i \wedge d\varphi_i.$$

and the product Riemannian metric

$$g = \sum_{i=1}^{N} (d\theta_i^2 + \sin^2\theta_i\, d\varphi_i^2).$$

The corresponding Riemannian volume form is

$$\mathrm{vol}_g = \bigwedge_{i=1}^{N} \sin\theta_i\, d\theta_i \wedge d\varphi_i = \frac{\overbrace{\omega \wedge \cdots \wedge \omega}^{N \text{ times}}}{N!},$$

so g is compatible with ω and the Hamiltonian flow preserves both the Louiville volume and the Riemannian volume. For the metric g on $(S^2)^N$, the induced distance is the ℓ^2–product of the individual S^2-distances, so

$$\mathrm{dist}_g(\mathbf{U}, \mathbf{V}) = \sqrt{\sum_{i=1}^{N} \mathrm{dist}_{S^2}(\mathbf{u}_i, \mathbf{v}_i)^2} = \sqrt{\sum_{i=1}^{N} \arccos\left(\mathbf{u}_i \cdot \mathbf{v}_i\right)^2},$$

for $\mathbf{U} = (\mathbf{u}_1, \ldots, \mathbf{u}_N) \in (S^2)^N$ and $\mathbf{V} = (\mathbf{v}_1, \ldots, \mathbf{v}_N) \in (S^2)^N$ [Ste05, Section 3.9.3].

The corresponding Poisson bracket of two observables $f(\{\theta_i, \varphi_i\})$ and $g(\{\theta_i, \varphi_i\})$ is then

$$\{f, g\} = \sum_{i=1}^{N} \frac{1}{\sin\theta_i} \left(\frac{\partial f}{\partial \theta_i}\frac{\partial g}{\partial \varphi_i} - \frac{\partial f}{\partial \varphi_i}\frac{\partial g}{\partial \theta_i} \right).$$

Since the variables of different spins live on different copies of S^2, the single-spin relations above give

$$\dot{S}_i^\alpha = \{S_i^\alpha, S_j^\beta\} = \delta_{ij}\,\varepsilon^{\alpha\beta\gamma} S_i^\gamma.$$

Finally, the Hamiltonian equations of motion for the spins follow directly from the Poisson bracket. Let $H(\mathbf{S}_1, \ldots, \mathbf{S}_N)$ be the Hamiltonian and consider the time evolution of a single component S_i^α:

$$\dot{S}_i^\alpha = \{S_i^\alpha, H\}.$$

Using the Leibniz rule and the fact that H depends on the spin components, we write

$$\dot{S}_i^\alpha = \sum_\beta \frac{\partial H}{\partial S_i^\beta}\,\{S_i^\alpha, S_i^\beta\} = \sum_{\beta,\gamma} \frac{\partial H}{\partial S_i^\beta}\,\varepsilon^{\alpha\beta\gamma} S_i^\gamma.$$

Introduce the gradient of the Hamiltonian with respect to the i-th spin,

$$\frac{\partial H}{\partial \mathbf{S}_i} \equiv \begin{pmatrix} \dfrac{\partial H}{\partial S_i^x} \\ \dfrac{\partial H}{\partial S_i^y} \\ \dfrac{\partial H}{\partial S_i^z} \end{pmatrix},$$

and recall that the α-component of a cross product is

$$\left(\mathbf{A} \times \mathbf{B}\right)^\alpha = \varepsilon^{\alpha\beta\gamma} A^\beta B^\gamma.$$

Comparing with the expression for $\dot{S}_i^\alpha$ above, we obtain

$$\dot{S}_i^\alpha = \left(\frac{\partial H}{\partial \mathbf{S}_i} \times \mathbf{S}_i \right)^\alpha,$$

which in vector form reads

$$\dot{\mathbf{S}}_i = \frac{\partial H}{\partial \mathbf{S}_i} \times \mathbf{S}_i. \tag{4.2}$$

Thus, each classical spin precesses around the local field $\partial H/\partial \mathbf{S}_i$.

4.4. SYMPLECTIC INTEGRATORS

In many applications one uses general-purpose time-evolution methods such as Runge–Kutta schemes (e.g. RK4) to integrate systems of ordinary differential equations. These methods have well-understood advantages such as having a high order of accuracy, relatively simple implementation, and good short-time error control. However, when applied to Hamiltonian systems they suffer from a fundamental drawback: they do not preserve the underlying symplectic structure.

Let (M, ω) be a $2n$-dimensional symplectic manifold, and let $H\colon M \to \mathbb{R}$ be a smooth Hamiltonian. The Hamiltonian flow φ_t^H generated by H preserves the symplectic form,

$$(\varphi_t^H)^* \omega = \omega,$$

and therefore preserves the associated Liouville volume form. By Liouville's theorem the phase-space volume is exactly conserved by the Hamiltonian dynamics, and the corresponding phase-space probability measure is invariant under the flow.

For such a measure-preserving dynamical system (M, μ, φ_t^H), Oseledets' multiplicative ergodic theorem applies and guarantees the existence of a set of Lyapunov's exponents

$$\lambda_1 \geq \lambda_2 \geq \cdots \geq \lambda_{2n},$$

that describe the average exponential rate at which nearby trajectories in phase space separate or converge under the Hamiltonian dynamics.

A generic, non-symplectic numerical integrator (such as RK4) does not preserve ω and hence does not preserve phase-space volume. The discrete-time map generated by such an integrator is typically not measure-preserving, so one loses the invariant probability measure which underlies the application of Oseledets' multiplicative ergodic theorem. As a consequence, the existence of Lyapunov's exponents for the system is no longer guaranteed, and even when they exist, the symplectic constraints $\sum_i \lambda_i = 0$ and $\lambda_i = -\lambda_{2n+1-i}$ need not hold.

In addition, conserved observables of the system, in particular the Hamiltonian H itself, typically exhibit a drift under non-symplectic schemes when integrated over long times, rather than remaining nearly constant. This long-time drift leads to significant inaccuracies in the properties of the dynamics.

These considerations motivate the use of time-integration schemes which preserve the symplectic form and therefore the phase-space volume. Such schemes are called symplectic integrators. For a modern overview of symplectic integrators we refer to [HLW06, Chapter VI].

A one-step method with step size Δt generates a discrete-time map

$$\Phi_{\Delta t} : M \to M, \qquad z_{k+1} = \Phi_{\Delta t}(z_k).$$

The method is called symplectic if $\Phi_{\Delta t}$ is a symplectic map,

$$\Phi_{\Delta t}^* \omega = \omega$$

for every Δt, here $\Phi_{\Delta t}^*$ denotes the pullback of $\Phi_{\Delta t}$ (Appendix A.2, Definition 30). In this case, the numerical flow is symplectic and therefore preserves the phase-space volume, just as the exact Hamiltonian flow does.

In the following we focus on a specific class of symplectic integrators, namely the second order Suzuki–Trotter time integrator [Suz90; Tro59; Yos90]. However, we first recall the definition and relevant properties of the Liouvillian operator.

4.5. Second order Suzuki-Trotter

Let the smooth function $f : M \to \mathbb{R}$ be an observable. The Hamiltonian flow generated by H induces the evolution

$$\frac{\mathrm{d}}{\mathrm{d}t} f(t) = \{f(t), H\},$$

where $\{\cdot, \cdot\}$ denotes the Poisson bracket. It is convenient to introduce the linear Liouvillian operator $\mathcal{L}_H : C^\infty(M) \to C^\infty(M)$ acting on observables by

$$\mathcal{L}_H f := \{f, H\}.$$

In this notation, the exact time evolution of f can be written as

$$f(t) = e^{t\mathcal{L}_H} f(0), \qquad t \in \mathbb{R}.$$

We now assume that the Hamiltonian splits as

$$H = H_A + H_B,$$

where H_A and H_B are two Hamiltonians whose flows $\varphi_t^{H_A}$ and $\varphi_t^{H_B}$ can be computed exactly. By linearity of the Poisson bracket,

$$\mathcal{L}_H = \mathcal{L}_{H_A} + \mathcal{L}_{H_B},$$

so that

$$f(t) = e^{t(\mathcal{L}_{H_A}+\mathcal{L}_{H_B})} f(0).$$

If $\mathcal{L}_{H_A}$ and $\mathcal{L}_{H_B}$ commuted, we would have the exact factorization

$$e^{t(\mathcal{L}_{H_A}+\mathcal{L}_{H_B})} = e^{t\mathcal{L}_{H_A}} e^{t\mathcal{L}_{H_B}} = e^{t\mathcal{L}_{H_B}} e^{t\mathcal{L}_{H_A}}.$$

For Liouvillian operators this is generically not the case. Using the antisymmetry of the Poisson bracket and the Jacobi identity,

$$\{H_A, \{H_B, f\}\} + \{H_B, \{f, H_A\}\} + \{f, \{H_A, H_B\}\} = 0,$$

we obtain

$$\{\{f, H_B\}, H_A\} = \{H_A, \{H_B, f\}\}, \tag{4.3}$$
$$\{\{f, H_A\}, H_B\} = \{H_B, \{H_A, f\}\}. \tag{4.4}$$

Therefore

$$[\mathcal{L}_{H_A}, \mathcal{L}_{H_B}]f = \mathcal{L}_{H_A}(\mathcal{L}_{H_B} f) - \mathcal{L}_{H_B}(\mathcal{L}_{H_A} f) \tag{4.5}$$
$$= \{H_A, \{f, H_B\}\} - \{H_B, \{f, H_A\}\} \tag{4.6}$$
$$= \{H_A, \{H_B, f\}\} - \{H_B, \{H_A, f\}\} \tag{4.7}$$
$$= -\{f, \{H_A, H_B\}\}. \tag{4.8}$$

Recognizing the Liouvillian operator generated by $\{H_A, H_B\}$,

$$\{f, \{H_A, H_B\}\} = \mathcal{L}_{\{H_A, H_B\}} f,$$

we find the operator identity

$$[\mathcal{L}_{H_A}, \mathcal{L}_{H_B}] = -\mathcal{L}_{\{H_A, H_B\}}.$$

In general $\{H_A, H_B\} \neq 0$, hence $\mathcal{L}_{H_A}$ and $\mathcal{L}_{H_B}$ do not generally commute. Consequently, one must use approximate exponential factorizations for non-commuting operators, such as the second order Suzuki-Trotter factorization [HLW06, Theorem III.5.3.6], which we will now introduce.

As in [BCM24, Section 1.2], the evolution of observables associated with a flow can be written in terms of Lie derivatives. In particular, for the exactly solvable flows $\varphi_t^{H_A}$ and $\varphi_t^{H_B}$ we associate the Lie derivatives F_1, F_2, which in the Hamiltonian case coincide with the Liouvillian operators $\mathcal{L}_{H_A}$, $\mathcal{L}_{H_B}$. The second order Suzuki-Trotter factorization corresponds to the following composition of the flows

$$\varphi_{\Delta t}^{\mathrm{ST}} := \varphi_{\Delta t/2}^{H_A} \circ \varphi_{\Delta t}^{H_B} \circ \varphi_{\Delta t/2}^{H_A},$$

and the associated evolution operator on observables is [BCM24, Equation 1.16]

$$\Psi(\Delta t) = e^{\frac{\Delta t}{2} F_1} e^{\Delta t F_2} e^{\frac{\Delta t}{2} F_1} = e^{\frac{\Delta t}{2} \mathcal{L}_{H_A}} e^{\Delta t \mathcal{L}_{H_B}} e^{\frac{\Delta t}{2} \mathcal{L}_{H_A}}. \tag{4.9}$$

To examine the error of (4.9) with respect to the exact solution of the evolution operator $e^{\Delta t(\mathcal{L}_{H_A}+\mathcal{L}_{H_B})}$, we follow the steps in [BCM24, Section 2.1.1], where φ_h^{ST} is written as $e^{Y(\Delta t)}$ with

$$Y(\Delta t) = \Delta t(F_1+F_2) - \frac{\Delta t^3}{24}[F_1,[F_1,F_2]] - \frac{\Delta t^3}{12}[F_2,[F_1,F_2]] + \cdots .$$

Substituting $F_1 = \mathcal{L}_{H_A}$ and $F_2 = \mathcal{L}_{H_B}$ shows that $\Psi(h)$ agrees with $e^{\Delta t(\mathcal{L}_{H_A}+\mathcal{L}_{H_B})}$ up to terms of order Δt^3. For a more detailed error analysis we refer to [HLW06, Section III.5.1-III.5.3].

Therefore, if we can compute exactly the Hamiltonian flows $\varphi_t^{H_A}$ and $\varphi_t^{H_B}$, the evolution of an observable f over one time step Δt can be approximated to second order by

$$f(\Delta t) = e^{\frac{\Delta t}{2}\mathcal{L}_{H_A}} e^{\Delta t \mathcal{L}_{H_B}} e^{\frac{\Delta t}{2}\mathcal{L}_{H_A}} f(0)$$

Equivalently, in terms of points $p \in M$, one time step is given by

$$p \mapsto \varphi_{\Delta t/2}^{H_A} \circ \varphi_{\Delta t}^{H_B} \circ \varphi_{\Delta t/2}^{H_A}(p).$$

This is precisely the second-order Suzuki–Trotter symplectic integrator for the Hamiltonian $H = H_A + H_B$ [HLW06, Section II.5]. Each of the maps $\varphi_{\Delta t}^{H_A}$ and $\varphi_{\Delta t}^{H_B}$ is an exact Hamiltonian flow and thus symplectic. The composition of symplectic maps is again symplectic, so the numerical one-step map

$$\Phi_{\Delta t} := \varphi_{\Delta t/2}^{H_A} \circ \varphi_{\Delta t}^{H_B} \circ \varphi_{\Delta t/2}^{H_A}$$

is symplectic for every Δt. Consequently, the Suzuki–Trotter scheme preserves the symplectic form ω and the phase-space volume, and it preserves the Lyapunov's exponent constraints, up to inaccuracies arising from the finite step size Δt and method order. Next, we will present a detailed account on Lyapunov's exponents and their properties.

4.6. Lyapunov's exponents

Defined in [Lya92], Lyapunov's exponents describe how sensitive a dynamical system is to small changes in initial data. For Hamiltonian systems, they quantify how small perturbations of a trajectory grow or shrink under the Hamiltonian flow. In this section we briefly recall the Hamiltonian setting, explain the linearized evolution of perturbations, and then state the multiplicative ergodic theorem in terms of the associated linear cocycle and its invariant subspaces. Further, we provide an account of the numerical methods used to calculate all the Lyapunov's exponents for a Hamiltonian system, which are adapted from [PP16, Chapter 3].

The Lyapunov's exponents λ_i describe the average exponential rate at which nearby trajectories in phase space separate or converge under the dynamics. We consider a symplectic manifold M with a Hamiltonian

$$H \in C^2(M, \mathbb{R}),$$

so that the associated Hamiltonian vector field and its flow are sufficiently regular. The Hamiltonian flow

$$\varphi_t : M \to M$$

is defined by following the Hamiltonian equations in time. For a point $p \in M$, the curve $t \mapsto \varphi_t(p)$ is the trajectory starting at p.

A small perturbation of the initial condition p is represented by a tangent vector $v \in T_pM$. To understand Lyapunov's exponents, we track how such perturbations evolve along the trajectory.

The linearized evolution of a perturbation $v \in T_pM$ along the trajectory is given by

$$(d\varphi_t)_p v \in T_{\varphi_t(p)}M,$$

the differential (Jacobian) of the flow at time t applied to v. The map $(d\varphi_t)_p$ is the linear approximation of how the flow changes when we slightly change the initial condition. For a nearby point $p + \varepsilon v$ with small ε,

$$\varphi_t(p + \varepsilon v) - \varphi_t(p) = \varepsilon\,(d\varphi_t)_p v + o(\varepsilon),$$

so $(d\varphi_t)_p v$ gives the first-order change in the evolved state due to the perturbation v. The Lyapunov's exponents quantify how $||(d\varphi_t)_p v||$ grows or decays on average as $t \to \pm\infty$.

4

4.7. THE MULTIPLICATIVE ERGODIC THEOREM.

For Hamiltonian systems, the existence of Lyapunov's exponents is guaranteed by the multiplicative ergodic theorem (Appendix A.3, Theorem 35) [Ose68]. This theorem applies when H is sufficiently regular, for example when $H \in C^2$, and there exists an invariant probability measure for the flow. In the Hamiltonian case, Liouville's theorem (Appendix A.3, Definition 34) provides such a measure by stating that the Hamiltonian flow φ_t preserves phase-space volume.

The multiplicative ergodic theorem is a theorem about linear cocycles over a measure-preserving dynamical system. Given a flow $(\varphi_t)_{t\in\mathbb{R}}$ on M, a (linear) cocycle over φ_t is a family of linear maps

$$A(t,p) : T_pM \to T_{\varphi_t(p)}M, \quad t \in \mathbb{R},\ p \in M,$$

such that

$$A(0,p) = \mathrm{Id}_{T_pM}, \qquad A(t+s,p) = A\big(t, \varphi_s(p)\big) \circ A(s,p) \quad \text{for all } t,s \in \mathbb{R}.$$

In our setting, the base dynamics are given by the Hamiltonian flow φ_t, and the linearized dynamics are given by its differential. The map

$$A(t,p) := (d\varphi_t)_p$$

is a linear map from T_pM to $T_{\varphi_t(p)}M$ and satisfies

$$(d\varphi_{t+s})_p = (d\varphi_t)_{\varphi_s(p)} \circ (d\varphi_s)_p,$$

so $\{(d\varphi_t)_p\}_{t\in\mathbb{R}}$ is a linear cocycle over the Hamiltonian flow. The multiplicative ergodic theorem will be applied to this cocycle.

The multiplicative ergodic theorem states that, for almost every point $p \in M$, the tangent space at p splits into a direct sum of subspaces

$$T_pM = E_1(p) \oplus \cdots \oplus E_{k(p)}(p).$$

Here $k(p)$ is the number of distinct Lyapunov subspaces at the point p. Each $E_i(p)$ corresponds to a different Lyapunov's exponent λ_i and thus to a different asymptotic growth rate. In particular,

$$1 \le k(p) \le \dim M = 2n.$$

The direct sum decomposition means:

1. **Unique decomposition:** Every tangent vector $v \in T_pM$ can be written in a unique way as
$$v = v_1 + \cdots + v_{k(p)}, \quad v_i \in E_i(p).$$

2. **Disjoint:** For $i \neq j$,
$$E_i(p) \cap E_j(p) = \{0\}.$$

Thus the tangent space at p is split into distinct families of directions $E_i(p)$. Each family consists of perturbation directions that share the same asymptotic exponential growth rate under the linearized dynamics.

These subspaces satisfy the invariance property

$$(d\varphi_t)_p\big(E_i(p)\big) = E_i\big(\varphi_t(p)\big) \quad \text{for all } t \in \mathbb{R},\ i = 1, \ldots, k(p).$$

That is, if $v \in E_i(p)$ at time 0, then the evolved vector $(d\varphi_t)_p v$ at time t lies in the corresponding subspace $E_i(\varphi_t(p))$. The flow may stretch or contract vectors in $E_i(p)$, but it does not mix them with directions from any $E_j(p)$ with $j \neq i$.

Each subspace $E_i(p)$ is associated with a Lyapunov's exponent λ_i. Vectors in $E_i(p)$ are precisely those perturbations whose norm, under repeated application of the linearized flow, grows or decays asymptotically at the exponential rate λ_i. More concretely, for $v \in E_i(p) \setminus \{0\}$,

$$\lambda_i = \lim_{t \to \pm\infty} \frac{1}{t} \log ||(d\varphi_t)_p v||,$$

whenever the limit exists. This definition of Lyapunov's exponents uses a norm on each tangent space, and hence depends on a choice of Riemannian metric on M.

The family of subspaces $\{E_i(p)\}$, together with their exponents $\{\lambda_i\}$, thus organizes infinitesimal perturbations according to their long-time growth rates under the linearized Hamiltonian dynamics.

Additionally, the Lyapunov's exponents of a Hamiltonian system are not arbitrary. The Hamiltonian structure imposes three structural constraints on the spectrum.

First, Liouville's theorem (Appendix A.3, Definition 33) states that the Hamiltonian flow φ_t preserves phase-space volume. Consider a small $2n$-dimensional parallelepiped in T_pM, spanned by tangent vectors that we decompose into Oseledets directions. Under the linearized flow, each of these directions is stretched or contracted roughly like $e^{\lambda_i t}$, so the volume of the parallelepiped grows asymptotically like

$$\exp\Big(t \sum_{i=1}^{2n} \lambda_i\Big).$$

Volume preservation means that this volume must remain constant in time, so the exponential factor cannot grow or decay. This forces the sum of all Lyapunov's exponents to vanish (Appendix A.3; Theorem 36):

$$\sum_{i=1}^{2n} \lambda_i = 0.$$

Further, this causes phase space to also become infinitesimally stretched out when there are positive Lyapunov's exponents.

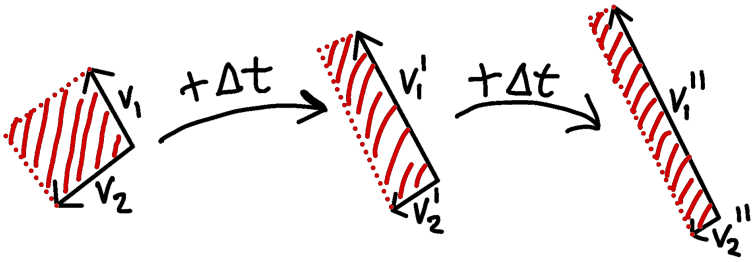

Figure 4.2.: Graphical representation of the time evolution of tangent vectors v_1, v_2 at time $t = \Delta t, 2\Delta t, \ldots$ for a 2-dimensional system, and the parallelepiped spanned by these tangent vectors with constant volume.

Secondly, preservation of the symplectic form ω imposes a pairing between expanding and contracting directions. The nondegeneracy of ω means that for every nonzero tangent vector $v \in T_pM$ there exists a unique tangent vector $w \in T_pM$ such that $\omega(v, \cdot)$ is represented by w. Since the Hamiltonian flow φ_t is symplectic, it preserves ω:

$$\omega\big((d\varphi_t)_p v, (d\varphi_t)_p w\big) = \omega(v, w) \quad \text{for all } t \in \mathbb{R}.$$

If v is expanded asymptotically with rate λ (so $(d\varphi_t)_p v \sim e^{\lambda t}$), then the identity above can only hold if w is contracted at the opposite rate $-\lambda$. Thus, for every positive Lyapunov's exponent there is a corresponding negative exponent of the same multiplicity. As a consequence, the Lyapunov spectrum is symmetric with respect to zero. In particular, after ordering the exponents as $\lambda_1 \geq \cdots \geq \lambda_{2n}$, one has (Appendix A.3; Theorem 40)

$$\lambda_i = -\lambda_{2n+1-i}, \qquad i = 1, \ldots, n.$$

Finally, every independent integral of motion produces an additional pair of vanishing Lyapunov's exponents. Let $I : M \to \mathbb{R}$ be a smooth conserved quantity, $I \circ \varphi_t = I$. Trajectories are confined to the level set

$$I^{-1}(c) = \{p \in M : I(p) = c\},$$

that is, the subset of phase space on which I takes the constant value c. The Hamiltonian vector field generating φ_t is everywhere tangent to $I^{-1}(c)$. A perturbation proportional to this vector field is equivalent to a small time shift along the same trajectory. The perturbed trajectory is therefore just the reference trajectory with a slightly shifted time origin, so the separation does not grow exponentially in time, and therefore has Lyapunov exponent 0. To see that there is also a transverse zero exponent associated with I, note that for constant c the set $I^{-1}(c)$ is a smooth $(\dim M - 1)$-dimensional surface in phase space. At each point of this surface there is a single direction perpendicular to it, and this normal direction is precisely the one given by ∇I. Since $I \circ \varphi_t = I$, the derivative of I in this normal direction is preserved along the flow, so the component of any perturbation normal to $I^{-1}(c)$ cannot grow or decay exponentially without changing the value of I. This normal direction therefore carries Lyapunov exponent 0. Each independent integral of motion therefore contributes at least two zero exponents: one along the flow and one normal to the corresponding invariant set $I^{-1}(c)$ in the above sense. In particular, in our case the Hamiltonian H is conserved, so there are already two zero exponents on the energy shell $H^{-1}(E)$: one along the Hamiltonian flow and one associated with the normal direction determined by ∇H (Appendix A.3, Theorem 41).

4.8. KOLMOGOROV-SINAI ENTROPY

An additional measure of dynamical complexity is the Kolmogorov-Sinai entropy H_{KS}, which quantifies the average rate of information production in a dynamical system. Intuitively, the Kolmogorov-Sinai entropy measures how rapidly two initially close trajectories become distinguishable when one observes the system with finite resolution. A larger Kolmogorov-Sinai entropy corresponds to a faster loss of predictability and hence to stronger chaos. For smooth, ergodic dynamical systems with a well-defined Lyapunov spectrum, Pesin's theorem [Pes77] establishes that the KS entropy can be expressed as the sum of all positive Lyapunov exponents: $H_{\mathrm{KS}}=\sum_{\lambda_i>0}\lambda_i$. In practice, this result allows one to estimate the Kolmogorov-Sinai entropy numerically by computing the Lyapunov spectrum and summing its positive components [ER85].

4.9. FINITE-TIME LYAPUNOV'S EXPONENTS

The limit definition of Lyapunov's exponents above can be interpreted directly in terms of the separation of two nearby trajectories. We fix a smooth Riemannian metric g on M, and denote by $\mathrm{dist}(\cdot,\cdot)$ the induced distance on M by the metric g and by $||\cdot||$ the induced norm for tangent vectors. Fix a point $p \in M$ and a direction $v \in T_pM$. For a small parameter $\delta_0 > 0$, consider a second point p_{δ_0} which is obtained by moving p for δ_0 time along the geodesic starting at p in the direction v. Then, the distance between the two points is

$$\delta_0 = \mathrm{dist}(p, p_{\delta_0}).$$

We obtain the points $\varphi_t(p)$ and $\varphi_t(p_{\delta_0})$ after evolving the two initial conditions for time t, and we denote their distance by

$$\delta_t(\delta_0) := \mathrm{dist}\big(\varphi_t(p), \varphi_t(p_{\delta_0})\big).$$

Since φ_t is differentiable with respect to the initial condition (Appendix A.2, Definition 29), we can write a first-order Taylor expansion of φ_t around p in the direction v in local coordinates:

$$\varphi_t(p_{\delta_0}) = \varphi_t(p) + \delta_0 (d\varphi_t)_p v + \mathcal{O}(\delta_0^2).$$

Subtracting $\varphi_t(p)$, dividing by δ_0, and taking the limit $\delta_0 \to 0$ yields

$$\lim_{\delta_0 \to 0} \frac{1}{\delta_0}\big(\varphi_t(p_{\delta_0}) - \varphi_t(p)\big) = (d\varphi_t)_p v.$$

The geodesic distance between $\varphi_t(p)$ and $\varphi_t(p_{\delta_0})$ is given to first order by the norm of the displacement vector, hence

$$\delta_t(\delta_0) = \mathrm{dist}\big(\varphi_t(p), \varphi_t(p_{\delta_0})\big) = \delta_0 \, ||(d\varphi_t)_p v|| + \mathcal{O}(\delta_0^2),$$

and therefore

$$\lim_{\delta_0 \to 0} \frac{\delta_t(\delta_0)}{\delta_0} = ||(d\varphi_t)_p v||.$$

This motivates the standard finite-time Lyapunov's exponent, defined via

$$\lambda_T(p, v) := \lim_{\delta_0 \to 0} \frac{1}{T} \log \frac{\delta_T(\delta_0)}{\delta_0} = \frac{1}{T} \log ||(d\varphi_T)_p v||.$$

For fixed p and a direction v lying in one of the Lyapunov subspaces $E_i(p)$, we then let the time T become large. Under the assumptions of the multiplicative ergodic

theorem, this finite-time quantity converges for almost every p and every nonzero $v \in E_i(p)$ to the corresponding Lyapunov's exponent:

$$\lambda_i = \lim_{T\to\pm\infty} \lambda_T(p, v) = \lim_{T\to\pm\infty} \frac{1}{T} \log\left(\frac{\operatorname{dist}(\varphi_T(p), \varphi_T(p_{\delta_0}))}{\operatorname{dist}(p, p_{\delta_0})}\right),$$

for any fixed $\delta_0 > 0$ sufficiently small. The limit only depends on the subspace $E_i(p)$ that contains the initial perturbation v, not on the particular choice of $v \in E_i(p)\setminus\{0\}$. In this sense, the Lyapunov's exponent λ_i is the asymptotic exponential rate at which the distance between two trajectories, initially separated by δ_0 in a direction belonging to $E_i(p)$, grows or decays as time evolves.

4.10. Calculating Lyapunov's exponents on bounded phase space

Theoretically, the task of calculating all the Lyapunov's exponents for an unbounded phase space is rather straight forward. For a $2n$-dimensional phase space M one simply picks points $p, p_1, \ldots, p_{2n} \in M$ such that for some sufficiently small $\delta_0 > 0$, every p_i is obtained by moving p for δ_0 time along the geodesic starting at p in the direction $v_i \in E_i(p)$. Then one finds all Lyapunov's exponents as the limit of the finite-time Lyapunov's exponents

$$\lambda_i = \lim_{T\to\pm\infty} \lambda_T(p, v_i) = \lim_{T\to\pm\infty} \frac{1}{T} \log\left(\frac{\operatorname{dist}(\varphi_t(p), \varphi_t(p_i))}{\operatorname{dist}(p, p_i)}\right).$$

There is one significant advantage when we are working in a compact symplectic manifold. The limit definition of Lyapunov's exponents is dependent on a choice of Riemannian metric. However, when M is compact, any two smooth Riemannian metrics g_1 and g_2 on M are uniformly equivalent in the sense that there exist constants $0 < c \le C < \infty$ such that their induced norms satisfy

$$c\,||v||_{g_1} \le ||v||_{g_2} \le C\,||v||_{g_1} \qquad \text{for all } p \in M,\ v \in T_pM,$$

where the constants c and C can be chosen independently of p [Heb00, Section 2.2]. If the Lyapunov's exponents are computed using $||\cdot||_{g_1}$ and $||\cdot||_{g_2}$ respectively, then for the associated cocycle $(d\varphi_t)_p$ we apply the above inequality and obtain

$$c\,||(d\varphi_t)_p v||_{g_1} \le ||(d\varphi_t)_p v||_{g_2} \le C\,||(d\varphi_t)_p v||_{g_1}.$$

Taking logarithms and subtracting $\log||(d\varphi_t)_p v||_{g_1}$ yields

$$\log c \le \log||(d\varphi_t)_p v||_{g_2} - \log||(d\varphi_t)_p v||_{g_1} \le \log C.$$

Hence

$$\left|\log||(d\varphi_t)_p v||_{g_2} - \log||(d\varphi_t)_p v||_{g_1}\right| \le \max\{|\log c|, |\log C|\},$$

Dividing by $t > 0$ gives

$$\left|\frac{1}{t}\log||(d\varphi_t)_p v||_{g_1} - \frac{1}{t}\log||(d\varphi_t)_p v||_{g_2}\right| \le \frac{1}{t}\max\{|\log c|, |\log C|\},$$

which converges to 0 as $t \to \infty$ for every nonzero $v \in T_pM$. Thus, on a compact symplectic manifold, the limits defining the Lyapunov's exponents are independent of the particular smooth Riemannian metric used to define the norm on each tangent space [Fro84; Kat80].

However, for bounded phase spaces, such as for spin systems, there is one significant drawback due to $\operatorname{dist}(\varphi_t(p), \varphi_t(p_i))$ increasing exponentially when $\lambda_i > 0$ and approaching the maximum separation between points in the phase space for

some finite time, and does not meaningfully capture the exponential separation any more. One insight that circumvents the problem of a uniform bound on $\mathrm{dist}(\cdot,\cdot)$ is by using the cocycle property of the differential of the flow, and observing that we can decompose

$$(d\varphi_T)_p = (d\varphi_{N\tau})_p = (d\varphi_\tau)_{\varphi_{(N-1)\tau}(p)} \circ \cdots \circ (d\varphi_\tau)_{\varphi_\tau(p)} \circ (d\varphi_\tau)_p.$$

For convenience, define

$$A_k := (d\varphi_\tau)_{\varphi_{k\tau}(p)}, \qquad k = 0, 1, \ldots, N-1,$$

so that

$$(d\varphi_{N\tau})_p = A_{N-1} \circ \cdots \circ A_1 \circ A_0.$$

Then

$$\lambda_i = \lim_{N\to\infty} \frac{1}{N\tau} \log ||A_{N-1} \circ \cdots \circ A_1 \circ A_0\, v_i||.$$

The expression above suggests interpreting λ_i as an average of local stretching rates. To make this explicit, we factor out the growth at each step. For now, we consider a single vector v_i. We introduce a sequence $\{\hat{v}_i^{(k)}\}_{k\geq 0}$ of rescaled tangent vectors with a fixed small norm $\delta_0 > 0$:

$$\hat{v}_i^{(0)} := \delta_0 \frac{v_i}{||v_i||}, \qquad ||\hat{v}_i^{(k)}|| = \delta_0 \quad \text{for all } k.$$

Given $\hat{v}_i^{(k)}$, we apply the linearized map over one time step:

$$w_{ik} := A_k \hat{v}_i^{(k)} = (d\varphi_\tau)_{\varphi_{k\tau}(p)} \hat{v}_i^{(k)}.$$

We then define the local stretching factor

$$\alpha_{ik} := \frac{||w_{ik}||}{\delta_0} > 0,$$

and rescale to obtain the next vector of norm δ_0:

$$\hat{v}_i^{(k+1)} := \delta_0 \frac{w_{ik}}{||w_{ik}||}.$$

By construction, $||\hat{v}_i^{(k)}|| = \delta_0$ for all k. An inductive argument shows that

$$A_{N-1} \cdots A_1 A_0\, \hat{v}_i^{(0)} = \left(\prod_{k=0}^{N-1} \alpha_k \right) \hat{v}_i^{(N)}.$$

Since $\hat{v}_i^{(0)} = \delta_0 v_i / ||v_i||$, we have

$$A_{N-1} \cdots A_1 A_0\, v_i = \frac{||v||}{\delta_0} A_{N-1} \cdots A_1 A_0\, \hat{v}_i^{(0)} = \frac{||v_i||}{\delta_0} \left(\prod_{k=0}^{N-1} \alpha_{ik} \right) \hat{v}_i^{(N)}.$$

Taking norms and using $||\hat{v}_i^{(N)}|| = \delta_0$ gives

$$||A_{N-1} \cdots A_1 A_0\, v_i|| = \frac{||v_i||}{\delta_0} \left(\prod_{k=0}^{N-1} \alpha_{ik} \right) ||\hat{v}_i^{(N)}|| = ||v|| \prod_{k=0}^{N-1} \alpha_{ik}.$$

Therefore,

$$\frac{1}{N\tau}\log||A_{N-1}\cdots A_1A_0\,v_i|| = \frac{1}{N\tau}\log||v_i|| + \frac{1}{N\tau}\sum_{k=0}^{N-1}\log\alpha_{ik}.$$

In the limit $N\to\infty$, the contribution $\frac{1}{N\tau}\log||v_i||$ vanishes, and we obtain

$$\lambda_i = \lim_{N\to\infty}\frac{1}{N\tau}\sum_{k=0}^{N-1}\log\alpha_{ik}, \qquad \alpha_{ik} = \frac{||(d\varphi_\tau)_{\varphi_{k\tau}(p)}\hat{v}_i^{(k)}||}{\delta_0}.$$

The quantity

$$\frac{1}{\tau}\log\alpha_{ik} = \frac{1}{\tau}\log\frac{||(d\varphi_\tau)_{\varphi_{k\tau}(p)}\hat{v}_i^{(k)}||}{\delta_0}$$

can be interpreted as the local stretching rate over the time interval $[k\tau,(k+1)\tau]$ along the direction $\hat{v}_i^{(k)}$. The Lyapunov's exponent λ_i is then the long-time average of these local stretching rates:

$$\lambda_i = \lim_{N\to\infty}\frac{1}{N}\sum_{k=0}^{N-1}\frac{1}{\tau}\log\frac{||(d\varphi_\tau)_{\varphi_{k\tau}(p)}\hat{v}_i^{(k)}||}{\delta_0}.$$

In the case of a single exponent, this repeated rescaling keeps the perturbation norm fixed at δ_0. For the full spectrum $\lambda_1,\ldots,\lambda_n$, one propagates a basis of tangent vectors $v_1,\ldots,v_n$ and repeatedly rescales them, recording the corresponding local stretching factors for each direction.

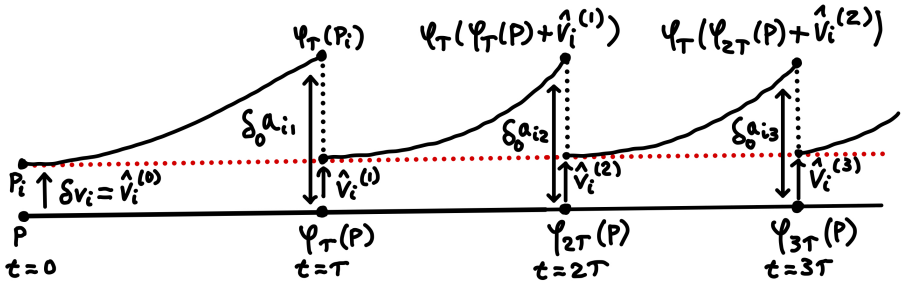

Figure 4.3.: Graphical representation of the time evolution of initially nearby trajectories while periodically rescaling at $t=\tau,2\tau,3\tau,\ldots$.

4.11. Calculating Lyapunov's exponents with finite precision

To practically calculate all the Lyapunov's exponents $\lambda_1,\ldots,\lambda_{2n}$, there is one more issue we need to address. If we simply propagate and rescale several tangent vectors $v_1,\ldots,v_{2n}$ independently, without enforcing any orthogonality, we run into a major problem. Due to the presence of numerical rounding errors, all tangent vectors tend to align with the fastest expanding subspace $E_1(p)$ associated with the largest Lyapunov exponent λ_1. Even if the initial vectors v_i are carefully chosen to lie in different Lyapunov's subspaces $E_i(p)$, finite precision and the different growth rates imply that, after sufficiently many steps, the component along $E_1(p)$ dominates in each v_i, and the remaining components become negligible numerically. As a result, the algorithm effectively converges only to the largest Lyapunov's exponent λ_1.

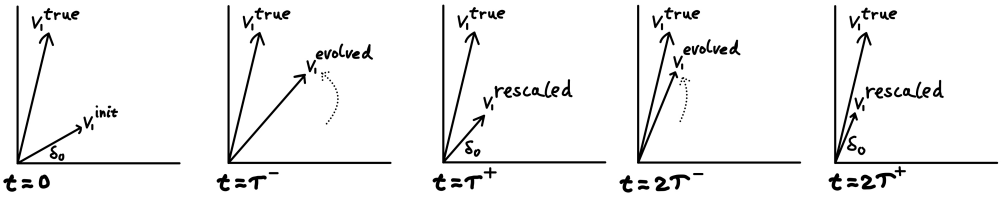

Figure 4.4.: Graphical representation of the eventually convergence of some arbitrary tangent vector v_1^{init} to $v_1^{\text{true}} \in E_1(p)$ over multiple rescaling events at $t = \tau, 2\tau, \dots$.

4

The goal is to ensure that, over long times, one vector converges to $E_1(p)$, another to $E_2(p)$, and so on, so that each v_i eventually aligns (and remains aligned) with the corresponding subspace $E_i(p)$. To achieve this, we start at time $t = 0$ with n tangent vectors

$$v_1, \dots, v_{2n} \in T_pM$$

that are mutually orthogonal with respect to the Riemannian metric g. Without loss of generality, we may think of v_1 as the vector that will eventually align with $E_1(p)$ under the dynamics. After evolving the system over a time step τ, the images $(d\varphi_\tau)_p v_i$ have, due to the dominance of the most unstable direction and numerical imprecision, all acquired significant components along $E_1(p)$. If we remove from each $(d\varphi_\tau)_p v_j$ the projection onto $(d\varphi_\tau)_p v_1$, then over long times only the evolved v_1 can align with $E_1(p)$: the others are continually forced to lie in directions transverse to $E_1(p)$.

Repeating this idea, we also remove from $(d\varphi_\tau)_p v_j$ the projections onto $(d\varphi_\tau)_p v_1$ and $(d\varphi_\tau)_p v_2$ for $j \geq 3$, and so on. Inductively, this ensures that v_2 aligns with $E_2(p)$, v_3 with $E_3(p)$, etc. This procedure is nothing other than a Gram–Schmidt orthogonalization applied after each propagation step. It stabilizes the tangent vectors and allows us to separate the different growth directions associated with the full Lyapunov's spectrum.

When $\delta_0 \ll 1$, we may interpret $v_1, \dots, v_{2n}$ as vectors in euclidean space, since the curvature is negligible. From a linear algebra point of view, the Gram-Schmidt procedure applied to a collection of linearly independent vectors $w_1, \dots, w_{2n} \in \mathbb{R}^{3n}$ is equivalent to computing a QR decomposition of the $3n \times 2n$ matrix $W = [w_1 \dots w_{2n}]$. (In the next section, we will choose each $w_1, \dots, w_n$ to represent a different tangent vector.) Concretely, Gram-Schmidt produces an orthonormal family $q_1, \dots, q_{2n}$ and scalars r_{ij} such that

$$W = QR, \qquad Q = [q_1 \dots q_{2n}] \in \mathbb{R}^{3n \times 2n}, \quad R = (r_{ij}) \in \mathbb{R}^{2n \times 2n},$$

where $Q^T Q = I_{2n}$ and R is upper triangular with $r_{ij} = q_i^T w_j$ for $i \leq j$ and $r_{ij} = 0$ for $i > j$. In numerical practice, this factorization is usually computed by QR algorithms such as Householder reflections rather than by the classical Gram–Schmidt procedure, because the explicit QR viewpoint leads to algorithms that control loss of orthogonality much better in finite machine precision. As a result, QR-based orthogonalization is significantly more stable and reliable when n is large.

4.12. Calculation scheme for classical spin systems

We now specialize the above construction to a classical spin system with N spins. The phase space is

$$M = (S^2)^N \subset \mathbb{R}^{3N},$$

but each spin $\boldsymbol{S}_i \in S^2$ is constrained to have unit length, so the phase space has $2N$ degrees of freedom. Consequently, there are $2N$ Lyapunov's exponents

$$\lambda_1 \geq \lambda_2 \geq \cdots \geq \lambda_{2N}.$$

We will use the standard algorithm for computing the full Lyapunov spectrum via periodic QR orthogonalization of tangent vectors [PP16, Section 3.2] adapted to the phase space $(S^2)^N$. However, in our calculation scheme we do not construct the tangent vectors explicitly. Instead, we evolve one reference trajectory and $2N$ nearby trajectories at distance δ_0 from the reference, and reconstruct approximate tangent vectors at each reorthogonalization time by taking differences between the reference and the nearby trajectories. These differences are arranged as columns of a $3N \times 2N$ matrix and orthogonalized by a QR decomposition. The upper triangular factor contains the local stretching factors whose long-time averages give the Lyapunov's exponents.

REPRESENTATION OF DEVIATIONS

Let

$$\boldsymbol{S}(t) = \big(\boldsymbol{S}_1(t), \ldots, \boldsymbol{S}_N(t)\big) \in (S^2)^N \subset \mathbb{R}^{3N}$$

denote the reference trajectory, where each spin $\boldsymbol{S}_i(t) \in \mathbb{R}^3$ satisfies $||\boldsymbol{S}_i(t)|| = 1$. We choose $2N$ nearby trajectories

$$\boldsymbol{S}^{(j)}(t), \qquad j = 1, \ldots, 2N,$$

with initial conditions at $t = 0$ such that

$$\delta_0 = ||\boldsymbol{S}^{(j)}(0) - \boldsymbol{S}(0)||$$

for all j, where $||\cdot||$ is the Euclidean norm on $\mathbb{R}^{3N}$. For small enough δ_0, the differences

$$\Delta\boldsymbol{S}^{(j)}(t) := \boldsymbol{S}^{(j)}(t) - \boldsymbol{S}(t) \in \mathbb{R}^{3N}, \qquad j = 1, \ldots, 2N,$$

approximate the evolution of $2N$ linearly independent tangent vectors.

At a given time $t_k = k\tau$, we collect these deviations into a $3N \times 2N$ matrix

$$W^{(k)} := \big(\Delta\boldsymbol{S}^{(1)}(t_k), \ldots, \Delta\boldsymbol{S}^{(2N)}(t_k)\big),$$

whose j-th column is the deviation of the j-th nearby trajectory from the reference trajectory. Note that, although $W^{(k)}$ lives in $\mathbb{R}^{3N\times 2N}$, its rank is at most $2N$, reflecting the $2N$ physical degrees of freedom.

INITIALIZATION OF NEARBY TRAJECTORIES

At the initial time $t_0 = 0$ we construct the $2N$ nearby trajectories in a symmetric way. Starting from a given reference configuration $\boldsymbol{S}(0)$, we first clone it to all trajectories:

$$\boldsymbol{S}^{(j)}(0) \leftarrow \boldsymbol{S}(0), \qquad j = 1, \ldots, 2N.$$

We then perturb the spins one by one. For each spin index $i \in \{1, \ldots, N\}$ we create two nearby trajectories by rotating only the i-th spin of the reference configuration while leaving all other spins unchanged.

More precisely, for each spin i we choose a small rotation angle $\theta_0 > 0$ and define two perturbed configurations:

- one trajectory where $\boldsymbol{S}_i(0)$ is rotated by $+\theta_0$ with respect to the $\hat{y}$-axis,

- one trajectory where $\boldsymbol{S}_i(0)$ is rotated by θ_0 with respect to the $\hat{z}$-axis,

The angle θ_0 is chosen such that each perturbed configuration has Euclidean distance

$$||\boldsymbol{S}^{(j)}(0) - \boldsymbol{S}(0)|| = \delta_0$$

from the reference configuration. This construction yields $2N$ nearby trajectories whose deviations form a well-conditioned initial set of approximate tangent vectors of norm δ_0. Then, a single QR step, before starting the time evolution, is performed to ensure that all these approximate tangent vectors become orthogonal. This QR step is not used in the calculation of Lyapunov's exponents.

SINGLE QR STEP

Assume that at time t_k the deviations have already been orthogonalized and rescaled so that

$$W^{(k)} = Q^{(k)}\delta_0,$$

where $Q^{(k)}$ is a $3N \times 2N$ matrix whose columns are orthonormal in $\mathbb{R}^{3N}$ and each column has norm $||\boldsymbol{q}_j^{(k)}|| = 1$. Equivalently, the columns of $W^{(k)}$ have norm δ_0 and are mutually orthogonal.

One QR step from t_k to $t_{k+1} = t_k + \tau$ consists of the following operations:

1. **Propagation of trajectories.** Evolve the reference and all nearby trajectories with the same integrator over the time interval $[t_k, t_{k+1}]$:

$$\boldsymbol{S}(t_k) \mapsto \boldsymbol{S}(t_{k+1}), \qquad \boldsymbol{S}^{(j)}(t_k) \mapsto \boldsymbol{S}^{(j)}(t_{k+1}), \quad j = 1, \ldots, 2N.$$

2. **Construction of deviations.** Form the new deviation matrix

$$W^{(k+1)} := \left(\Delta\boldsymbol{S}^{(1)}(t_{k+1}), \ldots, \Delta\boldsymbol{S}^{(2N)}(t_{k+1})\right),$$

where

$$\Delta\boldsymbol{S}^{(j)}(t_{k+1}) := \boldsymbol{S}^{(j)}(t_{k+1}) - \boldsymbol{S}(t_{k+1}).$$

3. **Orthogonalization through QR decomposition.** Compute the QR decomposition of the $3N \times 2N$ matrix $W^{(k+1)}$:

$$W^{(k+1)} = Q^{(k+1)}R^{(k+1)},$$

where

- $Q^{(k+1)}$ is a $3N \times 2N$ matrix with orthonormal columns (so $(Q^{(k+1)})^\top Q^{(k+1)} = I_{2N}$),
- $R^{(k+1)}$ is a $2N \times 2N$ upper triangular matrix with positive diagonal entries

$$r_{ii}^{(k+1)} > 0, \qquad i = 1, \ldots, 2N.$$

The matrix $Q^{(k+1)}$ provides a new orthonormal basis of deviation directions, and the diagonal elements of $R^{(k+1)}$ encode the local stretching factors along these directions over the time step $[t_k, t_{k+1}]$.

4. **Rescaling and reconstruction of nearby trajectories.** To keep the deviations small and well within the linear regime, we reset the nearby trajectories so that their deviations from the reference have norm δ_0 and directions given by the columns of $Q^{(k+1)}$. Let $\boldsymbol{q}_j^{(k+1)}$ denote the j-th column of $Q^{(k+1)}$. We define new nearby trajectories at time t_{k+1} by

$$\boldsymbol{S}^{(j)}(t_{k+1}) \leftarrow \Pi\big(\boldsymbol{S}(t_{k+1}) + \delta_0\, \boldsymbol{q}_j^{(k+1)}\big), \qquad j = 1, \dots, 2N,$$

where Π denotes the operation of normalizing each spin $\boldsymbol{S}_i$ to unit length. With this rescaling, the updated deviation matrix becomes

$$W_{\text{reset}}^{(k+1)} = Q^{(k+1)}\delta_0,$$

ready for the next propagation step.

Note that although $W^{(k+1)}$ has size $3N \times 2N$, the upper triangular matrix $R^{(k+1)}$ is only $2N \times 2N$. Thus, at each step we obtain exactly $2N$ diagonal elements $r_{ii}^{(k+1)}$ corresponding to the $2N$ Lyapunov's exponents of the system. The embedding dimension $3N$ only affects the size of the orthonormal basis $Q^{(k+1)}$.

PHASE SPACE VOLUME AND LYAPUNOV'S EXPONENTS

Over K such QR steps, with total integration time $T = K\tau$, we obtain a sequence of upper triangular matrices

$$R^{(1)}, R^{(2)}, \dots, R^{(K)},$$

each with diagonal entries $r_{ii}^{(k)} > 0$ for $i = 1, \dots, 2N$ and $k = 1, \dots, K$. The diagonal coefficients $r_{ii}^{(k)}$ encode the change of the phase space volume element spanned by the $2N$ deviation vectors. Indeed, the $2N$ columns of $W^{(k)}$ span a $2N$-dimensional parallelepiped in $\mathbb{R}^{3N}$ whose volume (in the induced Euclidean metric) is

$$V^{(k)} = \left|\det R^{(k)}\right| = \prod_{i=1}^{2N} r_{ii}^{(k)}.$$

Finally, the Lyapunov's exponents are given by the time-averaged logarithmic growth of these diagonal entries:

$$\lambda_i = \lim_{K\to\infty} \frac{1}{K\tau} \sum_{k=1}^{K} \log r_{ii}^{(k)}, \qquad i = 1, \dots, 2N.$$

In practice, for a finite integration time $T = K\tau$, we approximate

$$\lambda_i^{(T)} := \frac{1}{K\tau} \sum_{k=1}^{K} \log r_{ii}^{(k)}, \qquad i = 1, \dots, 2N,$$

and monitor convergence as T increases.

Finally, we note the we are using the second-order Suzuki-Trotter numerical scheme while carrying out this calculation. Due to this calculation of Lyapunov's exponents generally requiring simulations over relatively long periods of time, we make use of the following identity,

$$\Phi_{N\Delta t} = \varphi_{\Delta t/2}^{H_A} \circ \varphi_{\Delta t}^{H_B} \circ \varphi_{\Delta t}^{H_A} \circ \varphi_{\Delta t}^{H_B} \cdots \circ \varphi_{\Delta t}^{H_B} \circ \varphi_{\Delta t}^{H_A} \circ \varphi_{\Delta t}^{H_B} \circ \varphi_{\Delta t/2}^{H_A},$$

for N time steps of size Δt, which provides a significant improvement of the numerical scheme's efficiency. However, we must remind ourselves to apply the aforementioned QR step and calculate the finite-time Lyapunov's exponent only at integer multiples of Δt. Therefore, we structure the method as follows

$$\Phi_{N\Delta t} = \Phi_{\tau\Delta t} \circ (\text{QR step}) \circ \Phi_{\tau\Delta t} \circ (\text{QR step}) \circ \cdots \circ \Phi_{\tau\Delta t} \circ (\text{QR step}),$$

where τ denotes the amount of time steps of size Δt before we apply the QR step and calculate the finite-time Lyapunov's exponents.

5

INVESTIGATIONS OF LYAPUNOV'S EXPONENTS IN SPIN GLASS SHARDS

To restate our goal, we aim to gain insight in the connection between signatures of chaos between a quantum many-body system and its classical many-body counterpart. Specifically, we focus on the spin glass shards system in a random transverse magnetic field studied by Georgeot and Shepelyansky [GS98]. In the quantum regime, one signature of chaos is given by energy-level spacing statistics and their crossover from Poissonian behavior, typical of integrable regimes, to GOE statistics with strong level repulsion. The system of interest crosses between the integrable magnetic, chaotic, and integrable spin-spin regimes, see figure 3.4.

In parallel, we construct and simulate the corresponding classical Hamiltonian system (5.1) and quantify its dynamics via Lyapunov's exponents computed using the methods described in section (4.12). By comparing quantum energy-level spacing statistics and classical Lyapunov's exponents across many disorder realizations and system parameter choices, we aim to identify how changing the global system parameters and local disorder parameters simultaneously influences the onset of classical chaos, and to map regions of parameter and phase space that are effectively integrable or chaotic.

To further specify, we are studying the classical analog of the quantum system introduced in section 3.4. The model is defined, for N classical spins, by the Hamiltonian

$$H = \sum_{i<j} J_{ij} S_i^x S_j^x + \sum_{i=1}^{N} \Gamma_i S_i^z := H_A + H_B, \tag{5.1}$$

where the first sum runs over all distinct spin pairs. This model represents a classical spin glass shard interacting with a random transverse magnetic field. The random transverse magnetic field is represented by the coefficients Γ_i which are drawn independently from a uniform distribution in the interval $[0, \Gamma_{\max}]$. The exchange interactions J_{ij} are taken to be independent random variables uniformly distributed in the interval $[-J_{\max}/\sqrt{N}, J_{\max}/\sqrt{N}]$. The $1/\sqrt{N}$ factor ensures the energy per spin H/N stays finite rather than diverging with system size. In this way one obtains a well-defined thermodynamic limit as $N \to \infty$. For later convenience we introduce the parameter

$$R := \frac{J_{\max}}{J_{\max} + \Gamma_{\max}}.$$

$R \approx 0$ corresponds to a system dominated by the transverse magnetic field, while $R \approx 1$ corresponds to a system dominated by the spin-spin coupling.

In this model the randomness is quenched: the couplings J_{ij} and local fields Γ_i are randomly drawn once and then kept fixed during the time evolution of the system. A single choice of all $\{J_{ij}\}$ and $\{\Gamma_i\}$ at fixed $J, \Gamma > 0$ is called a realization of disorder.

Because the couplings J_{ij} have random signs, the system is generally frustrated: it is not possible to choose spin orientations that simultaneously minimize all pairwise interaction terms. Consequently, for J not too small compared to Γ, the ground state is typically spin glass-like rather than a simple ferromagnetic or antiferromagnetic configuration. Only in the strong-field limit $\Gamma \gg J$ does one recover a field-polarized ground state, with spins aligned mostly along the transverse field direction.

The Hamiltonian H can be split into two parts, H_A and H_B. The equations of motion for these parts are obtained by applying equation (4.2), from which it follows that

$$\left(\frac{d\mathbf{S}_i}{dt}\right)_{H_A} = \frac{\partial H_A}{\partial \mathbf{S}_i} \times \mathbf{S}_i, \qquad \frac{\partial H_A}{\partial \mathbf{S}_i} = \begin{pmatrix} \sum_{j \neq i} J_{ij} S_j^x \\ 0 \\ 0 \end{pmatrix},$$

and

$$\left(\frac{d\mathbf{S}_i}{dt}\right)_{H_B} = \frac{\partial H_B}{\partial \mathbf{S}_i} \times \mathbf{S}_i, \qquad \frac{\partial H_B}{\partial \mathbf{S}_i} = \begin{pmatrix} 0 \\ 0 \\ \Gamma_i \end{pmatrix}.$$

Thus, $\varphi_{\Delta t}^{H_A}$ (resp. $\varphi_{\Delta t}^{H_B}$) from the sympectic integrator is realized by rotating each spin $\mathbf{S}_i$ around the x-axis (resp. z-axis) by an angle

$$\theta_i^{(H_A)} = \Big(\sum_{j \neq i} J_{ij} S_j^x\Big)\Delta t, \qquad \theta_i^{(H_B)} = \Gamma_i \Delta t.$$

All data underlying the results presented is available at [Hui25].

5.1. NUMERICAL VALIDATION

For the second-order Suzuki–Trotter time integration scheme (Section 4.5) and the calculation scheme for the Lyapunov's exponents (Section 4.12) we adopt the following notation: the parameter T denotes the total time duration of the simulation, the parameter Δt denotes the duration of a single time step, τ denotes the number of time steps between successive QR orthogonalization steps, and δ_0 denotes the initial deviation between the reference trajectory $\mathbf{S}(0)$ and the perturbed spin configurations. We denote by $\langle H \rangle$ and $\langle \log V \rangle$ the time-averaged Hamiltonian and the time-averaged natural logarithm of the phase-space volume, respectively. In the following, we determine suitable choices of these numerical parameters such that the integration remains stable, in the sense that the phase-space volume is approximately preserved, the Hamiltonian exhibits bounded fluctuations around a constant mean without systematic drift, and the sum of all Lyapunov's exponents converges to zero within numerical accuracy.

CONSERVATION PROPERTIES OF THE INTEGRATOR

We start by validating the phase volume V and Hamiltonian H values that are obtained during the simulation. For $N = 17$ and $\delta_0 = 10^{-4}$ we expect

$$\langle \log V \rangle \approx 2N \log \delta_0 \approx -313.152,$$

which is consistent with the numerical results shown in figures 5.1b and 5.1d. The amplitude of the fluctuations of $\log V$ around its mean is approximately an order of magnitude larger for the RK4 time integrator than for the second-order Suzuki–Trotter scheme.

Moreover, a drawback of the non-symplectic RK4 integrator is immediately visible in figure 5.1c: the Hamiltonian H exhibits an approximately linear drift in time. In contrast, the second-order Suzuki–Trotter integrator yields a Hamiltonian that remains bounded and fluctuates around a constant mean, see figure 5.1a. However, we do note that the drift associated with the RK4 integrator is an order of magnitude smaller than the observed fluctuations with the second-order Suzuki-Trotter integrator.

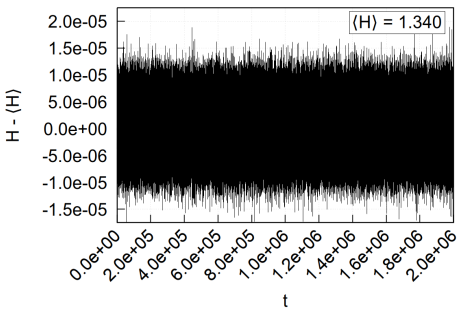

(a) Second-order Suzuki–Trotter; Hamiltonian fluctuations.

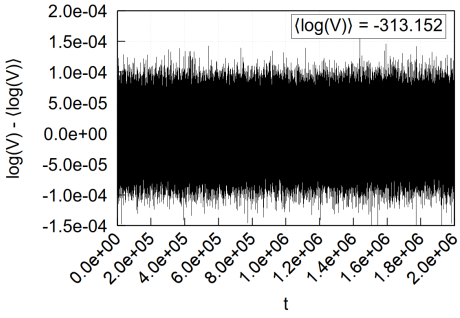

(b) Second-order Suzuki–Trotter; Phase space volume fluctuations.

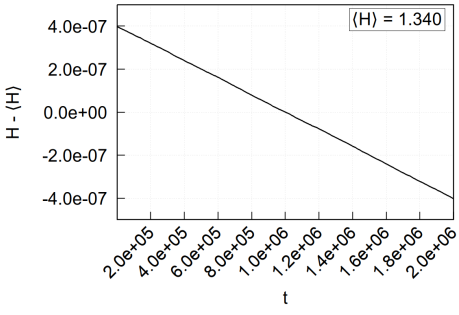

(c) RK4; Hamiltonian drift.

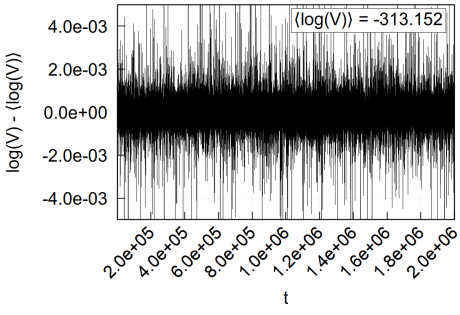

(d) RK4; Phase space volume fluctuations.

Figure 5.1.: Results for $N = 17$, $\Delta t = 10^{-2}$, $\tau = 50$, $\delta_0 = 10^{-4}$, $J_{\max} = 1$ and $\Gamma_{\max} = 1$ ($R = 0.5$).

DEPENDENCE ON TIME STEP

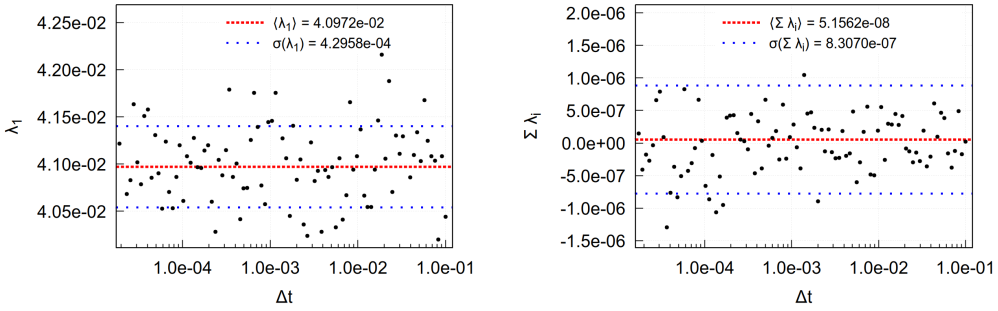

Figure 5.2.: Results for $N = 17$, $T = 10^4$, $\tau = 0.5/\Delta t$, $\delta_0 = 10^{-4}$, $J_{\max} = 1$ and $\Gamma_{\max} = 1$ ($R = 0.5$).

5

From figures 5.2 and 5.3 we observe that, for the 17-spin system, the choice of time step Δt has a negligible effect on the maximal Lyapunov's exponent λ_1, on the total sum $\sum_{i=1}^{34} \lambda_i$, and on $\langle \log V \rangle$.

Furthermore, we recall that τ counts the number of time integration steps before reorthogonalizing the tangent vectors in the Lyapunov's exponent calculation procedure. In our implementation we represent tangent vectors as small deviations between trajectories, which is only valid as long as these deviations remain sufficiently small so that the curvature of phase space is negligible. Keeping the product $\tau\Delta t$, the physical time interval between successive QR orthogonalization steps, constant ensures that changing Δt does not change how long the deviations are physically allowed to evolve before being orthogonalized. If $\tau\Delta t$ is too large, the deviations can potentially grow for too long between orthogonalizations such that deviations will no longer accurately represent elements of tangent space. We observe in figure 5.3, for which we fix $\tau\Delta t = 0.5$, that as a consequence of not letting deviations grow for too long that tangent space is sufficiently well approximated due to the observed preservation of phase-space volume.

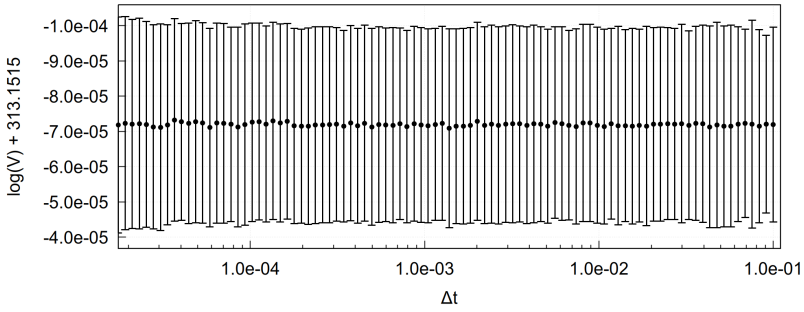

Figure 5.3.: Results for $N = 17$, $T = 10^4$, $\tau = 0.5/\Delta t$, $\delta_0 = 10^{-4}$, $J_{\max} = 1$ and $\Gamma_{\max} = 1$ ($R = 0.5$).

In contrast, we observe in figure 5.4 that the mean value of the Hamiltonian $\langle H \rangle$

does depend on Δt. For $\Delta t \gg 10^{-2}$ we observe a pronounced deviation of $\langle H \rangle$ from its reference value. Moreover, the standard deviation $\sigma(H)$ grows approximately quadratically with the time step as $\sigma(H) \propto \Delta t^2$.

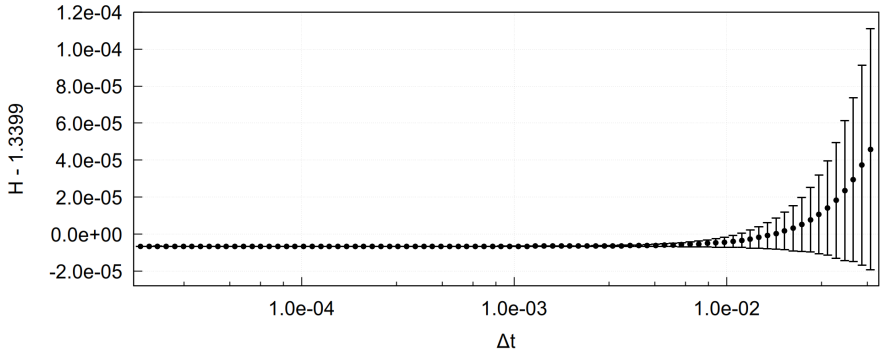

(a)

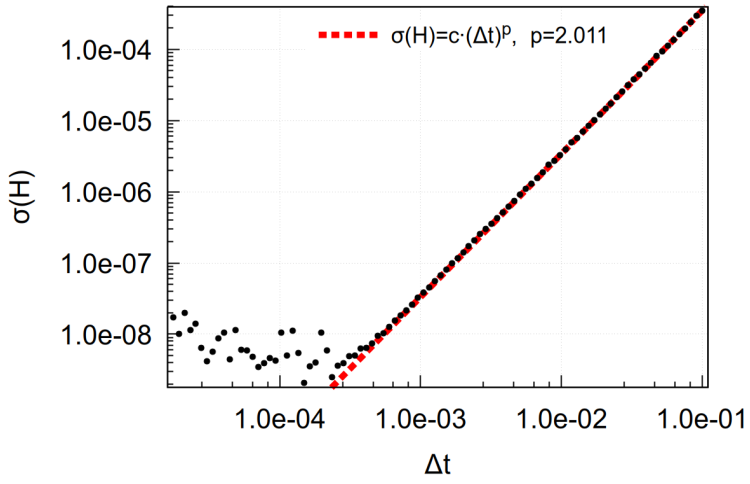

(b)

Figure 5.4.: Results for $N = 17$, $T = 10^4$, $\tau = 0.5/\Delta t$, $\delta_0 = 10^{-4}$, $J_{\max} = 1$ and $\Gamma_{\max} = 1$ ($R = 0.5$).

DEPENDENCE ON RESET INTERVAL

Next, we fix $\Delta t = 10^{-3}$ and vary the reset interval τ. Over the range considered, τ has a negligible influence on the mean and standard deviation of the Hamiltonian H. However, beyond a certain threshold the preservation of phase-space volume deteriorates. As shown in figure 5.5a, the phase-space volume is approximately conserved for $\tau \leq 500$, while for $\tau > 500$ systematic deviations appear. Furthermore, figure 5.5b indicates an approximately linear growth of the standard deviation $\sigma(\log V)$ with τ.

The maximal Lyapunov's exponent λ_1 remains essentially constant for $\tau \leq 200$, but starts to deviate for larger reset intervals $t > 500$, see figure 5.5c. The

dependence of $\left|\sum_{i=1}^{34} \lambda_i\right|$ on τ is more complex. The sum attains a minimum near $\tau \approx 100$. For smaller τ the sum increases again, possibly because the reorthogonalization interval is too short to clearly numerically distinguish between linear and exponential separation of deviation trajectories. For larger τ the sum also increases, which may be attributed to the deviations between trajectories becoming too large, such that tangent space vectors are no longer properly approximated by deviations due to the local curvature of phase space. To balance numerical accuracy and computational efficiency, we use $\tau = 500$ as an upper bound in the simulations and adopt $\tau\Delta t = 0.5$ as the maximal reorthogonalization time.

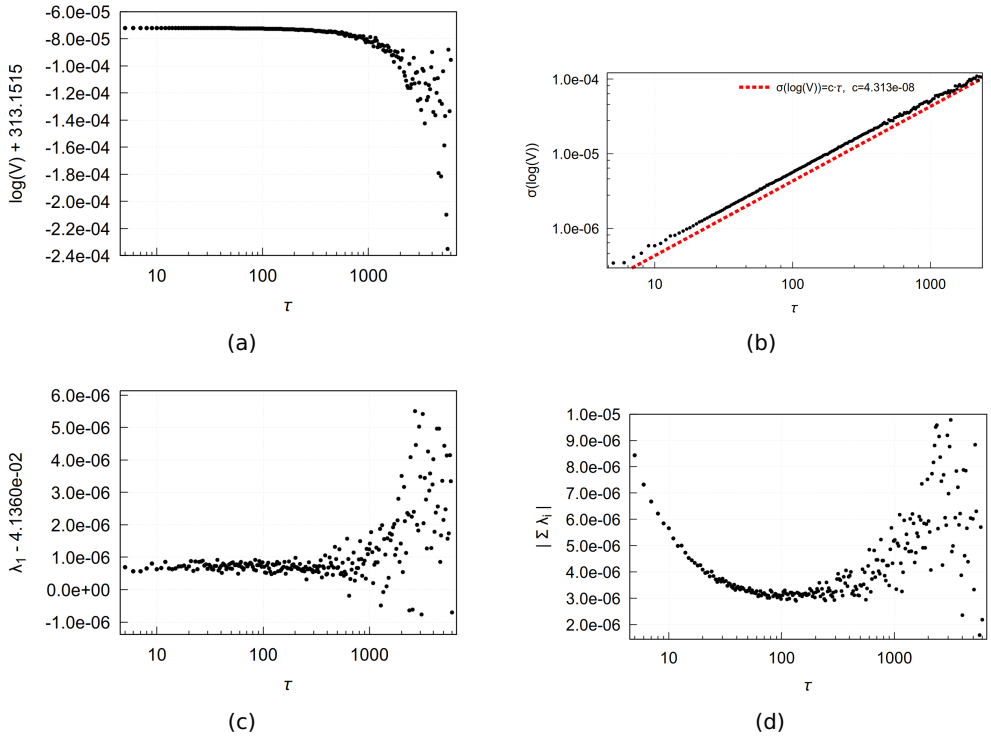

Figure 5.5.: Results for $N = 17$, $\Delta t = 10^{-3}$, $\delta_0 = 10^{-4}$, $J_{\max} = 1$ and $\Gamma_{\max} = 1$.

DEPENDENCE ON INITIAL SEPARATION

Finally, we briefly mention the role of the initial separation δ_0 observed during our investigation. For $10^{-7} \leq \delta_0 \leq 10^{-2}$ the simulations are generally stable. For the 17-spin system, the Lyapunov spectrum and phase-space volume statistics are largely insensitive to δ_0 within this range. For larger spin systems, however, smaller initial separations are required for numerical stability, typically $\delta_0 \ll 10^{-3}$. For the remaining simulations δ_0 is set equal to 10^{-4}.

5.2. EXAMPLES OF LYAPUNOV SPECTRA

Having validated our choice of numerical parameters, we next examine several representative realizations of the spin glass dynamics. In figure 5.6a we show the time evolution of the finite-time Lyapunov's exponents for a system with $N = 17$

and coupling parameter $R = 0.5$, for which we expect influences from both the spin-spin coupling and the transverse magnetic field. The exponents initially exhibit substantial fluctuations, but gradually converge towards approximately stationary values as the elapsed time increases.

A more detailed view is provided in figure 5.6b, where the Lyapunov's exponents and time are plotted on a logarithmic scale. We observe that two exponents continue to approach zero, in agreement with the theoretical prediction of two vanishing Lyapunov's exponents for this system (Appendix A.3, Theorem 41), while the remaining exponents reach quasi-stationary values and no longer change significantly in time.

The final finite-time approximation of the Lyapunov spectrum is displayed in figure 5.6. The numerical Lyapunov spectrum satisfies the expected properties: it is symmetric, its sum is (within numerical accuracy) equal to zero, and it contains precisely two exponents that are numerically close to zero. Moreover, the presence of a strictly positive maximal Lyapunov's exponent, $\lambda_1 \approx 0.04$, indicates that the corresponding dynamics are chaotic.

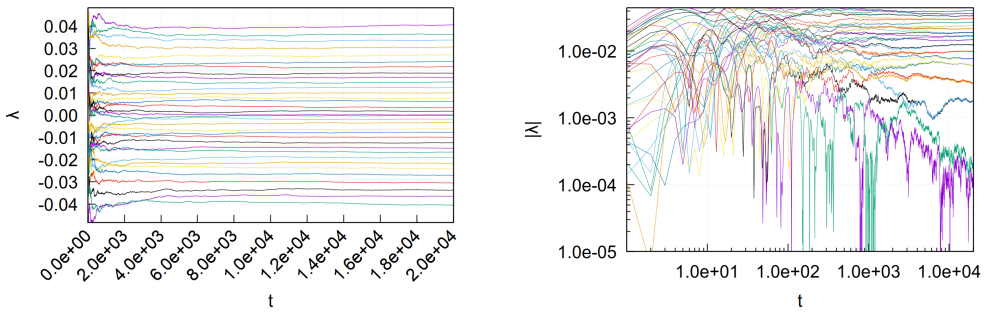

(a) (b)

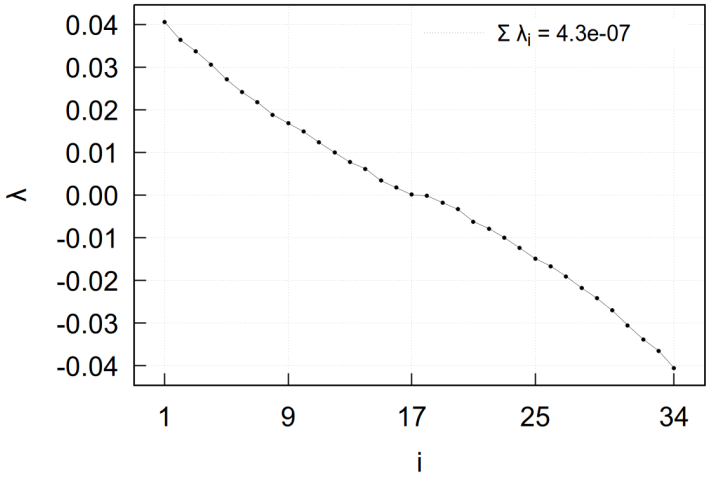

(c)

Figure 5.6.: Results for $N = 17$, $\Delta t = 2.15 \cdot 10^{-4}$, $\tau = 2321$, $\delta_0 = 10^{-4}$, $J_{\max} = 1$ and $\Gamma_{\max} = 1$ ($R = 0.5$).

In figures 5.7a and 5.7b we show the time evolution of the finite-time Lyapunov's exponents for a classical spin glass system with $N = 17$ and coupling parameter $R = 1$, a regime in which the dynamics are expected to be integrable. In this case, the spins predominantly precess around the x-axis due to the dominant spin-spin coupling. We observe, as expected, that the finite-time Lyapunov's exponents clearly converge towards zero as the elapsed time increases. This behavior is clearly visible in the logarithmic representation in figure 5.7b, where all exponents continue to decrease and approach zero, in agreement with the absence of chaotic dynamics in the integrable regime.

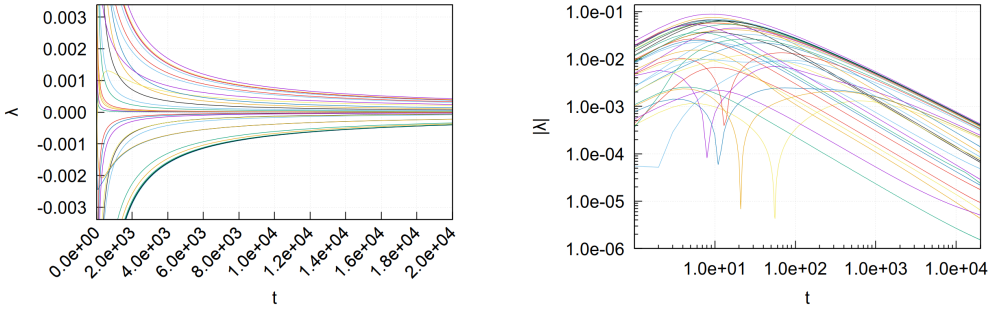

(a) (b)

Figure 5.7.: Results for $N = 17$, $\Delta t = 2.15 \cdot 10^{-4}$, $\tau = 2321$, $\delta_0 = 10^{-4}$, $J_{\max} = 1$ and $\Gamma_{\max} = 0$ ($R = 1$).

In figures 5.8a and 5.8b we show the time evolution of the finite-time Lyapunov's exponents for a classical system of spins in a transverse magnetic field with $N = 17$ and coupling parameter $R = 0$, a regime in which the dynamics are also expected to be integrable. In this case, the spins predominantly precess around the z-axis due to the dominant transverse magnetic field.

The finite-time Lyapunov's exponents rapidly decay and converge towards zero as the elapsed time increases, in agreement with the absence of chaotic behavior. Moreover, compared to the spin-spin coupling dominated case ($R = 1$), the absolute values of the exponents in this system ($R = 0$) are approximately five orders of magnitude smaller at the last timestep, indicating a significantly faster convergence to zero.

Having examined one chaotic realization ($R = 0.5$) and two integrable limits ($R = 0; R = 1$) of the dynamics, we now turn to an intermediate regime that exhibits a mixture of integrable and chaotic behavior. In figures 5.9a and 5.9b we show the time evolution of the finite-time Lyapunov's exponents for a classical system of spins in a transverse magnetic field with $N = 17$ and coupling parameter $R = 0.0909$. This parameter choice interpolates between the purely magnetic field-driven and the strongly interacting spin-spin regimes and is therefore expected to generate mixed dynamical behavior.

The corresponding finite-time Lyapunov spectrum at the end of the simulation is shown in figure 5.9c. A substantial fraction of the Lyapunov's exponents are close to zero, indicating tangent-space directions associated with nearly integrable or weakly chaotic motion. In contrast, a subset of exponents attains clearly non-zero values, signaling directions in phase space for which nearby trajectories separate exponentially.

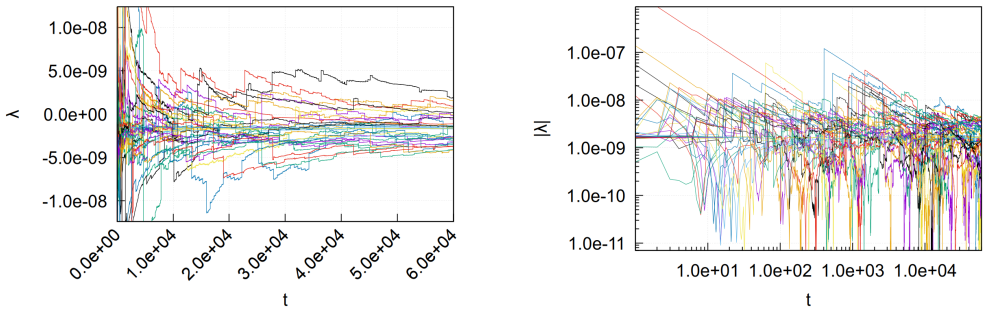

(a) (b)

Figure 5.8.: Results for $N = 17$, $\Delta t = 2.15 \cdot 10^{-4}$, $\tau = 2321$, $\delta_0 = 10^{-4}$, $J_{\max} = 0$ and $\Gamma_{\max} = 1$ ($R = 0$).

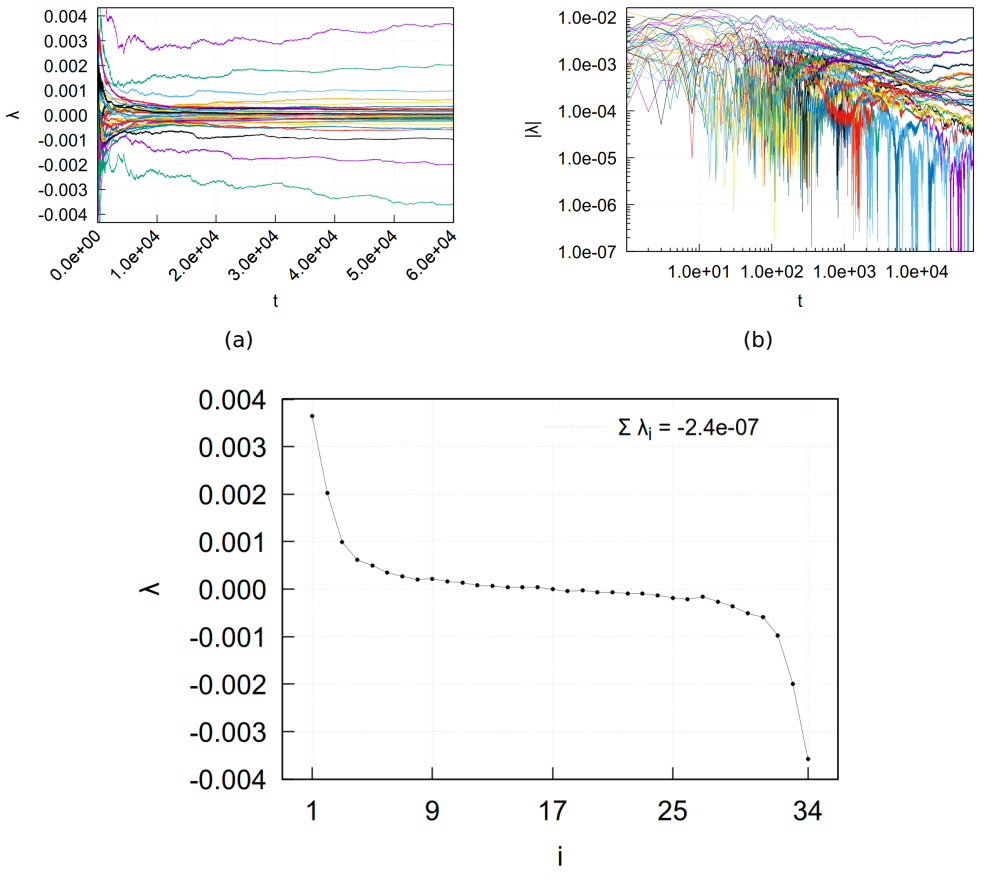

(a) (b)

(c)

Figure 5.9.: Results for $N = 17$, $\Delta t = 2.15 \cdot 10^{-4}$, $\tau = 2321$, $\delta_0 = 10^{-4}$, $J_{\max} = 1$ and $\Gamma_{\max} = 10$ ($R = 0.0909$).

LARGER NUMBER OF SPINS

To demonstrate the capability of the present approach, we compute the full Lyapunov spectrum for a system with $N = 100$ spins and coupling parameter $R = 0.5$. The resulting spectrum satisfies all expected structural constraints: it is symmetric, its sum is (within numerical accuracy) equal to zero, and it contains precisely two exponents that converge to zero, as illustrated in figure 5.7b.

The computation of Lyapunov spectra for such large systems is, however, numerically demanding, owing to both the long integration times required for convergence and the cost of repeated QR decompositions in a high-dimensional tangent space. In the remainder of this work we therefore focus on the $N = 17$ spin system, which is also the second-largest amount of spins examined in [GS98].

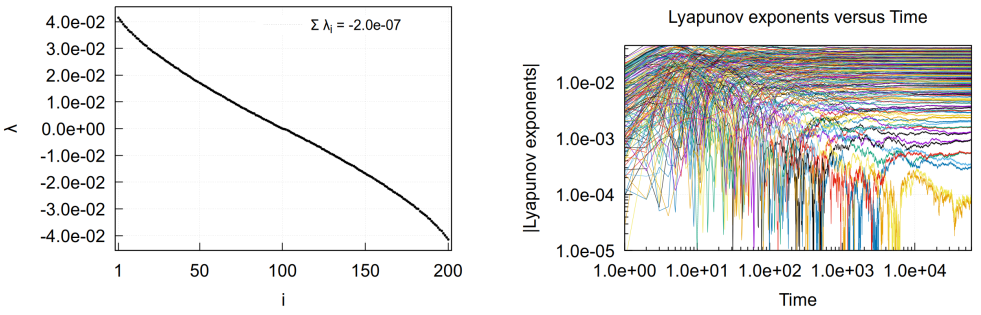

(a) (b)

Figure 5.10.: Results for $N = 100$, $\Delta t = 10^{-4}$, $\tau = 5000$, $\delta_0 = 10^{-4}$, $J_{\max} = 1$ and $\Gamma_{\max} = 1$ ($R = 0.5$).

5.3. LYAPUNOV SPECTRA FOR PHASE SPACE ENSEMBLES

We expect the phase space of our classical spin system to contain regions in which either predominantly integrable or chaotic dynamics are present. Intuitively, configurations with spins oriented closer to the z-axis are expected to be more strongly influenced by the transverse magnetic field, whereas configurations closer to the x-axis are expected to be dominated by the spin-spin coupling. To quantitatively inspect these distinct regions, we introduce three different ensembles of initial configurations in phase space, each sampling a specific region of interest, see figure 5.11.

The first ensemble is the uniform ensemble, for each spin $\mathbf{S}_i$ one samples polar and azimuthal angles (θ_i, ϕ_i) with $\cos\theta_i$ uniformly distributed in $[-1, 1]$ and ϕ_i uniformly distributed in $[0, 2\pi)$, and set $\mathbf{S}_i = (\sin\theta_i \cos\phi_i, \sin\theta_i \sin\phi_i, \cos\theta_i)$.

The second and third ensembles concentrate the sampling near a specific direction in spin space. In the z-focused ensemble, we fix the z-component of each spin to a prescribed value

$$S_i^z = 1 - \Delta z, \qquad \Delta z \in [0, 2],$$

and sample the components (S_i^x, S_i^y) uniformly on the corresponding circle of radius $\sqrt{1-(1-\Delta z)^2}$ in the xy-plane. Concretely, this can be implemented by choosing an angle $\phi_i \in [0, 2\pi)$ uniformly at random for each spin and setting

$$S_i^x = \sqrt{1-(1-\Delta z)^2}\cos\phi_i, \qquad S_i^y = \sqrt{1-(1-\Delta z)^2}\sin\phi_i.$$

In the x-focused ensemble, we instead fix

$$S_i^x = 1 - \Delta x, \qquad \Delta x \in [0, 2],$$

and sample (S_i^y, S_i^z) uniformly on the circle of radius $\sqrt{1-(1-\Delta x)^2}$ in the yz-plane by choosing $\phi_i \in [0, 2\pi)$ uniformly and setting

$$S_i^y = \sqrt{(}1-(1-\Delta x)^2 \cos\phi_i, \qquad S_i^z = \sqrt{1-(1-\Delta x)^2}\sin\phi_i.$$

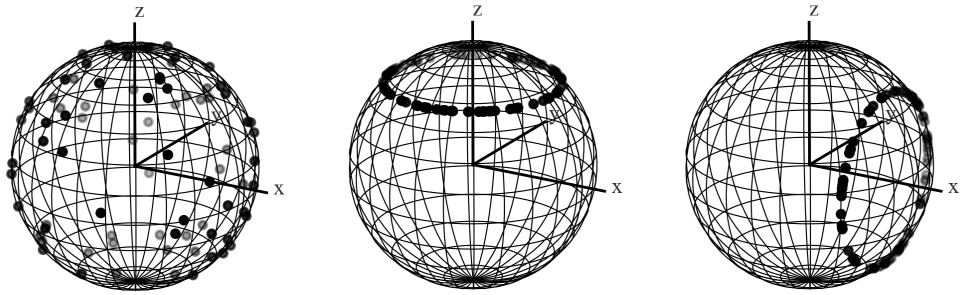

Figure 5.11.: A graphical representation of each ensemble, a dot representing a sampled point of a trajectory. The uniform, z-focused and x-focused ensemble are shown in the respective left, middle and right image.

TYPICAL TRAJECTORIES IN DIFFERENT ENSEMBLES

We first consider spin trajectories initialized in the uniform ensemble, where a single spin configuration is sampled uniformly on the unit sphere. When $R = 0.75$, indicating that both the magnetic field and spin-spin coupling are dominant, we observe in figure 5.12a that the spin trajectory explores a substantial part of the entire phase space. This indicates that the associated energy shell is effectively spread over a large region of phase space, consistent with chaotic dynamics.

When the coupling parameter is increased to $R = 0.975$, the system is placed in a nearly integrable regime dominated by the spin-spin interaction, the qualitative nature of the motion changes significantly. As illustrated in figure 5.12b, the trajectory of the same spin, started from the same initial configuration in the uniform ensemble, becomes confined to a comparatively small subset of phase space and is characterized by quasi-periodic precession around the x-axis, which is expected for this specific choice of R.

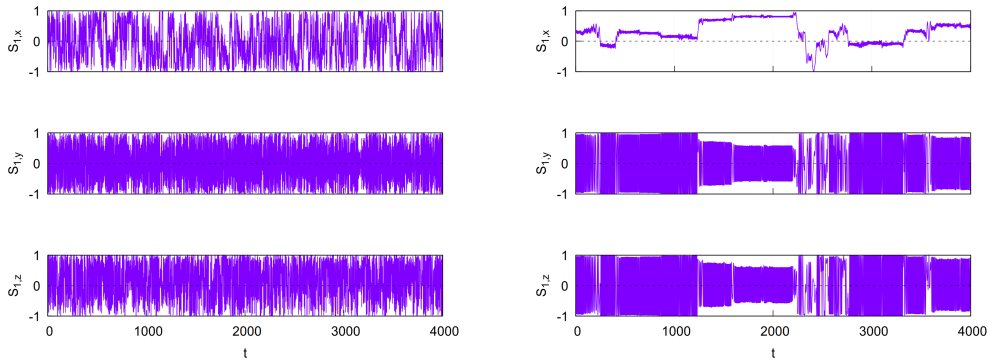

(a) $\Gamma_{\max} = 0.33$ ($R = 0.75$). (b) $\Gamma_{\max} = 0.02564$ ($R = 0.975$).

Figure 5.12.: Spin coordinates of the first spin $\mathbf{S}_1$ over time for a trajectory from the uniform ensemble. Chosen parameters are $N = 17$, $\Delta t = 10^{-3}$, $\tau = 500$, $\delta_0 = 10^{-4}$ and $J_{\max} = 1$. More trajectories are provided in appendix A.2.

5

To further illustrate the qualitative behavior of typical trajectories, we focus on the z-focused ensemble for several representative values of R and Δz. For $\Delta z = 0.05$ and $R = 0.2$, the trajectory of a single spin, shown in figure 5.13a, remains close to the z-axis and exhibits predominantly quasi-periodic precessions around the z-axis, as expected for a nearly integrable regime in which the transverse magnetic field is dominant.

Increasing the coupling parameter to $R = 0.5$, while keeping the same initial spin configuration for $\Delta z = 0.05$, leads to a distinctly different behavior (figure 5.13b): the trajectory becomes more irregular and explores a larger fraction of the accessible phase space, although its support on the energy shell is still largely confined to the upper hemisphere.

Another picture emerges when the system is evolved in a regime where the spin-spin interactions dominate. In figures 5.13c ($\Delta z = 0.05$) and 5.13d ($\Delta z = 0.01$), trajectories initialized in the z-focused ensemble are shown for $R = 0.975$. Although the spins are initially aligned predominantly with the transverse magnetic field, the subsequent dynamics are rapidly governed by the spin-spin coupling. Consequently, the long-time motion is characterized by quasi-periodic precession around the x-axis.

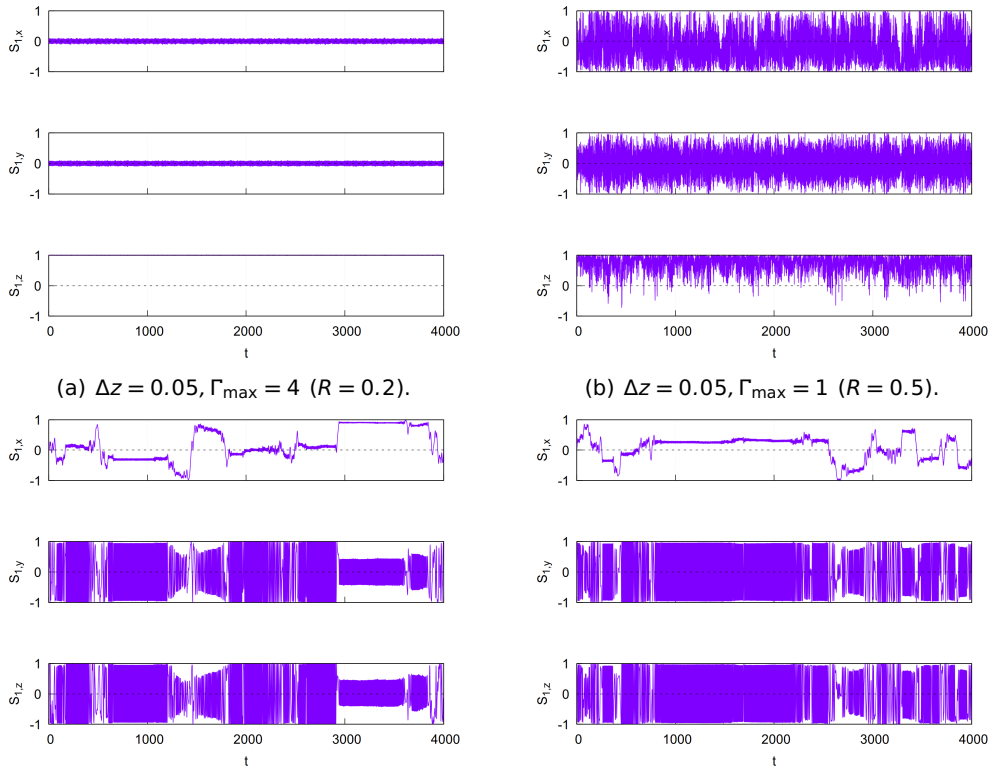

(a) $\Delta z = 0.05, \Gamma_{\max} = 4$ $(R = 0.2)$.

(b) $\Delta z = 0.05, \Gamma_{\max} = 1$ $(R = 0.5)$.

(c) $\Delta z = 0.01, \Gamma_{\max} = 0.0256$ $(R = 0.975)$.

(d) $\Delta z = 0.05, \Gamma_{\max} = 0.0256$ $(R = 0.975)$.

Figure 5.13.: Spin coordinates of the first spin $\mathbf{S}_1$ over time for a trajectory from the z-focused ensemble. Chosen parameters are $N = 17$, $\Delta t = 10^{-3}$, $\tau = 500$, $\delta_0 = 10^{-4}$ and $J_{\max} = 1$. For $\Delta z = 0.01$, more trajectories are provided in appendix A.3.

LYAPUNOV SPECTRA IN DIFFERENT ENSEMBLES

Having examined the typical trajectories, we now turn to the Lyapunov spectra for spin configurations initialized in the uniform ensemble. In figures 5.14a, 5.14b and 5.14c we show the final finite-time Lyapunov spectra for $R = 0.2$, $R = 0.75$ and $R = 0.975$, respectively. For $R = 0.2$ and $R = 0.75$ the Lyapunov's exponents form a relatively compact band, with no clear separation into distinct groups, indicating that the typical trajectories sampled by the uniform ensemble exhibit comparable dynamics.

In contrast, for $R = 0.975$ we observe a bimodal structure in the spectrum. Some trajectories have clearly positive Lyapunov's exponents, indicative of chaotic dynamics, while others have significantly smaller exponents that cluster near zero, indicative of integrable dynamics. This splitting suggests that, for this specific disorder realization, in the regime where the spin-spin coupling is dominant but a weak transverse magnetic field is still present, spin configurations sampled from the uniform ensemble can exhibit qualitatively different dynamical behaviour, ranging from strongly chaotic to nearly integrable.

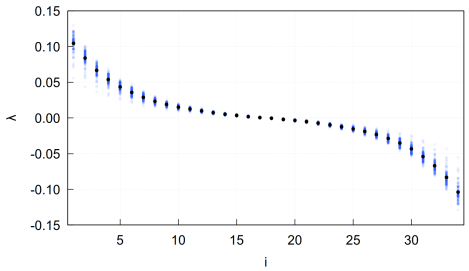

(a) $\Gamma_{\max} = 4$ ($R = 0.2$).

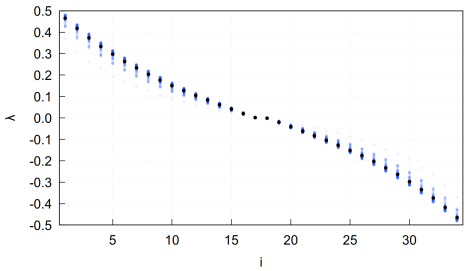

(b) $\Gamma_{\max} = 0.33$ ($R = 0.75$).

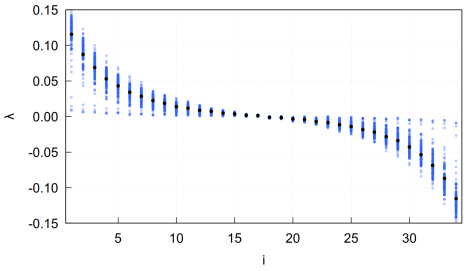

(c) $\Gamma_{\max} = 0.02564$ ($R = 0.975$).

Figure 5.14.: The Lyapunov's exponents for 100 trajectories (blue dots) from the uniform ensemble and each exponent's average (black dot). Chosen parameters are $N = 17$, $\Delta t = 10^{-3}$, $\tau = 500$, $\delta_0 = 10^{-4}$ and $J_{\max} = 1$. More Lyapunov spectra are provided in appendix A.1a.

For trajectories initialized in the z-focused ensemble ($\Delta z = 0.05$), we do not observe a bimodal Lyapunov spectrum, see figure 5.15. Instead, as shown in figure 5.15a, the tangent space contains a larger number of directions with Lyapunov's exponents close to zero for $R = 0.2$ than in the corresponding uniform ensemble case. This indicates that the initial coupling to the transverse magnetic field remains dynamically dominant over long times, leading to dynamics that are close to integrable.

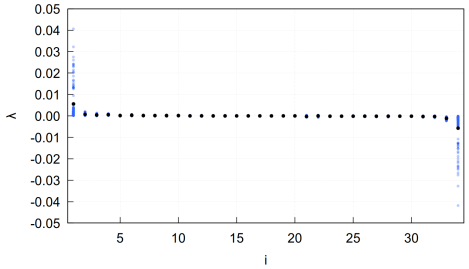

(a) $\Delta z = 0.05, \Gamma_{\max} = 4$ $(R = 0.2)$.

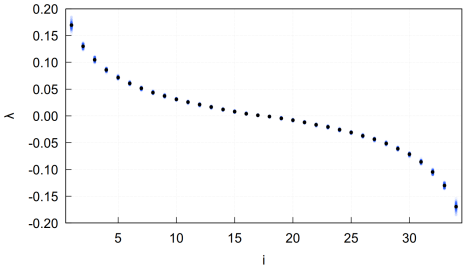

(b) $\Delta z = 0.05, \Gamma_{\max} = 1$ $(R = 0.5)$.

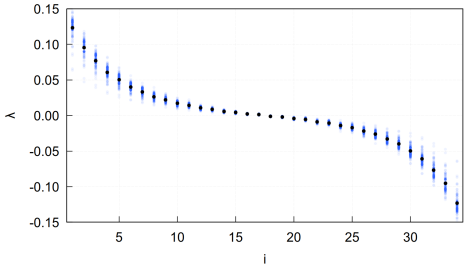

(c) $\Delta z = 0.05, \Gamma_{\max} = 0.0256$ $(R = 0.975)$.

Figure 5.15.: The Lyapunov's exponents for 100 trajectories (blue dots) from the z-focused ensemble and each exponent's average (black dot). Chosen parameters are $N = 17$, $\Delta t = 10^{-3}$, $\tau = 500$, $\delta_0 = 10^{-4}$ and $J_{\max} = 1$. More Lyapunov spectra are provided in appendix A.1b-A.1c.

AVERAGING PROCEDURES FOR THE MAXIMAL LYAPUNOV'S EXPONENT

We introduce one additional heuristic concerning the averaging procedure when calculating the average Lyapunov's exponent for several trajectories in a given ensemble. There are two types of averaging we apply. The first method is to take the trivial arithmetic average $\langle\lambda\rangle_{\text{arithmetic}}$ of all the individual maximum Lyapunov's exponents of each trajectory. The second is to average all the traversed distances of all the individual trajectories in the direction of the maximum Lyapunov's exponent, and use that average distance to calculate the Lyapunov's exponent as

$$\langle\lambda\rangle_{\text{dist}} = \lim_{t\to\infty} \frac{1}{t} \log\big(\langle \text{dist}(t)\rangle\big).$$

Because the logarithm is concave, Jensen's inequality implies $\langle\lambda\rangle_{\text{arithmetic}} \leq \langle\lambda\rangle_{\text{dist}}$. If $\langle\lambda\rangle_{\text{arithmetic}} \approx \langle\lambda\rangle_{\text{dist}}$, it means that different trajectories have similar dynamics. If the two values differ significantly, that indicates that some trajectories in the ensemble are much more unstable than others and strongly influence the average distance [Tex20].

DEPENDENCE OF λ_1 ON THE COUPLING RATIO R

We expect the appearance of integrable or chaotic dynamics to depend on several factors, including the overall strength of the spin-spin coupling $J_{\max}$, the strength of the transverse magnetic field $\Gamma_{\max}$, the specific realization of disorder, and the region of phase space in which the trajectory is initialized. We investigate this dependency by fixing a specific ensemble and, for one or more realizations

of disorder, investigate how the maximal Lyapunov's exponent λ_1 and the Kolmogorov–Sinai entropy H_{KS} depend on the coupling ratio $R = J_{max}/(J_{max} + \Gamma_{max})$.

In figure 5.16 we show the dependence of λ_1 on R for trajectories initialized in the uniform ensemble. In the limits $\Gamma_{max} \gg J_{max}$ and $\Gamma_{max} \ll J_{max}$ the system exhibits expected integrable dynamics, as shown by the vanishing of λ_1. For values of $0 < R < 0.04$, figures 5.16a and 5.16c show a small integrable plateau in which λ_1 remains close to zero, indicating that the transverse magnetic field is still sufficiently strong to suppress chaotic behavior. In contrast, for the realization of disorder shown in figure 5.16d, this plateau is significantly smaller, indicating a weaker effective magnetic-field dominance for that particular disorder configuration. Across all realizations considered, the maximal Lyapunov's exponent attains its largest value near $\Gamma_{max} \approx J_{max}/3$ (corresponding to $R \approx 0.75$).

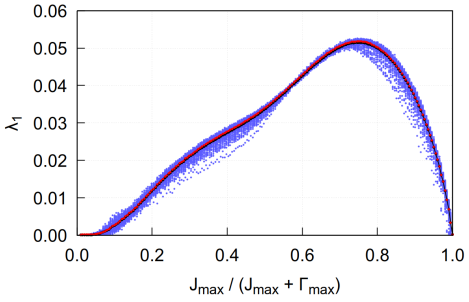

(a) Realization of disorder #1, uniform.

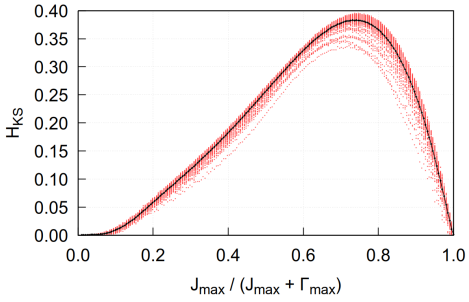

(b) Realization of disorder #1, uniform.

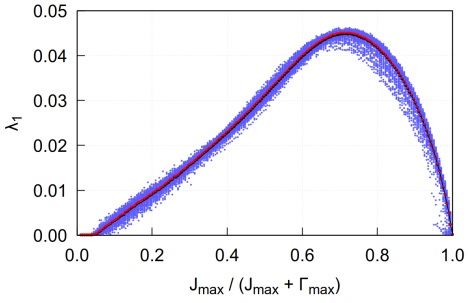

(c) Realization of disorder #2, uniform.

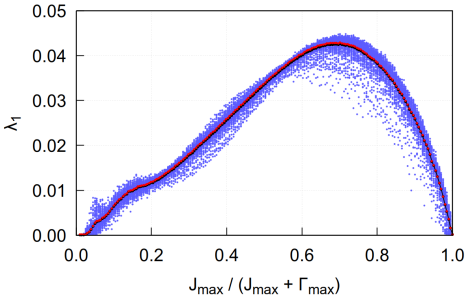

(d) Realization of disorder #3, uniform.

Figure 5.16.: The maximum Lyapunov's exponent λ_1, Kolmogorov-Sinai entropy H_{KS}, $\langle\lambda_1\rangle_{\text{arithmetic}}$ (black dot) and $\langle\lambda_1\rangle_{\text{dist}}$ (red dot) for 200 ratios of $J_{max}/(J_{max} + \Gamma_{max})$. For each sampled ratio, 100 runs were executed. Each run was chosen from the uniform ensemble. Chosen parameters are $N = 17$, $T = 3 \cdot 10^4$, $\Delta t = 10^{-2}$, $\tau = 50$, $\delta_0 = 10^{-4}$ and $J_{max} = 1$.

In figure 5.17 we show the dependence of λ_1 on R for trajectories initialized in the z-focused ensemble with $\Delta z = 0.05$. For $0 < R < 0.018$, figures 5.17a and 5.17c, in comparison to the uniform ensemble, show a larger integrable plateau in which λ_1 remains close to zero. This indicates that, within the z-focused ensemble, comparatively small values of the global magnetic field strength Γ_{max} are sufficient to suppress chaotic dynamics, in contrast to the behavior observed for the uniform ensemble. At the same time, for $0.05 < R < 0.6$ the curves display a clear

dependence on the specific realization of disorder. In figures 5.17a, 5.17c and 5.17d we observe several peaks and valleys where the R-dependence of λ_1 differs substantially between realizations, signaling a significant sensitivity to quenched disorder in this ensemble. Nevertheless, across all realizations considered, the value of R at which the maximal Lyapunov's exponent attains its largest value is consistent, occurring near $R \approx 0.8$.

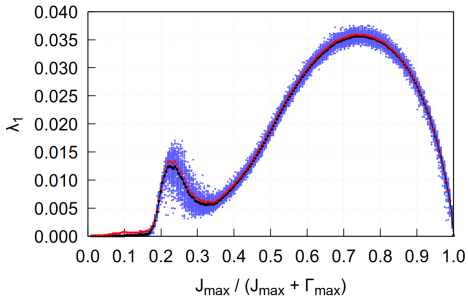

(a) Realization of disorder #1, $\Delta z = 0.05$.

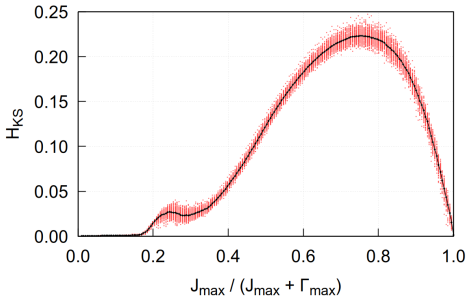

(b) Realization of disorder #1, $\Delta z = 0.05$.

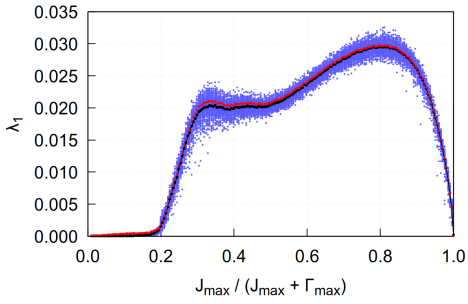

(c) Realization of disorder #2, $\Delta z = 0.05$.

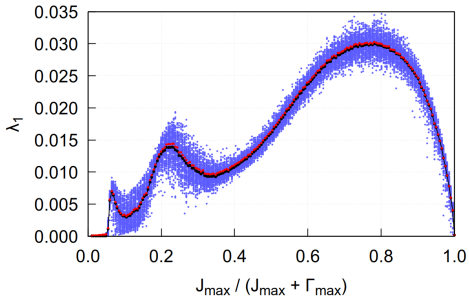

(d) Realization of disorder #3, $\Delta z = 0.05$.

Figure 5.17.: The maximum Lyapunov's exponent λ_1, Kolmogorov-Sinai entropy H_{KS}, $\langle\lambda_1\rangle_{\text{arithmetic}}$ (black dot) and $\langle\lambda_1\rangle_{\text{dist}}$ (red dot) for 200 ratios of $J_{\max}/(J_{\max}+\Gamma_{\max})$. For each sampled ratio, 100 runs were executed. Each run was chosen from the z-focused ensemble for $\Delta z = 0.05$. Chosen parameters are $N = 17$, $T = 3 \cdot 10^4$, $\Delta t = 10^{-2}$, $\tau = 50$, $\delta_0 = 10^{-4}$ and $J_{\max} = 1$.

By concentrating the z-focused ensemble more closely around the z-axis ($\Delta z = 0.01$), we observe in figure 5.18a that, in the interval $0.25 < R < 0.35$, the dynamics vary greatly per trajectory. Some trajectories remain nearly integrable with $\lambda_1 \approx 0$, while others exhibit clearly positive Lyapunov's exponents indicative of chaotic behavior. In contrast, when the ensemble is placed farther away from the z-axis (figure 5.18c) the near-integrable trajectories disappear and the ensemble consists primarily out of trajectories with chaotic dynamics.

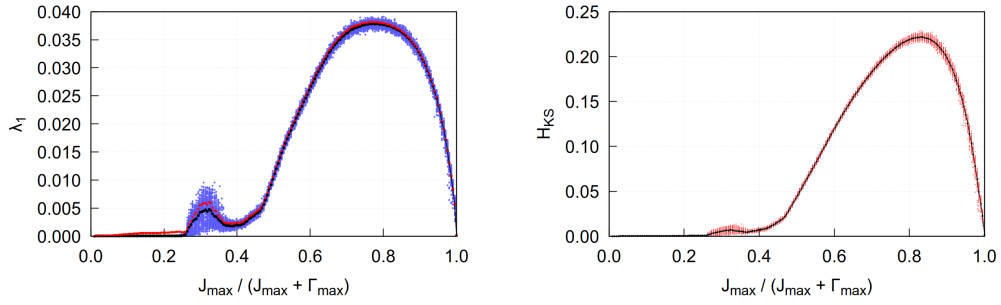

(a) $\Delta z = 0.01$.

(b) $\Delta z = 0.01$.

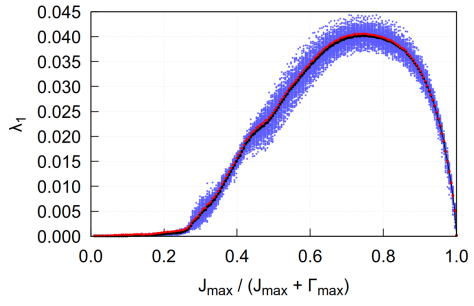

(c) $\Delta z = 0.10$.

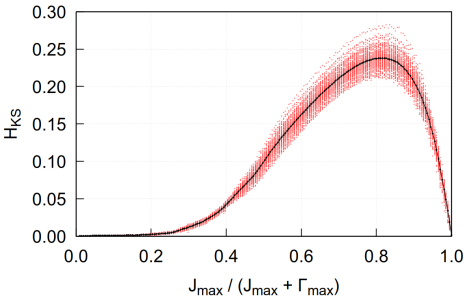

(d) $\Delta z = 0.10$.

Figure 5.18.: The maximum Lyapunov's exponent λ_1, Kolmogorov-Sinai entropy H_{KS}, $\langle\lambda_1\rangle_{\text{arithmetic}}$ (black dot) and $\langle\lambda_1\rangle_{\text{dist}}$ (red dot) for 200 ratios of $J_{\max}/(J_{\max}+\Gamma_{\max})$. For each sampled ratio, 100 runs were executed. Each run was chosen from the z-focused ensemble. The realization of disorder for the chosen system is #1. Chosen parameters are $N = 17$, $T = 3 \cdot 10^4$, $\Delta t = 10^{-2}$, $\tau = 50$, $\delta_0 = 10^{-4}$ and $J_{\max} = 1$.

In figure 5.19 we show the dependence of the maximal Lyapunov's exponent λ_1 on R for trajectories initialized in the x-focused ensemble, for several values of Δx. For $\Delta x = 0.01$ and $\Delta x = 0.10$ (see figures 5.19c and 5.19d), we observe a narrow integrable plateau in the interval $0.95 < R < 1$, where λ_1 remains close to zero. This indicates that a sufficiently strong spin-spin coupling can enforce integrable dynamics. Moreover, we also find a thin integrable plateau for $0 < R < 0.05$, showing that in this x-focused ensemble a sufficiently strong transverse magnetic field can also enforce integrable dynamics. In contrast, for the uniform and z-focused ensemble we were unable to find a sufficiently strong spin-spin coupling $J_{\max}$ to enforce integrable dynamics when $\Gamma_{\max} \neq 0$.

In figure 5.19 we also see that, for each value of Δx, there exists a global parameter range, when $J_{\max} \gg \Gamma_{\max}$, for which λ_1 changes rapidly under small variations of R. This sharp crossover suggests that there exists a threshold value of R in this range at which the qualitative nature of the dynamics changes for almost all trajectories in the ensemble and the chosen realization of disorder. Furthermore, in the x-focused ensemble the value of R at which the maximal Lyapunov's exponent attains its largest value is slightly reduced compared to the uniform and z-focused ensembles, occurring at $R \approx 0.65$–0.7.

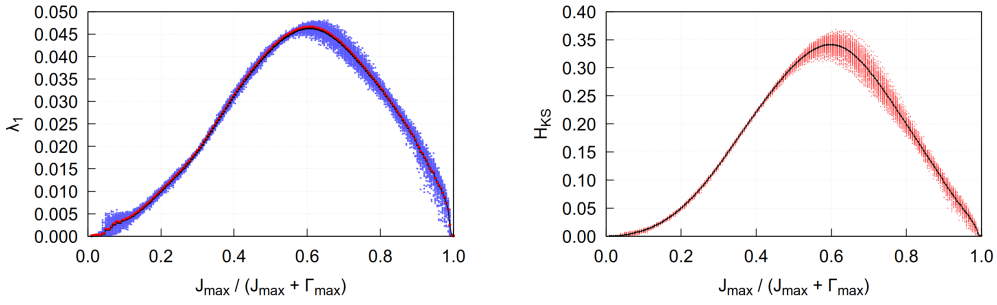

(a) $\Delta x = 0.05$.

(b) $\Delta x = 0.05$.

(c) $\Delta x = 0.01$.

(d) $\Delta x = 0.10$.

Figure 5.19.: The maximum Lyapunov's exponent λ_1, Kolmogorov-Sinai entropy H_{KS}, $\langle\lambda_1\rangle_{\text{arithmetic}}$ (black dot) and $\langle\lambda_1\rangle_{\text{dist}}$ (red dot) for 200 ratios of $J_{\text{max}}/(J_{\text{max}}+\Gamma_{\text{max}})$. For each sampled ratio, 100 runs were executed. Each run was chosen from the x-focused ensemble. The realization of disorder for the chosen system is #1. Chosen parameters are $N = 17$, $T = 3 \cdot 10^4$, $\Delta t = 10^{-2}$, $\tau = 50$, $\delta_0 = 10^{-4}$ and $J_{\text{max}} = 1$.

HAMILTONIAN RESCALING

One challenge in comparing results from different choices of global parameters $(J_{\text{max}}, \Gamma_{\text{max}})$ is that both the typical values and the distribution of the Hamiltonian H changes. The same absolute energy can then correspond to different parts of the spectrum for different parameter sets. For example, a given value of H might lie near the center of the energy distribution for one choice of $(J_{\text{max}}, \Gamma_{\text{max}})$, but in the low- or high-energy tails for another, where the density of states and accessible phase-space volume are different. As a result, Lyapunov's exponents evaluated at a fixed value of H are not directly comparable across different parameter sets.

In the quantum case for the energy-level spacing statistics, when unfolding the spectrum, energy spacings are rescaled by the mean level spacing ΔE, so that $(E_1 - E_2)/\Delta E$ has unit mean spacing. In the classical case, we can still similarly remove the overall scale of H by normalizing with the ensemble standard deviation $\sigma(H)$. Concretely, we work with the ratio $H/\sigma(H)$, where $\sigma(H)$ is computed for a chosen ensemble of spin configurations at fixed $(J_{\text{max}}, \Gamma_{\text{max}})$. This provides a natural energy unit determined by the width of the energy distribution. Comparing Lyapunov's exponents at fixed $H/\sigma(H)$ then means comparing trajectories at similar relative positions within their respective energy distributions, rather than

at arbitrary absolute values of H. By exploiting the symmetry and independent probability distribution of the coefficients J_{ij}, Γ_i and spin S_i we can calculate $\sigma(H)$ for our three different ensembles. We obtain for the uniform ensemble:

$$\sigma(H) = \sqrt{\frac{N-1}{54} J_{\max}^2 + \frac{N}{9}\Gamma_{\max}^2},$$

and for the z-focused ensemble

$$\sigma(H) = \sqrt{\frac{N-1}{6}\left(\Delta z - \frac{\Delta z}{2}\right)^2 J_{\max}^2 + \frac{N}{12}(1-\Delta z)^2\Gamma_{\max}^2},$$

5

and for the x-focused ensemble

$$\sigma(H) = \sqrt{\frac{N-1}{6}(1-\Delta x)^4 J_{\max}^2 + \frac{N}{6}(2\Delta x - \Delta x^2)\Gamma_{\max}^2}.$$

Using these expressions for $\sigma(H)$, we observe in figures 5.20-5.22 the relationship beween the maximum Lyapunov's exponent λ_1 and the rescaled energy $H/\sigma(H)$ for several ensembles. These figures illustrate how chaotic and integrable dynamics can arise for certain energy ranges in a given ensemble.

In figure 5.20 we compare the maximum Lyapunov's exponent λ_1 to the rescaled energy $H/\sigma(H)$ for several values of R in the uniform and z-focused ensemble. For the z-focused ensembles, we observe that the dense clusters of points in figures 5.20b, 5.20c and 5.20d correspond to the peaks and valleys seen in figures 5.17a, 5.17c and 5.17d. This indicates that these pronounced features in λ_1 are mainly associated with trajectories with a relatively large rescaled energy, rather than with typical rescaled energies near $H/\sigma(H) \approx 0$.

More specifically, figure 5.21c shows that trajectories in the z-focused ensemble, with $\Delta z = 0.01$, have large values of $H/\sigma(H)$ up to relatively large values of R when compared to the z-focused ensemble with $\Delta z = 0.05$. In contrast, figure 5.21d shows that trajectories in the z-focused ensemble, with $\Delta z = 0.10$, have smaller values of $H/\sigma(H)$ already at relatively lower values of R than for the z-focused ensemble with $\Delta z = 0.05$.

In figures 5.20e, 5.21c and 5.21d we also see that, as the spin-spin coupling becomes more dominant (larger R), the sampled values of $H/\sigma(H)$ move closer to zero. For the z-focused ensemble this suggests that stronger spin-spin couplings results in smaller energy values, whereas for small values of R the z-focused ensemble more frequently samples larger energies. Finally, for the uniform ensemble we observe in figure 5.20a that varying R has only a relatively small effect on the distribution of $H/\sigma(H)$, so the overall rescaled energy distribution is relatively insensitive to changes in R.

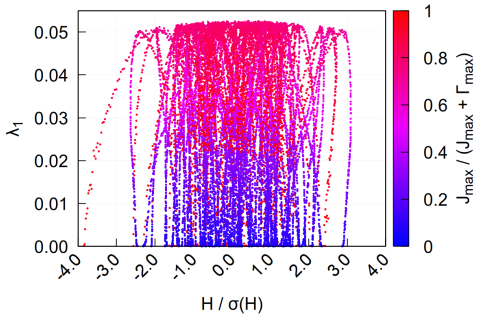

(a) Realization of disorder #1, uniform.

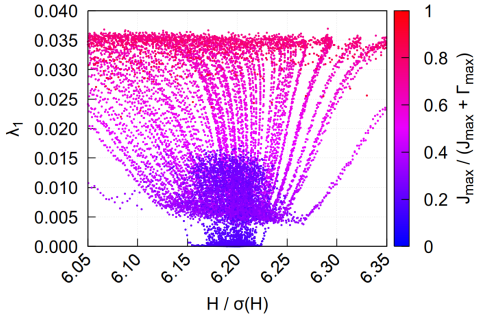

(b) Realization of disorder #1, $\Delta z = 0.05$.

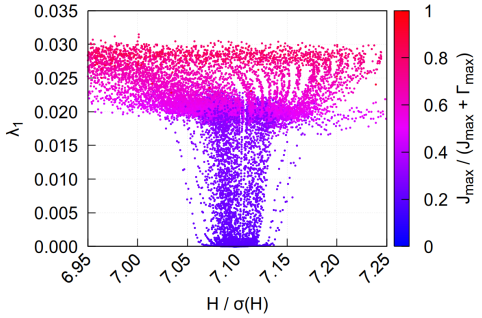

(c) Realization of disorder #2, $\Delta z = 0.05$.

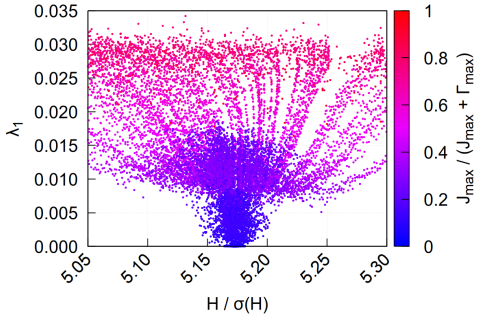

(d) Realization of disorder #3, $\Delta z = 0.05$.

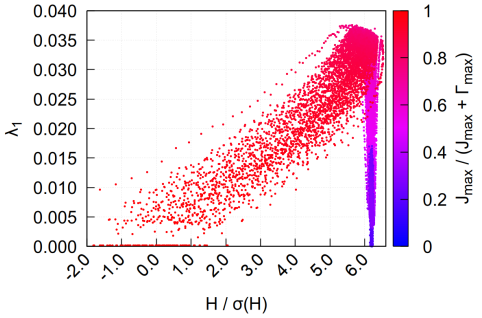

(e) Realization of disorder #1, $\Delta z = 0.05$. Zoomed out view of figure 5.20b.

Figure 5.20.: The maximum Lyapunov's exponent for various values of $H/\sigma(H)$. For each of the 200 sampled ratios $J_{max}/(J_{max} + \Gamma_{max})$ and ensemble choice, 100 runs were executed. Each run was chosen from the uniform or z-focused ensemble. Chosen parameters are $N = 17$, $T = 3 \cdot 10^4$, $\Delta t = 10^{-2}$, $\tau = 50$, $\delta_0 = 10^{-4}$ and $J_{max} = 1$. More uniform ensemble distributions are provided in appendix A.5.

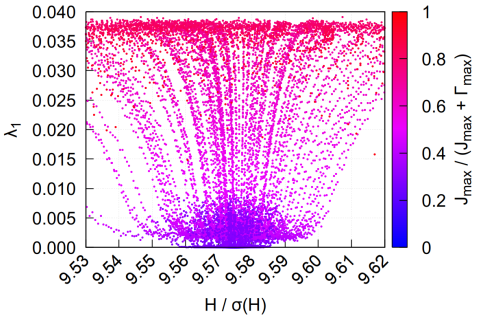

(a) $\Delta z = 0.01$.

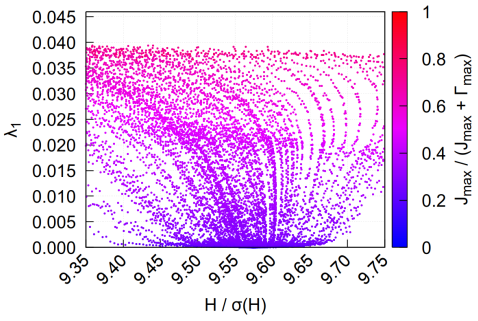

(b) $\Delta z = 0.10$.

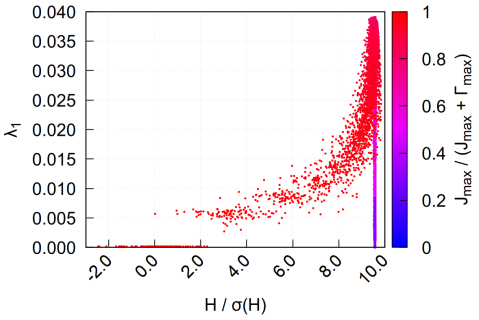

(c) $\Delta z = 0.01$. Zoomed out view of figure 5.21a.

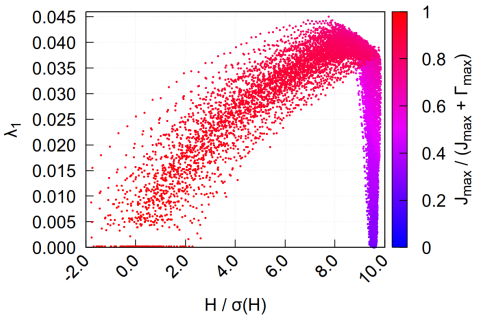

(d) $\Delta z = 0.10$. Zoomed out view of figure 5.21b.

Figure 5.21.: The maximum Lyapunov's exponent for various values of $H/\sigma(H)$. For each of the 200 sampled ratios $J_{\max}/(J_{\max} + \Gamma_{\max})$, 100 runs were executed. Each run was chosen from the z-focused ensemble. The realization of disorder for the chosen system is #1. Chosen parameters are $N = 17$, $T = 3 \cdot 10^4$, $\Delta t = 10^{-2}$, $\tau = 50$, $\delta_0 = 10^{-4}$ and $J_{\max} = 1$.

In figure 5.22 we compare the maximum Lyapunov's exponent λ_1 to the rescaled energy $H/\sigma(H)$ for several values of R in the x-focused ensemble. In figures 5.22a and 5.22c we observe that the clusters of red points at relatively small values of $H/\sigma(H)$ correspond to the integrable plateaus seen in figures 5.19c and 5.19d near the spin-spin coupling dominated regime.

Moreover, as the transverse magnetic field becomes more dominant, the sampled values of $H/\sigma(H)$ in the x-focused ensemble shift slightly toward smaller values of $H/\sigma(H)$, but this shift is noticeably weaker than in the z-focused case shown in figure 5.20e.

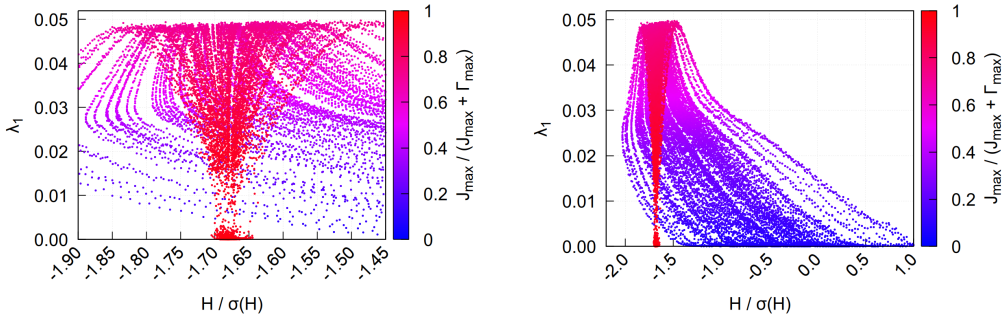

(a) $\Delta x = 0.01$.

(b) $\Delta x = 0.01$. Zoomed out view.

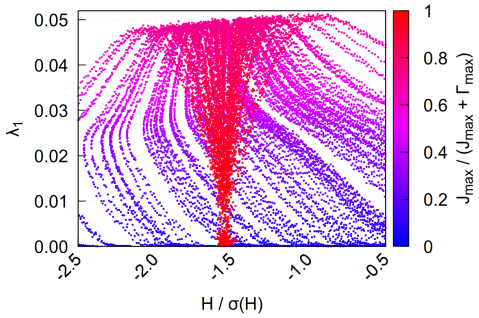

(c) $\Delta x = 0.10$.

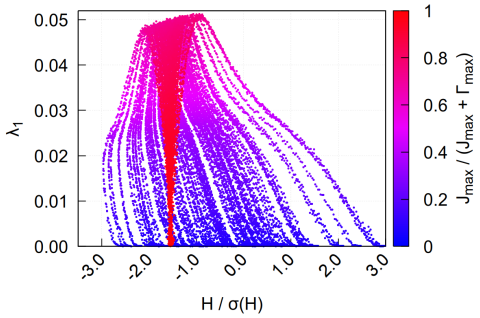

(d) $\Delta x = 0.10$. Zoomed out view.

Figure 5.22.: The maximum Lyapunov's exponent for various values of $H/\sigma(H)$. For each of the 200 sampled ratios $J_{max}/(J_{max} + \Gamma_{max})$, 100 runs were executed. Each run was chosen from the x-focused ensemble. The realization of disorder for the chosen system is #1. Chosen parameters are $N = 17$, $T = 3 \cdot 10^4$, $\Delta t = 10^{-2}$, $\tau = 50$, $\delta_0 = 10^{-4}$ and $J_{max} = 1$. More x-focused ensemble distributions are provided in appendix A.5.

These figures show that measuring energy in units of its ensemble standard deviation, $H/\sigma(H)$, is a method to compare dynamics across different system parameter choices and ensembles. In the z-focused ensembles, the strong peaks and dips in the largest Lyapunov's exponent are mainly found for trajectories at relatively large rescaled energies, while trajectories near $H/\sigma(H) \approx 0$ have more integrable dynamics. As the spin-spin coupling becomes stronger, the sampled rescaled energies in the z-focused case shift toward zero, this shift is slower for initial spin configurations that are more closely aligned with the z-axis. In the uniform ensemble, the rescaled energy distribution hardly changes with the coupling ratio R, and in the x-focused ensembles the integrable plateaus correspond to clusters at relatively small rescaled energies, with only a modest shift as the transverse magnetic field increases. Overall, depending on the choice of ensemble, the figures show that whether the dynamics are chaotic or integrable can be associated with certain energy ranges in the rescaled energy distribution.

5.4. Lyapunov spectra for multiple realized disorders

Having examined the dynamics for varying global parameters (J_{max}, Γ_{max}) and a few realizations of disorder, the question remains to what extent different realizations

of disorder behave similarly or differently in general. Our approach is to fix a phase space ensemble, choose several values of R, and compute the maximal Lyapunov's exponent λ_1 for multiple realizations of disorder at several fixed values of R.

In figure 5.23 we show the results for the uniform ensemble. The sampled energy values span a broad interval and form an approximately symmetric distribution around $H = 0$, consistent with the expectation for spins uniformly sampled on the unit sphere. Across different realizations of disorder, the observed dynamics (integrable or chaotic) are similar for different values of H, although the absolute values of the exponents vary per realization, the general form is largely preserved from one realization to another. In particular, we see in figure 5.23d, for $R = 0.75$, that the largest values of λ_1 occur predominantly near $H \approx 0$. For $R = 0.4$ (figure 5.23c), the largest values of λ_1 tend to occur in either the maximum or minimum sampled value of the Hamiltonian H, depending on the specific realization of disorder. Thus, in this regime the energy where chaos is strongest is qualitatively more sensitive to the particular realization of disorder. Finally, for smaller values of R, such as in figures 5.23a and 5.23b, we no longer observe a clear dependence of λ_1 on H. Instead, different realizations of disorder mainly act to shift the overall value of λ_1 up or down, with only a noisy dependency on the Hamiltonian.

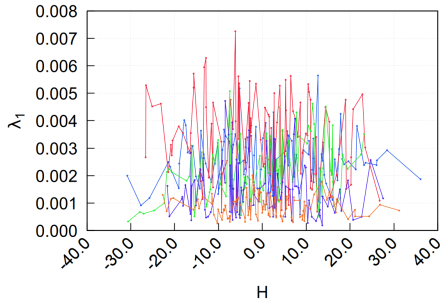

(a) $\Gamma_{\max} = 9$ ($R = 0.1$).

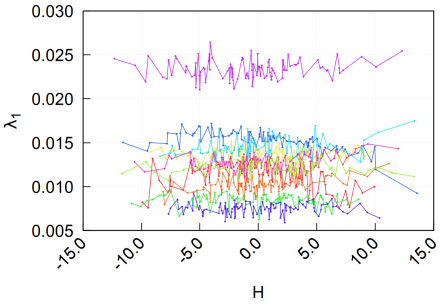

(b) $\Gamma_{\max} = 3.28$ ($R = 0.2335$).

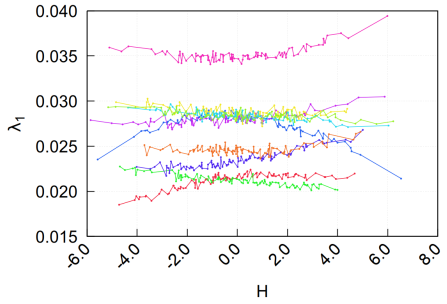

(c) $\Gamma_{\max} = 1.5$ ($R = 0.4$).

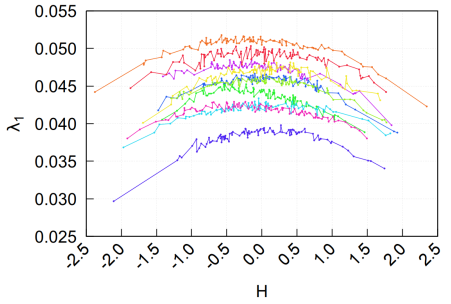

(d) $\Gamma_{\max} = 0.33$ ($R = 0.75$).

Figure 5.23.: The maximum Lyapunov's exponent for various values of H. For each of the 10 shown realizations of disorder, shown in different colors, 100 runs were executed. Each run was chosen from the uniform ensemble. Chosen parameters are $N = 17$, $T = 3 \cdot 10^4$, $\Delta t = 10^{-2}$, $\tau = 50$, $\delta_0 = 10^{-4}$, $J_{\max} = 1$.

In figure 5.24 we show the results for the z-focused ensemble. For this ensemble the sampled energies are mostly positive and, for each realization of disorder,

occupy a comparatively narrow interval, as expected from configurations whose spins are initially concentrated near the direction of the transverse magnetic field. For values of $R \geq 0.33$, see figures 5.24c, 5.24d and 5.24e, the observed maximal Lyapunov's exponents are all significantly positive and form a single cluster for each realization of disorder, with similar vertical height in λ_1. The clusters are slightly diagonal, which we can interpret by noticing that within the z-focused ensemble, systems with larger values of H correspond to spin configurations more closely aligned with the transverse magnetic field, resulting in a larger H_B term, whereas configurations with smaller values H at the same R have a, relative to H_B, larger contribution from the spin-spin term H_A. Because chaotic dynamics are expected to be stronger when both spin-spin interactions and magnetic field terms contribute substantially, a slight diagonal shape of the clusters is expected.

For smaller values of R, starting around $R \simeq 0.2335$ (figure 5.24b), a qualitatively different pattern emerges. For each realization of disorder, the points separate into two distinct types: one vertically extended cluster with clearly positive λ_1, characteristic of chaotic dynamics, and a small, point cloud with $\lambda_1 \approx 0$, indicative of nearly integrable motion. Within the set of realizations examined, each realization appears to fall primarily into one of these two types, and we do not observe cases that display both types. This suggests the existence, for the z-focused ensemble at $\Delta z = 0.05$, of a certain threshold value for the coupling ratio $0.2335 \leq R \leq 0.33$ below which the observed type of dynamics of all trajectories in the ensemble is dependent on the specific realization of quenched disorder.

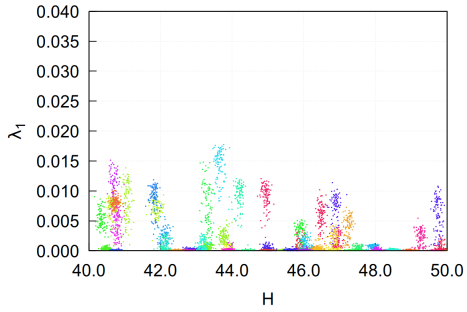

(a) $\Gamma_{max} = 5.66$ ($R = 0.15$).

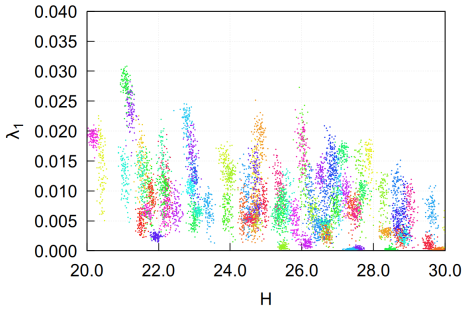

(b) $\Gamma_{max} = 3.28$ ($R = 0.2335$).

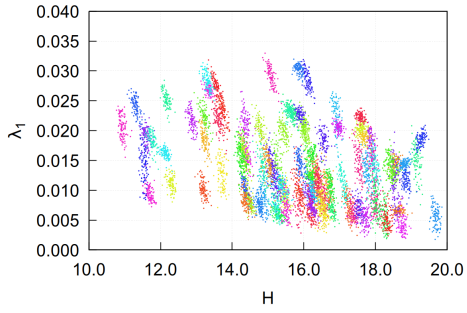

(c) $\Gamma_{max} = 2.03$ ($R = 0.33$).

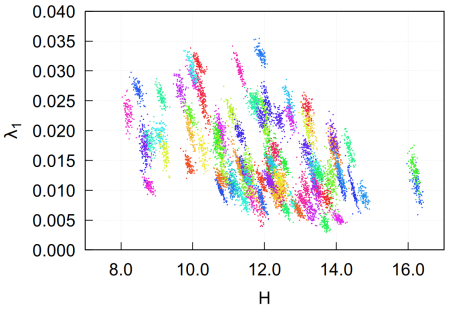

(d) $\Gamma_{max} = 1.5$ ($R = 0.4$).

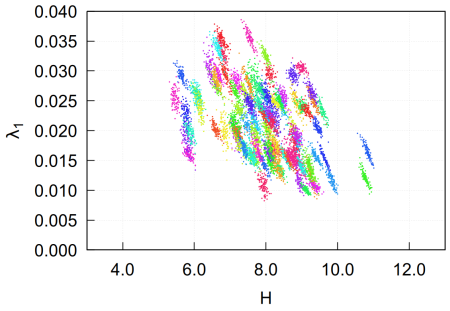

(e) $\Gamma_{max} = 1$ ($R = 0.5$).

Figure 5.24.: The maximum Lyapunov's exponent for various values of H . For each of the 100 shown realizations of disorder, shown in different colors, 100 runs were executed. Each run was chosen from the z-focused ensemble with $\Delta z = 0.05$. Chosen parameters are $N = 17$, $T = 3 \cdot 10^4$, $\Delta t = 10^{-2}$, $\tau = 50$, $\delta_0 = 10^{-4}$ and $J_{max} = 1$.

In figure 5.25 we show the results for the x-focused ensemble with $\Delta x = 0.01$. For this ensemble the sampled energies form an approximately symmetric distribution and, for each realization of disorder, occupy a narrow interval. This is consistent with the fact that the dominant contribution to the energy comes from the spin-spin interaction term H_A, while the x-component of each spin is initially fixed. Since the z-component can vary only slightly for $\Delta x = 0.01$, and $\Gamma_{max} \ll 1$ for $R > 0.925$, the contribution of the field term H_B remains small, which explains the narrow spread

in H per realization.

As in the z-focused case, we observe two types of realizations of disorder: some realizations exhibit predominantly chaotic behavior with clearly positive λ_1, while others display point clouds with $\lambda_1 \approx 0$ indicative of integrable dynamics. In the x-focused ensemble, however, there also exist realizations that exhibit characteristics of both types. Overall, as Γ_{max} increases (corresponding to decreasing R), the typical magnitude of λ_1 grows and the fraction of integrable point clouds decreases. For $R = 0.95$ and $R = 0.925$, among the realizations that exhibit chaotic behavior, those with energy distribution $H \approx 0$ tend to have slightly larger maximal Lyapunov's exponents.

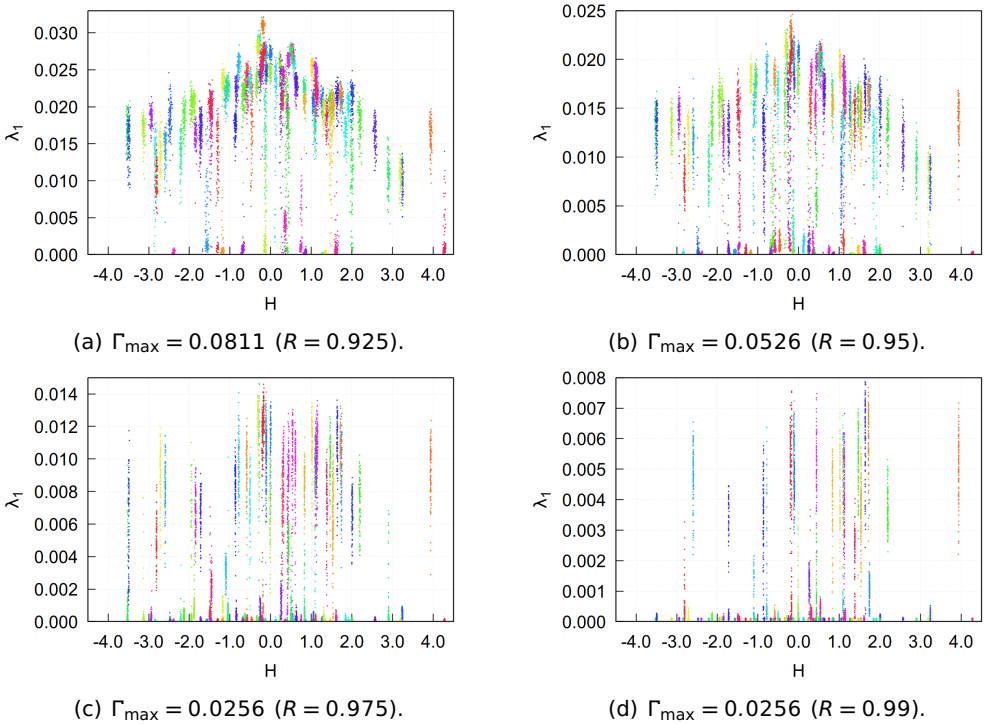

(a) $\Gamma_{max} = 0.0811$ ($R = 0.925$).

(b) $\Gamma_{max} = 0.0526$ ($R = 0.95$).

(c) $\Gamma_{max} = 0.0256$ ($R = 0.975$).

(d) $\Gamma_{max} = 0.0256$ ($R = 0.99$).

Figure 5.25.: The maximum Lyapunov's exponent for various values of H . For each of the 100 shown realizations of disorder, shown in different colors, 100 runs were executed. Each run was chosen from the x-focused ensemble with $\Delta x = 0.01$. Chosen parameters are $N = 17$, $T = 3 \cdot 10^4$, $\Delta t = 10^{-2}$, $\tau = 50$, $\delta_0 = 10^{-4}$ and $J_{max} = 1$.

6

DISCUSSION

We first note that the numerical results in section (5.1) confirm the correct implementation of the second-order Suzuki–Trotter integrator and the Lyapunov's exponents calculation scheme. The phase-space volume and the Hamiltonian fluctuate around their expected constant mean values, without exhibiting any systematic drift. In addition, the symplectic form ω is preserved over the entire integration time, as reflected in two key properties of the Lyapunov spectrum. First, the sum of all Lyapunov's exponents converges to zero within numerical accuracy, as expected for a integration scheme that preserves phase space volume. Second, the finite-time Lyapunov's exponents converge to symmetric pairs, which indicates that the symplectic structure is preserved by the numerical scheme.

Furthermore, we have successfully computed full Lyapunov spectra for systems with $N = 17$ spins (figures 5.6, 5.7a, 5.8a and 5.9c) and also for a substantially larger system with $N = 100$ spins (figure 5.10a). In both cases the spectra satisfy the expected constraints.

DEPENDENCE ON COUPLING PARAMETERS

Our results confirm that the classical spin glass shard model (5.1) exhibits both integrable and chaotic dynamics, depending on the relative strength of the spin-spin coupling J_{max} and the transverse magnetic field Γ_{max}.

A first observation is that, as expected, for all ensembles studied (uniform, z-focused and x-focused), the dynamics indeed become integrable in the limits $R \approx 0$ and $R \approx 1$, see figures 5.16, 5.17, 5.18 and 5.19. In these limits the maximal Lyapunov's exponent λ_1 approaches zero and the motion of the trajectories are well described by a precession dominated either by the magnetic field ($R \to 0$) or by the spin-spin coupling ($R \to 1$).

For the z-focused ensemble with $\Delta z = 0.05$, figure 5.17 shows plateaus of integrability at small values of $R < 0.2$, which are more pronounced than in the uniform ensemble. This indicates that aligning spins closer to the z-axis makes it easier for the transverse magnetic field to enforce integrable dynamics. At the same time, the dependence of λ_1 on R is more irregular in the z-focused ensemble, especially when $R < 0.5$. In particular, in figure 5.17d we observe that several pronounced peaks and valleys are present for one realization of disorder that produced a relatively weak interaction with the transverse magnetic field.

The x-focused ensemble exhibits its own characteristic features. For several values of Δx we again observe integrable behaviour as $R \to 0$ and $R \to 1$, but the location of the maximum of λ_1 is shifted slightly to $R \approx 0.65 - 0.70$, see figure 5.19. This suggests that trajectories initially aligned closer to the x-axis become maximally chaotic at relatively stronger transverse magnetic fields than those in the uniform or z-focused ensembles. Moreover, while we might generally expect that concentrating the focused ensembles closer to the coordinate axes,

by choosing a smaller Δx or Δz, makes it more likely to obtain larger plateaus of integrability around $R \approx 0$ or $R \approx 1$, our results show that this expectation is not always valid. In particular, for the realization of disorder shown in figure 5.17, the plateau of integrability observed for $\Delta x = 0.05$ (figure 5.19a) is in fact smaller than the corresponding plateau of integrability for $\Delta x = 0.10$ (figure 5.19d), indicating that the emergence and size of integrable regions depend in a nontrivial way on the ensemble choice.

One additional observation is that for all ensembles the strongest chaotic dynamics are consistently found near $\Gamma_{\max} \approx 0.33 J_{\max}$. For this choice of global parameters, the maximal Lyapunov's exponent λ_1 attains its largest value, independent of the specific realization of disorder, see figures 5.16, 5.17 and 5.19. The location of the strongest chaotic dynamics near $R \approx 0.75$ can be possibly explained for the uniform ensemble by requiring the standard deviation of H_A and H_B to be equal. This would imply that the spin-spin coupling term H_A and the transverse magnetic field term H_B have similar energy scales and neither term dominates the dynamics. Concretely, using

$$\sigma(H_A) = \sqrt{\frac{N-1}{54}} J_{\max}, \qquad \sigma(H_B) = \sqrt{\frac{N}{9}} \Gamma_{\max},$$

and equating these standard deviations, we find that

$$\Gamma_{\max} = J_{\max} \sqrt{\frac{N-1}{6N}}.$$

For $N = 17$ this yields

$$\Gamma_{\max} \approx 0.396 J_{\max}, \quad R \approx 0.716$$

which is somewhat larger than the value $\Gamma_{\max} \approx 0.33 J_{\max}$ corresponding to $R \approx 0.75$. Nevertheless, this comparison of standard deviations provides qualitative support for the idea that the strongest chaotic dynamics are present when H_A and H_B have standard deviations of comparable size, which is broadly consistent with the observed range of R.

DEPENDENCE ON REALIZATIONS OF DISORDER

Another goal of this work was to understand how sensitive the classical dynamics are to the realizations of quenched disorder. Figure 5.23 shows that, in the uniform ensemble for a fixed R, all realizations of disorder exhibit the same type of dynamics and are either all chaotic (with $\lambda_1 > 0$) or all integrable (with $\lambda_1 \approx 0$). Moreover, for different disorder realizations the dependence of λ_1 on the Hamiltonian H does not significantly change. Therefore, for the uniform ensemble, we can generally expect that the type of dynamics observed for one realization of disorder is approximately representative of all realizations of disorder. For trajectories in the uniform ensemble when $\Gamma_{\max} \approx J_{\max}/3$, we additionally observe in figure 5.23d that the largest maximum Lyapunov's exponents occur when $H \approx 0$. Similarly, for the x-focused ensemble at relatively large values of $R = 0.95$ we observe in figure 5.25 that, for all disorder realizations displaying chaotic dynamics, the maximum of λ_1 again occurs when $H \approx 0$.

In contrast, for the x-focused and z-focused ensembles there is a significant dependence of the maximum Lyapunov's exponent λ_1 on the realization of disorder. Figures 5.24 and 5.25 show that, for different realizations of disorder, the dynamics can drastically vary. For some realized disorders all the trajectories are integrable, while for other realized disorders the trajectories all have chaotic dynamics.

However, while the dynamics can greatly vary for each different realization of disorder, we do observe that all realizations of disorder generally are more chaotic for intermediate values of R, and integrable when $R \approx 0$ or $R \approx 1$.

In general, the main phenomenon we observe are the following:

- the existence of integrable dynamics at $R \approx 0$ and $R \approx 1$ and the location of the strongest chaos near $R \approx 0.65 - 0.80$ are robust across all studied ensembles.
- trajectories in the uniform ensemble exhibits the most robust behaviour with respect to realizations of disorder, with all trajectories sharing the same type of dynamics at fixed values of R.
- the dynamics of the trajectories in the x-focused and z-focused ensembles are more sensitive to the specific realization of disorder, especially at intermediate values of R, depending on the specific realization of disorder.
- the dependence of λ_1 on R is especially irregular in the z-focused ensemble for $R < 0.5$, see figure 5.19. This dependence greatly varies for different realizations of disorder.
- Plateaus of integrability generally appear in the x-focused ensemble (z-focused ensemble) for $\Delta x \ll 1$ ($\Delta z \ll 1$), becoming larger in size as Γ_{max} decreases (increases). However, there do exist exceptions to this rule, as observed in figures 5.19a and 5.19a.

ENERGY SCALES

To further characterize for which typical energies chaotic and integrable dynamics occur, we introduced a rescaling of the Hamiltonian H by the ensemble standard deviation $\sigma(H)$, and examined the dependence of the maximal Lyapunov's exponent λ_1 on this rescaled Hamiltonian for different ensembles. This rescaling is motivated by the normalization step in the spectrum unfolding procedure when constructing the quantum level-spacing statistics.

For the z-focused ensemble, figures 5.20-5.21 shows that, once Hamiltonians H are expressed in units of $\sigma(H)$, the largest Lyapunov's exponents tend to occur for relatively large values of H. As the spin-spin interaction becomes more dominant (larger R), the typical energies of the trajectories become smaller. Additionally, we observe that the irregular dependencies of λ_1 on R, observed in figures 5.17a, 5.17c and 5.17d, correspond with certain narrow ranges of energy in figures 5.20b-5.20d.

In contrast, for the uniform and x-focused ensembles (figures 5.20a and 5.22) the strongest chaotic dynamics are less systematically associated with large values in the ensemble's rescaled energy distribution. In these ensembles, trajectories with large λ_1 have relatively small energy values, compared to the z-focused ensemble, and the relation between energy and chaotic dynamics is less obvious. Taken together, these findings suggest that the locations in the energy values for which we observe integrable or chaotic dynamics are strongly dependent on the ensemble choice, being most distinct for the z-focused ensemble.

COMPARISON WITH QUANTUM RESULTS

The next step in our analysis is to compare our classical findings with the results of Georgeot and Shepelyansky [GS98], who studied the quantum analog of the spin glass model in a transverse magnetic field and characterized quantum chaos via

level-spacing statistics. In figure 3.4, they report for several number of spins a small interval

$$0 < \frac{J_{max}}{J_{max} + \Gamma_{max}} \leq 0.1$$

in which the level-spacing statistics are close to Poissonian, indicative of integrable dynamics. A similar plateau of integrability is observed in our classical simulations for both the uniform and z-focused ensembles, where $\lambda_1 \approx 0$ for sufficiently small values of R (figures 5.16 and 5.17). However, no such plateau appears in the x-focused ensemble, indicating that the strong effective spin-spin coupling experienced by trajectories initialized near the x-axis is sufficient to sustain chaotic dynamics even in the presence of relatively large values of Γ_{max}.

At the opposite end of the interval, for

$$0.9 \leq \frac{J_{max}}{J_{max} + \Gamma_{max}} \leq 1$$

Georgeot and Shepelyansky observe a rapid crossover of the level-spacing statistics back towards Poissonian behaviour as $J_{max}/(J_{max} + \Gamma_{max})$ increases, without a visible plateau of integrability. Our classical results in this regime show a similar trend: for the uniform and z-focused ensembles the maximal Lyapunov's exponent decreases sharply as $R \to 1$, but does not develop a broad integrable plateau where $\lambda_1 \approx 0$ (figures 5.16 and 5.17). In contrast, for the x-focused ensemble we do observe a narrow plateau of integrability near $R \approx 1$, indicating that in this ensemble the spin-spin interaction can enforce nearly integrable dynamics up to some non-zero threshold value of Γ_{max}.

There is, however, an important quantitative difference between the classical and quantum indicators of chaos. For the quantum system, the level-spacing statistics is closest to the GOE distribution for

$$0.3 \leq \frac{J_{max}}{J_{max} + \Gamma_{max}} \leq 0.4.$$

In our classical analysis the maximal Lyapunov's exponent attains its maximum at the significantly larger ratio $J_{max}/(J_{max} + \Gamma_{max}) \approx 0.75$. This suggests that the global parameters (J_{max}, Γ_{max}) for which we observe the largest Lyapunov's exponents in the classical system, does not coincide with the set of global parameters $(J'_{max}, \Gamma'_{max})$, for which we observe the strongest signature of chaos in the quantum analog, for which $\Gamma'_{max} \approx 4.5\Gamma_{max}$ (assuming we fix $J_{max} = J'_{max} = 1$).

We emphasize that this discrepancy does not necessarily indicate a fundamental mismatch between classical and quantum chaos, but can also be explained by highlighting that different diagnostics (Lyapunov's exponents versus level-spacing statistics), applied in different regimes (classical many-body versus quantum many-body), can quantitatively differ from each other.

7

CONCLUSION

In this thesis we have investigated how global system parameters and local realizations of quenched disorder influence the dynamics of a classical many-body spin system, and how classical and quantum signatures of chaos relate to each other. We examined the dynamics of the classical analog of the quantum spin glass shards model in a random transverse magnetic field studied by Georgeot and Shepelyansky [GS98]. We then constructed and analysed the dynamics of the classical analogue of this spin glass shards model by computing Lyapunov's exponents for trajectories in different regions of phase space. For this purpose, we described the classical many-body spin phase space as a symplectic manifold and made use of a second-order Suzuki-Trotter integrator to evolve the trajectories while preserving the symplectic structure needed to reliably calculate the Lyapunov's exponents. This allowed us to obtain accurate finite-time approximations of the Lyapunov spectrum via the standard procedure of repeated reorthogonalization of tangent vectors through applying the QR decomposition.

With these tools, we identified integrable and chaotic areas of phase space as functions of both the relative strength of the spin-spin coupling and the transverse magnetic field. We found that, for all regions considered, both the strong spin-spin coupling limit and the strong transverse magnetic field limit are nearly integrable, while the dynamics is most strongly chaotic within a consistent range of intermediate coupling–field ratios. For spin configurations uniformly distributed over phase space, we observed that different realizations of disorder do not significantly affect whether the dynamics is chaotic or integrable. In contrast, configurations with spins more concentrated near the x- or z-axis are more sensitive to the specific realization of disorder and can display either almost completely integrable or strongly chaotic dynamics for identical global system parameters. However, regardless of the region of phase space, for 17 spins, we find that the classical spin system generally exhibits chaotic dynamics for all trajectories when the spin-spin coupling is three times as strong as the transverse magnetic field. Comparing these classical results with the quantum energy level-spacing statistics of the corresponding quantum model reveals a qualitative agreement in the appearance of plateaus of integrability and chaotic windows. However, these findings also show that Lyapunov's exponents have a complex relation to energy level-spacing statistics. In response to global changes in the Hamiltonian, Lyapunov's exponents vary in a way that is correlated with, but not identical to this quantum signature of chaos.

There are several directions in which the present work can be extended:

Firstly, we can apply the same Lyapunov's exponent calculation scheme to other classical spin systems with sufficiently smooth Hamiltonians H, for which a symplectic integrators can be constructed. In such models, one could systematically scan over the global system parameters and ensembles of initial conditions, as

done in this work, to map out regions of integrable and chaotic dynamics and to search for possible hidden integrals of motion.

Secondly, the present work has effectively focused on the temperature $T = \infty$ situation in the uniform ensemble, where initial configurations sample the energy shell without Boltzmann weighting. A possible extension is to study finite-temperature $T < \infty$ ensembles, in which initial configurations are drawn from a Gibbs distribution with weight $\propto \exp(-H/T)$ for $T < \infty$. This would require additional information about the density of states, or the use of Monte Carlo techniques such as Gibbs sampling to generate representative initial conditions. Such a finite-temperature generalization would allow one to investigate how Lyapunov's exponents depend on temperature and to relate them more directly to thermodynamic properties.

Finally, we remark that almost all of our results have been obtained for systems with $N = 17$ spins, with only a single computation of the Lyapunov spectrum at $N = 100$. Analyzing the 17 spin system is sufficient to reveal an already complex structure of integrable and chaotic regimes, but it does not allow us gain concrete insight into the thermodynamic limit. A suggestion for future work is therefore to repeat the presented analysis for larger system sizes and to study how quantities such as the maximal Lyapunov's exponent and the existence and size of integrable plateaus scale with N. However, it is reasonable to expect that the qualitative results obtained here (plateaus of integrability near $R \approx 0$ and $R \approx 1$, strongest chaos consistently near $R \approx 0.75$) persists in the large-N limit.

8

DATA AVAILABILITY STATEMENT

All data and codes used in this work are openly available at *https://doi.org/10.4121/286901ce-d227-4add-b06d-4cc12d137227* [Hui25].

REFERENCES

[Arn63] **V. I. Arnold**. “Small Denominators and Problems of Stability of Motion in Classical and Celestial Mechanics”. In: *Russian Mathematical Surveys* 18.6 (1963), pp. 85–191. doi: 10.1070/RM1963v018n06ABEH001143.

[Arn89] **V. I. Arnold**. *Mathematical Methods of Classical Mechanics*. 2nd ed. Vol. 60. Graduate Texts in Mathematics. New York: Springer, 1989. doi: 10.1007/978-1-4757-1693-1.

[Bäc07] **A. Bäcker**. “Quantum Chaos in Billiards”. In: *Computing in Science & Engineering* 9 (2007). doi: 10.1109/MCSE.2007.61.

[Bar+08] **J. C. Barba, F. Finkel, A. González-López, and M. A. Rodríguez**. “The Polychronakos–Frahm spin chain of BC_N type and the Berry–Tabor conjecture”. In: *Physical Review B* 77 (2008), p. 214422. doi: 10.1103/PhysRevB.77.214422.

[Ben+80a] **G. Benettin, L. Galgani, A. Giorgilli, and J.-M. Strelcyn**. “Lyapunov Characteristic Exponents for smooth dynamical systems and for hamiltonian systems; a method for computing all of them. Part 1: Theory”. In: *Meccanica* 15.1 (1980), pp. 9–20. doi: 10.1007/BF02128236.

[Ben+80b] **G. Benettin, L. Galgani, A. Giorgilli, and J.-M. Strelcyn**. “Lyapunov characteristic exponents for smooth dynamical systems and for Hamiltonian systems; a method for computing all of them. Part 2: Numerical application”. In: *Meccanica* 15.1 (1980), pp. 21–30. doi: 10.1007/BF02128237.

[BP23] **G. Benettin and A. Ponno**. “FPU Model and Toda Model: A Survey, a View”. In: *From Kinetic Theory to Turbulence Modeling*. Vol. 51. Springer INdAM Series. Springer, 2023, pp. 21–44. doi: 10.1007/978-981-19-6462-6_3.

[BBW04] **J. Berges, S. Borsányi, and C. Wetterich**. “Prethermalization”. In: *Phys. Rev. Lett.* 93 (14 2004), p. 142002. doi: 10.1103/PhysRevLett.93.142002.

[BT77a] **M. V. Berry and M. Tabor**. “Level clustering in the regular spectrum”. In: *Proceedings of the Royal Society of London A* 356 (1977), pp. 375–394. doi: 10.1098/rspa.1977.0140.

[BT77b] **M. V. Berry and M. Tabor**. “Level Clustering in the Regular Spectrum”. In: *Proceedings of the Royal Society of London A* 356.1686 (1977), pp. 375–394. doi: 10.1098/rspa.1977.0140.

[BCM24] **S. Blanes, F. Casas, and A. Murua**. “Splitting methods for differential equations”. In: *Acta Numerica* 33 (2024), pp. 1–161. doi: 10.1017/S0962492923000077.

[BGS84] **O. Bohigas, M. J. Giannoni, and C. Schmit**. “Characterization of Chaotic Quantum Spectra and Universality of Level Fluctuation Laws”. In: *Physical Review Letters* 52 (1984), pp. 1–4. doi: 10.1103/PhysRevLett.52.1.

[BSS92] **J. Bolte, G. Steil, and F. Steiner**. “Arithmetical chaos and violation of universality in energy level statistics”. In: *Physical Review Letters* 69.15 (1992), pp. 2188–2191. doi: 10.1103/PhysRevLett.69.2188.

[CH96] **N. I. Chernov and C. Haskell**. “Nonuniformly hyperbolic K-systems are Bernoulli”. In: *Ergodic Theory and Dynamical Systems* 16 (1996), pp. 19–44.

[Chi79] **B. V. Chirikov**. “A universal instability of many-dimensional oscillator systems”. In: *Physics Reports* 52.5 (1979), pp. 263–379. doi: 10.1016/0370-1573(79)90023-1.

[dSil01] **A. C. da Silva**. *Lectures on Symplectic Geometry*. Vol. 1764. Lecture Notes in Mathematics. Berlin: Springer, 2001. doi: 10.1007/978-3-540-45330-7.

[ER85] **J.-P. Eckmann and D. Ruelle**. “Ergodic theory of chaos and strange attractors”. In: *Reviews of Modern Physics* 57.3 (1985), pp. 617–656. doi: 10.1103/RevModPhys.57.617.

[Fer+55] **E. Fermi, P. Pasta, S. Ulam, and M. Tsingou**. *Studies of nonlinear problems*. Tech. rep. LA-1940. Los Alamos, New Mexico: Los Alamos Scientific Laboratory, 1955. doi: 10.2172/4376203.

[Fin+14] **B. V. Fine, T. A. Elsayed, C. M. Kropf, and A. S. de Wijn**. “Absence of exponential sensitivity to small perturbations in nonintegrable systems of spins 1/2”. In: *Physical Review E* 89.1 (2014), p. 012923. doi: 10.1103/PhysRevE.89.012923.

[Fis08] **T. A. Fisher**. “Linear Algebra: Non-degenerate Bilinear Forms”. Department of Pure Mathematics and Mathematical Statistics, University of Cambridge. 2008. url: https://www.dpmms.cam.ac.uk/study/IB/LinearAlgebra/2008-2009/bilinear-08.pdf.

[For92] **J. Ford**. “The Fermi–Pasta–Ulam Problem: Paradox Turns Discovery”. In: *Physics Reports* 213.5 (1992), pp. 271–310. doi: 10.1016/0370-1573(92)90116-H.

[Fro84] **C. Froeschlé**. “The Lyapunov characteristic exponents—applications to celestial mechanics”. In: *Celestial Mechanics* 34 (1984), pp. 95–115. doi: 10.1007/BF01235793.

[Gal08] **G. Gallavotti**. *The Fermi–Pasta–Ulam Problem: A Status Report*. Vol. 728. Lecture Notes in Physics. Berlin: Springer, 2008. doi: 10.1007/978-3-540-72995-2.

[GS98] **B. Georgeot and D. L. Shepelyansky**. “Integrability and Quantum Chaos in Spin Glass Shards”. In: *Phys. Rev. Lett.* 81 (23 1998), pp. 5129–5132. doi: 10.1103/PhysRevLett.81.5129.

[Gha+20] **H. Gharibyan, M. Hanada, B. Swingle, and M. Tezuka**. “A characterization of quantum chaos by two-point correlation functions”. In: *Physical Review E* 102 (2020), p. 022213. doi: 10.1103/PhysRevE.102.022213.

[GPS02] **H. Goldstein, C. P. Poole, and J. L. Safko**. *Classical Mechanics*. 3rd ed. San Francisco: Addison-Wesley, 2002.

[Gor+06] **T. Gorin, T. Prosen, T. H. Seligman, and M. Žnidarič**. “Dynamics of Loschmidt Echoes and Fidelity Decay”. In: *Physics Reports* 435.2–5 (2006), pp. 33–156. issn: 0370-1573. doi: 10.1016/j.physrep.2006.09.003.

[GMW98] **T. Guhr, A. Müller-Groeling, and H. A. Weidenmüller**. "Random-matrix theories in quantum physics: common concepts". In: *Physics Reports* 299.4–6 (1998), pp. 189–425. doi: 10.1016/S0370-1573(97)00088-4.

[Haa10] **F. Haake**. *Quantum Signatures of Chaos*. 3rd ed. Berlin: Springer, 2010. doi: 10.1007/978-3-642-05428-0.

[HLW06] **E. Hairer, C. Lubich, and G. Wanner**. *Geometric Numerical Integration: Structure-Preserving Algorithms for Ordinary Differential Equations*. 2nd ed. Vol. 31. Springer Series in Computational Mathematics. Berlin: Springer, 2006. doi: 10.1007/3-540-30666-8.

[Ham34] **W. R. Hamilton**. "On a General Method in Dynamics". In: *Philosophical Transactions of the Royal Society of London* 124 (1834), pp. 247–308.

[Heb00] **E. Hebey**. *Nonlinear Analysis on Manifolds: Sobolev Spaces and Inequalities*. Vol. 5. Courant Lecture Notes in Mathematics. American Mathematical Society, 2000.

[HK08] **A. Henrici and T. Kappeler**. *Birkhoff normal form for the periodic Toda lattice*. Contemporary Mathematics. American Mathematical Society, 2008, pp. 11–19. isbn: 978-0-8218-4150-1.

[HK09] **A. Henrici and T. Kappeler**. "Nekhoroshev theorem for the periodic Toda lattice". In: *Chaos: An Interdisciplinary Journal of Nonlinear Science* 19.3 (2009). doi: 10.1063/1.3196783.

[Hui25] **E. Huisman**. *Experimental data for classical spin system simulations*. 4TU.ResearchData, 2025. doi: 10.4121/286901ce-d227-4add-b06d-4cc12d137227. url: https://doi.org/10.4121/286901ce-d227-4add-b06d-4cc12d137227.

[Ish82] **Y. Ishimori**. "An Integrable Classical Spin Chain". In: *Journal of the Physical Society of Japan* 51.11 (1982), pp. 3417–3418. doi: 10.1143/JPSJ.51.3417.

[JP01] **R. A. Jalabert and H. M. Pastawski**. "Environment-Independent Decoherence Rate in Classically Chaotic Systems". In: *Physical Review Letters* 86.12 (2001), pp. 2490–2493. doi: 10.1103/PhysRevLett.86.2490.

[Kat80] **A. Katok**. "Lyapunov exponents, entropy and periodic orbits for diffeomorphisms". In: *Publications Mathématiques de l'IHÉS* 51 (1980), pp. 137–173.

[Khi49] **A. I. Khinchin**. *Mathematical Foundations of Statistical Mechanics*. New York: Dover, 1949.

[Kol54] **A. N. Kolmogorov**. "On Conservation of Conditionally Periodic Motions for a Small Change in Hamilton's Function". In: *Doklady Akademii Nauk SSSR* 98 (1954), pp. 527–530.

[Lag88] **J.-L. Lagrange**. *Mécanique analytique*. English translation: *Analytical Mechanics*. Paris: Veuve Desaint, 1788.

[LL80] **L. D. Landau and E. M. Lifshitz**. *Statistical Physics, Part 1*. 3rd ed. Vol. 5. Course of Theoretical Physics. Oxford: Pergamon Press, 1980.

[Lee97] **J. M. Lee**. *Riemannian Manifolds: An Introduction to Curvature*. Vol. 176. Graduate Texts in Mathematics. New York: Springer, 1997. doi: 10.1007/b98852.

[Lee13] **J. M. Lee**. *Introduction to Smooth Manifolds*. 2nd ed. Vol. 218. Graduate Texts in Mathematics. New York: Springer, 2013. doi: 10.1007/978-1-4419-9982-5.

[Lee24] **J. M. Lee**. *Introduction to Complex Manifolds*. Vol. 244. Graduate Studies in Mathematics. American Mathematical Society, 2024.

[LW95] **C. Liverani and M. P. Wojtkowski**. "Ergodicity in Hamiltonian systems". In: *Dynamics Reported. Expositions in Dynamical Systems. New Series*. Ed. by C. K. R. T. Jones, U. Kirchgraber, and H. O. Walther. Vol. 4. Berlin: Springer-Verlag, 1995, pp. 130–202.

[Lya92] **A. M. Lyapunov**. "The General Problem of the Stability of Motion". PhD thesis. Imperial University of Kharkov, 1892.

[Mar93] **R. Markarian**. "New ergodic billiards: exact results". In: *Nonlinearity* 6 (1993), pp. 819–841.

[MS17] **D. McDuff and D. Salamon**. *Introduction to Symplectic Topology*. 3rd ed. Oxford: Oxford University Press, 2017.

[Mos62] **J. Moser**. "On Invariant Curves of Area-Preserving Mappings of an Annulus". In: *Nachrichten der Akademie der Wissenschaften in Göttingen, II. Mathematisch-Physikalische Klasse* (1962), pp. 1–20.

[Nek77] **N. N. Nekhoroshev**. "An exponential estimate of the time of stability of nearly-integrable Hamiltonian systems". In: *Russian Mathematical Surveys* 32.6 (1977), pp. 1–65.

[New87] **I. Newton**. *Philosophiæ Naturalis Principia Mathematica*. English translation: *The Mathematical Principles of Natural Philosophy*. London: Royal Society, 1687.

[Ose68] **V. I. Oseledets**. "A multiplicative ergodic theorem. Lyapunov characteristic numbers for dynamical systems". In: *Transactions of the Moscow Mathematical Society* 19 (1968), pp. 197–231.

[Pes77] **Y. B. Pesin**. "Lyapunov characteristic exponents and smooth ergodic theory". In: *Russian Mathematical Surveys* 32.4 (1977), pp. 55–114. doi: 10.1070/RM1977v032n04ABEH001639.

[PP16] **A. Pikovsky and A. Politi**. *Lyapunov Exponents: A Tool to Explore Complex Dynamics*. Cambridge: Cambridge University Press, 2016. isbn: 978-1-107-03042-8.

[Poi09] **S.-D. Poisson**. *Traite de mecanique*. Paris: Courcier, 1809.

[Pro02] **T. Prosen**. "On General Relation between Quantum Ergodicity and Fidelity of Quantum Dynamics". In: *Physical Review E* 65.3 (2002), p. 036208. doi: 10.1103/PhysRevE.65.036208.

[PŽ02] **T. Prosen and M. Žnidarič**. "Stability of quantum motion and correlation decay". In: *Journal of Physics A: Mathematical and General* 35.6 (2002), pp. 1455–1481. doi: 10.1088/0305-4470/35/6/309.

[Rei08] **P. Reimann**. "Foundation of Statistical Mechanics under Experimentally Realistic Conditions". In: *Physical Review Letters* 101 (2008), p. 190403. doi: 10.1103/PhysRevLett.101.190403.

[RPW71] **W.-K. Rhim, A. Pines, and J. S. Waugh**. "Time-Reversal Experiments in Dipolar-Coupled Spin Systems". In: *Physical Review B* 3.3 (1971), pp. 684–696. doi: 10.1103/PhysRevB.3.684.

[SN20] **J. J. Sakurai and J. Napolitano**. *Modern Quantum Mechanics*. 3rd ed. Cambridge University Press, 2020.

[STB03] **P. G. Silvestrov, J. Tworzydło, and C. W. J. Beenakker**. "Hypersensitivity to perturbations of quantum-chaotic wave-packet dynamics". In: *Physical Review E* 67.2 (2003), p. 025204. doi: 10.1103/PhysRevE.67.025204.

[Sin70] **Y. G. Sinai**. "Dynamical systems with elastic reflections. Ergodic properties of dispersing billiards". In: *Russian Mathematical Surveys* 25.2 (1970), pp. 137–189. doi: 10.1070/RM1970v025n02ABEH003794.

[Sli90] **C. P. Slichter**. *Principles of Magnetic Resonance*. 3rd enlarged and updated. Vol. 1. Springer Series in Solid-State Sciences. Berlin, Heidelberg: Springer, 1990.

[Ste05] **R. Steinigeweg**. "Zur Dynamik von klassischen Heisenberg-Systemen: Klassen integrabler Systeme und symplektische Integratoren für nicht integrable Systeme". MA thesis. Osnabrück: Universität Osnabrück, 2005.

[Stö99] **H.-J. Stöckmann**. *Quantum Chaos: An Introduction*. Cambridge: Cambridge University Press, 1999.

[Suz90] **M. Suzuki**. "Fractal decomposition of exponential operators with applications to many-body theories and Monte Carlo simulations". In: *Physics Letters A* 146.6 (1990), pp. 319–323. doi: 10.1016/0375-9601(90)90962-N.

[Szá92] **D. Szász**. "On the K-property of some planar hyperbolic billiards". In: *Communications in Mathematical Physics* 145 (1992), pp. 595–604.

[Tex20] **C. Texier**. "Fluctuations of the Product of Random Matrices and Generalized Lyapunov Exponent". In: *Journal of Statistical Physics* 181.3 (2020), pp. 990–1051. doi: 10.1007/s10955-020-02617-w.

[Tod67] **M. Toda**. "Vibration of a Chain with Nonlinear Interaction". In: *Journal of the Physical Society of Japan* 22.2 (1967), pp. 431–436. doi: 10.1143/JPSJ.22.431.

[Tol38] **R. C. Tolman**. *The Principles of Statistical Mechanics*. Oxford: Clarendon Press, 1938.

[Tro59] **H. F. Trotter**. "On the product of semi-groups of operators". In: *Proceedings of the American Mathematical Society* 10.4 (1959), pp. 545–551. doi: 10.1090/S0002-9939-1959-0108732-6.

[Van08] **S. Vandoren**. *Lectures on Riemannian Geometry, Part II: Complex Manifolds*. https://webspace.science.uu.nl/~vando101/MRIlectures.pdf. MRI Masterclass in Mathematics, Utrecht University. 2008.

[Via14] **M. Viana**. *Lectures on Lyapunov Exponents*. Vol. 145. Cambridge Studies in Advanced Mathematics. Cambridge University Press, 2014. doi: 10.1017/CBO9781139976602.

[Via] **M. Viana**. "Theorem of Oseledets". Lecture notes, Instituto Nacional de Matemática Pura e Aplicada (IMPA). url: https://w3.impa.br/~viana/out/ltosel.pdf.

[Wig51] **E. P. Wigner**. "On the Statistical Distribution of the Widths and Spacings of Nuclear Resonance Levels". In: *Mathematical Proceedings of the Cambridge Philosophical Society* 47.4 (1951), pp. 790–798. doi: 10.1017/S0305004100027237.

[Woj86] **M. Wojtkowski**. “Principles for the design of billiards with nonvanishing Lyapunov exponents”. In: *Communications in Mathematical Physics* 105 (1986), pp. 391–414.

[Yos90] **H. Yoshida**. “Construction of higher order symplectic integrators”. In: *Physics Letters A* 150.5–7 (1990), pp. 262–268. doi: 10.1016/0375-9601(90)90092-3.

[Zas07] **G. M. Zaslavsky**. *The Physics of Chaos in Hamiltonian Systems*. 2nd. Imperial College Press, 2007. doi: 10.1142/p507.

A

APPENDIX

A.1. DERIVING THE GAUSSIAN ORTHOGONAL ENSEMBLE

Let H be a real symmetric 2×2 matrix with

$$P(H_{11}, H_{12}, H_{22}) \propto \exp(-c(H_{11}^2 + 2H_{12}^2 + H_{22}^2))$$

Firstly, write H in the following representation, with $E_1 \geq E_2$,

$$H \equiv \begin{pmatrix} H_{11} & H_{12} \\ H_{21} & H_{22} \end{pmatrix} = R(\theta) \begin{pmatrix} E_1 & 0 \\ 0 & E_2 \end{pmatrix} R^T(\theta)$$

where

$$R(\theta) = \begin{pmatrix} \cos(\theta) & \sin(\theta) \\ -\sin(\theta) & \cos(\theta) \end{pmatrix}.$$

Then, a calculation of the Jacobian yields

$$|\det(J(E_1, E_2, \theta))| = |\det(\frac{\partial(H_{11}, H_{12}, H_{22})}{\partial(E_1, E_2, \theta)})| = |E_1 - E_2|$$

and

$$\begin{aligned} P(E_1, E_2, \theta) &= |\det(J(E_1, E_2, \theta))| P(H_{11}, H_{12}, H_{22}) \\ &\propto |E_1 - E_2| \exp(-c(E_1^2 + E_2^2)). \end{aligned}$$

Note that integrating over θ only results in a constant factor. Introduce the level spacing $s = E_1 - E_2$ and level average $\bar{E} = \frac{E_1 + E_2}{2}$. A short calculation yields

$$|\det(J(s, \bar{E}))| = 1$$

and

$$P(s, \bar{E}) = P(E_1, E_2, \theta) \propto |s| \exp(-c(2\bar{E}^2 + \frac{s^2}{2})).$$

Note that $s \geq 0$. Integrating over $\bar{E}$ results in another constant factor

$$P(s) = As \exp(-c\frac{s^2}{2}).$$

Then, normalizing the distribution through

$$1 = \int_0^\infty P(s)ds = A \int_0^\infty s \exp(-c\frac{s^2}{2})ds = \frac{A}{c}$$

and enforcing the mean energy spacing $\langle s \rangle$ to be 1 through

$$1 = \langle s \rangle = \int_0^\infty sP(s)ds = c \int_0^\infty s^2 \exp(-c\frac{s^2}{2}) = \frac{2c}{\pi}$$

results in the following distribution for the level spacing s

$$P_{\text{GOE}}(s) \equiv P(s) = \frac{\pi}{2} s \exp(-\frac{\pi}{4} s^2). \tag{A.1}$$

A

A.2. SYMPLECTIC MANIFOLDS

The definitions and theorems presented in this appendix are adapted from [dSil01; Lee13; MS17].

Definition 1. Let X and Y be topological spaces. A map $f : X \to Y$ is a homeomorphism if it is bijective, continuous, and its inverse $f^{-1} : Y \to X$ is also continuous.

Definition 2. A topological space X is called Hausdorff if for every pair of distinct points $p, q \in X$ there exist open sets $U, V \subset X$ such that

$$p \in U, \quad q \in V, \quad \text{and} \quad U \cap V = \emptyset.$$

Definition 3. A topological space X is called second countable if there exists a countable collection of open sets $\{B_k\}_{k\in\mathbb{N}}$ such that every open set $U \subset X$ can be written as a union of some of the B_k. Such a collection $\{B_k\}$ is called a countable base for the topology on X.

Definition 4. A space M is an n-dimensional manifold if and only if it is Hausdorff, second countable, and for every $p \in M$ there exist an open neighborhood $U \subset M$ of p and a homeomorphism $\varphi : U \to \varphi(U) \subset \mathbb{R}^n$ with $\varphi(U)$ open.

Definition 5. A chart on M is a pair (U, φ) with $U \subset M$ open and $\varphi : U \to \varphi(U) \subset \mathbb{R}^n$ a homeomorphism. Two charts (U, φ) and (U', ψ) with $U \cap U' \neq \emptyset$ are C^∞-compatible if the transition map $\psi \circ \varphi^{-1} : \varphi(U \cap U') \to \psi(U \cap U')$ and its inverse are smooth. An atlas is a collection $\mathcal{A} = \{(U_\alpha, \varphi_\alpha)\}$ with $\bigcup_\alpha U_\alpha = M$. A maximal C^∞-atlas contains every chart C^∞-compatible with all its charts.

Remark 6. Given a chart (U, φ) as above, the map $\varphi : U \to \mathbb{R}^n$ can be written in components as

$$\varphi(p) = \big(x^1(p), \ldots, x^n(p)\big), \quad p \in U,$$

where each $x^i : U \to \mathbb{R}$ is a smooth function. The functions $x^1, \ldots, x^n$ are called the coordinate functions of the chart (U, φ), and the n-tuple $(x^1, \ldots, x^n)$ is often used as a shorthand for the map φ itself. In particular, for $p \in U$ we may think of $(x^1(p), \ldots, x^n(p))$ as the coordinates of the point p in this chart.

Definition 7. An n-dimensional manifold M equipped with a maximal C^∞-atlas is called a smooth n-manifold.

Definition 8. Let M be a smooth n-manifold and $p \in M$. A linear map $v : C^\infty(M) \to \mathbb{R}$ is a derivation at p if $v(fg) = f(p)\, v(g) + v(f)\, g(p)$ for all $f, g \in C^\infty(M)$. The set of derivations at p is the tangent space T_pM. The tangent bundle is $TM := \bigsqcup_{p\in M} T_pM$.

Definition 9. For $U \subset M$ open, a smooth vector field on U is a map $X : C^\infty(U) \to C^\infty(U)$ that is $\mathbb{R}$-linear and satisfies $X(fg) = f\,X(g) + g\,X(f)$ for all $f, g \in C^\infty(U)$, and such that for each $p \in U$ the evaluation $f \mapsto (Xf)(p)$ is a derivation at p. The set of all smooth vector fields on U is denoted $\mathfrak{X}(U)$.

Definition 10. For each $p \in M$, the cotangent space is the dual space

$T_p^*M := (T_pM)^*$, and the cotangent bundle is

$$T^*M := \bigsqcup_{p\in M} T_p^*M = \{(p,\xi) | p \in M, \xi \in T_p^*M\}.$$

Note that $T * M$ is a manifold [Lee13, Proposition 11.9]. A smooth 1-form on U is a smooth section $\alpha : U \to T^*M$, i.e. $\alpha(p) \in T_p^*M$ depends smoothly on p. The space of smooth 1-forms on U is $\Omega^1(U)$.

Definition 11. Let $(U,\varphi) = (U,(x^1,\dots,x^n))$ be a chart on a smooth n-dimensional manifold M. For $f \in C^\infty(U)$ define the coordinate vector fields $\partial_i \in \mathfrak{X}(U)$ by

$$(\partial_i f)(p) := \frac{\partial(f\circ\varphi^{-1})}{\partial x^i}(\varphi(p)), \qquad p \in U,\ i = 1,\dots,n.$$

For each $p \in U$, the vectors

$$\partial_1|_p,\dots,\partial_n|_p \in T_pM$$

form a basis of the tangent space T_pM.

Define the coordinate 1-forms $dx^i \in \Omega^1(U)$ as the $C^\infty(U)$-linear dual to the coordinate vector fields ∂_i:

$$dx^i(\partial_j) = \delta_{ij}, \qquad dx^i\left(\sum_j X^j\partial_j\right) = X^i$$

for all smooth functions $X^j \in C^\infty(U)$. Equivalently, for each $p \in U$ the set

$$dx^1|_p,\dots,dx^n|_p \in T_p^*M$$

form the basis of T_p^*M dual to the basis $\{\partial_1|_p,\dots,\partial_n|_p\}$ of T_pM.

Definition 12. Let $\Lambda^k(T_p^*M)$ denote the space of alternating k-linear maps $\underbrace{T_pM\times\cdots\times T_pM}_{k \text{ times}} \to \mathbb{R}$. A k-form on U is a smooth section of $\Lambda^k(T^*M)$, the space of k-forms is $\Omega^k(U)$. In particular $\Omega^0(U) = C^\infty(U)$ and $\Omega^1(U)$ is as above. There is a bilinear wedge product $\wedge : \Omega^k(U)\times\Omega^\ell(U) \to \Omega^{k+\ell}(U)$ characterized by

$$(\alpha\wedge\beta)(X_1,\dots,X_{k+\ell})$$

$$:= \frac{1}{k!\,\ell!}\sum_{\sigma\in S_{k+\ell}} \operatorname{sgn}(\sigma)\,\alpha(X_{\sigma(1)},\dots,X_{\sigma(k)})\,\beta(X_{\sigma(k+1)},\dots,X_{\sigma(k+\ell)}),$$

for $\alpha \in \Omega^k(U)$, $\beta \in \Omega^\ell(U)$, and $X_i \in \mathfrak{X}(U)$. $S_{k+\ell}$ denotes the symmetric group of all permutations of $\{1,\dots,k+\ell\}$ and $\operatorname{sgn}(\sigma) \in \{+1,-1\}$ is the sign of the permutation σ. It is associative, $C^\infty(U)$-bilinear, and commutative in the sense of $\alpha\wedge\beta = (-1)^{k\ell}\beta\wedge\alpha$.

Remark 13. In a chart (U,φ), $\{dx^{i_1}\wedge\cdots\wedge dx^{i_k}\}_{i_1<\dots<i_k}$ is a local $C^\infty(U)$-basis of $\Omega^k(U)$. So any $\alpha \in \Omega^k(U)$ has a unique expression $\alpha = \sum_{i_1<\dots<i_k} a_{i_1\dots i_k}\,dx^{i_1}\wedge\cdots\wedge dx^{i_k}$ with smooth coefficients $a_{i_1\dots i_k}$.

Remark 14. In the special case $k = \ell = 1$, the wedge product of two 1-forms $\alpha,\beta \in \Omega^1(U)$ is the 2-form $\alpha\wedge\beta \in \Omega^2(U)$ given explicitly by

$$(\alpha\wedge\beta)(X,Y) = \alpha(X)\beta(Y) - \alpha(Y)\beta(X), \qquad X,Y \in \mathfrak{X}(U).$$

A

In particular, for the coordinate 1-forms $dx^i, dx^j \in \Omega^1(U)$ one has

$$(dx^i \wedge dx^j)(X,Y) = dx^i(X)\,dx^j(Y) - dx^i(Y)\,dx^j(X).$$

This shows directly that $\alpha \wedge \beta = -\beta \wedge \alpha$ for 1-forms.

Definition 15. There is a unique $\mathbb{R}$-linear map $d : \Omega^k(U) \to \Omega^{k+1}(U)$ for all $k \geq 0$ called the exterior derivative such that:

(i) $df(X) = X(f)$, for all $f \in C^\infty(U) = \Omega^0(U)$, $X \in \mathfrak{X}(U)$,

(ii) $d(\alpha \wedge \beta) = d\alpha \wedge \beta + (-1)^k \alpha \wedge d\beta$, for $\alpha \in \Omega^k(U)$, $\beta \in \Omega^\ell(U)$,

(iii) $d \circ d = 0$.

In coordinates, if $\alpha = \sum_{i_1 < \cdots < i_k} a_{i_1 \cdots i_k}\, dx^{i_1} \wedge \cdots \wedge dx^{i_k}$, then

$$d\alpha = \sum_{i_1 < \cdots < i_k} \sum_{j=1}^{n} \frac{\partial a_{i_1 \cdots i_k}}{\partial x^j}\, dx^j \wedge dx^{i_1} \wedge \cdots \wedge dx^{i_k}.$$

A form α is closed if $d\alpha = 0$.

Definition 16. A smooth 2-form on M is an element of $\Omega^2(M)$. Locally, in a chart (U, φ),

$$\omega\big|_U = \sum_{1 \leq i < j \leq n} \omega_{ij}\, dx^i \wedge dx^j, \qquad \omega_{ij} \in C^\infty(U).$$

Equivalently, ω is represented by a skew-symmetric matrix (ω_{ij}) in coordinates.

Definition 17. For a finite-dimensional real vector space V, a skew bilinear form $\eta \in \Lambda^2(V^*)$ is nondegenerate if for any $v \neq 0$ there exists an $w \in V$ such that $\eta(v, w) \neq 0$.

Definition 18. A symplectic manifold is a smooth manifold M equipped with a smooth 2-form $\omega \in \Omega^2(M)$ that is closed ($d\omega = 0$) and nondegenerate. The form ω is called the symplectic form.

Theorem 19. Let (M, ω) be a symplectic manifold. Then for every $p \in M$, the tangent space T_pM has even dimension. In particular, M is an even-dimensional manifold.

Definition 20. Let (M, ω) be a symplectic manifold. For each $p \in M$, the nondegenerate 2-form $\omega_p \in \Lambda^2(T_p^*M)$ defines a linear map

$$\omega_p^\flat : T_pM \to T_p^*M, \qquad \omega_p^\flat(v)(w) := \omega_p(v, w), \quad v, w \in T_pM.$$

Nondegeneracy of ω_p means that $\omega_p^\flat$ is an isomorphism for every p. These pointwise maps assemble to a smooth vector bundle isomorphism

$$\omega^\flat : TM \to T^*M.$$

Theorem 21. *Let (M, ω) be a symplectic $2n$-dimensional manifold and let $(U, (x^1, \ldots, x^n))$ be a chart. On U write*

$$\omega = \frac{1}{2} \sum_{i=1}^{2n} \sum_{j=1}^{2n} \omega_{ij}\, dx^i \wedge dx^j, \qquad \omega_{ij} = -\omega_{ji}.$$

Let $\partial_i := \frac{\partial}{\partial x^i}$ be the associated coordinate vector fields. Then for each $k \in \{1, \dots, n\}$,

$$\omega^\flat(\partial_k) = \sum_{j=1}^{2n} \omega_{kj}\, dx^j.$$

Proof. We compute $\omega^\flat$ on the coordinate basis $\{\partial_1, \dots, \partial_n\}$, where $\partial_i := \frac{\partial}{\partial x^i}$. Let $k \in \{1, \dots, n\}$ and Y be any vector field. Then

$$\begin{aligned}
\omega^\flat(\partial_k)(Y) = \omega(\partial_k, Y) &= \frac{1}{2} \sum_{i=1}^{2n} \sum_{j=1}^{n} \omega_{ij} (dx^i \wedge dx^j)(\partial_k, Y) \\
&= \frac{1}{2} \sum_{i=1}^{2n} \sum_{j=1}^{2n} \omega_{ij} \big(dx^i(\partial_k)\, dx^j(Y) - dx^i(Y)\, dx^j(\partial_k) \big) \\
&= \frac{1}{2} \sum_{i=1}^{2n} \sum_{j=1}^{2n} \omega_{ij} \big(\delta_{ik}\, dx^j(Y) - dx^i(Y)\, \delta_{jk} \big) \\
&= \frac{1}{2} \sum_{j=1}^{2n} \omega_{kj}\, dx^j(Y) - \frac{1}{2} \sum_{i=1}^{2n} \omega_{ik}\, dx^i(Y).
\end{aligned}$$

In the second sum, rename the index $i \mapsto j$ and use skew-symmetry $\omega_{jk} = -\omega_{kj}$:

$$-\frac{1}{2} \sum_{i=1}^{2n} \omega_{ik}\, dx^i(Y) = -\frac{1}{2} \sum_{i=1}^{2n} \omega_{jk}\, dx^j(Y) = \frac{1}{2} \sum_{i=1}^{2n} \omega_{kj}\, dx^j(Y).$$

Hence the two terms are equal, and we obtain

$$\omega^\flat(\partial_k)(Y) = \sum_{j=1}^{2n} \omega_{kj}\, dx^j(Y).$$

Since this holds for all Y, we conclude that

$$\omega^\flat(\partial_k) = \sum_{j=1}^{2n} \omega_{kj}\, dx^j.$$

□

Definition 22. Since $\omega^\flat : TM \to T^*M$ is a vector bundle isomorphism, it has a smooth inverse

$$\omega^\sharp : T^*M \to TM,$$

Equivalently, for each $p \in M$, the map

$$\omega_p^\sharp : T_p^*M \to T_pM$$

is the inverse of $\omega_p^\flat$. In particular, for any $v \in T_pM$ and $\alpha \in T_p^*M$,

$$\alpha = \omega_p^\flat(v) \iff v = \omega_p^\sharp(\alpha).$$

Theorem 23. *Let (M, ω) be a symplectic $2n$-dimensional manifold and*

A

let $(U, (x^1, \dots, x^n))$ be a chart. On U write

$$\omega = \frac{1}{2} \sum_{i,j=1}^{n} \omega_{ij}\, dx^i \wedge dx^j, \qquad \omega_{ij} = -\omega_{ji}.$$

Let $\partial_i := \frac{\partial}{\partial x^i}$ be the associated coordinate vector fields. Then there exist unique functions $\pi^{ij} \in C^\infty(U)$ such that

$$\omega^\sharp(dx^j) = \sum_{i=1}^{2n} \pi^{ij}\, \partial_i, \qquad j = 1, \dots, n,$$

and these satisfy

$$\sum_{i=1}^{2n} \omega_{ik}\, \pi^{ij} = \delta_{jk} \quad \text{for all } j, k \in \{1, \dots, n\}.$$

Moreover, for any 1-form $\alpha = \sum_{j=1}^{n} \alpha_j\, dx^j$ on U we have

$$\omega^\sharp(\alpha) = \sum_{i=1}^{2n} \sum_{j=1}^{2n} \pi^{ij}\, \alpha_j\, \partial_i.$$

Proof. From Theorem 14 we know that on U

$$\omega^\flat(\partial_i) = \sum_{k=1}^{2n} \omega_{ik}\, dx^k \quad \text{for each } i = 1, \dots, n.$$

By definition, $\omega^\sharp : T^*M \to TM$ is the inverse of $\omega^\flat : TM \to T^*M$, so in particular

$$\omega^\flat\big(\omega^\sharp(\alpha)\big) = \alpha \quad \text{for all } \alpha \in T^*M.$$

Fix $j \in \{1, \dots, n\}$. Since $\{\partial_i\}_{i=1}^{2n}$ is a basis of TM on U, there exist unique smooth functions π^{ij} on U such that

$$\omega^\sharp(dx^j) = \sum_{i=1}^{2n} \pi^{ij}\, \partial_i.$$

Applying $\omega^\flat$ and using linearity, we obtain

$$dx^j = \omega^\flat\big(\omega^\sharp(dx^j)\big) = \omega^\flat\Big(\sum_{i=1}^{2n} \pi^{ij}\, \partial_i\Big) = \sum_{i=1}^{2n} \pi^{ij}\, \omega^\flat(\partial_i) = \sum_{i=1}^{2n} \pi^{ij} \Big(\sum_{k=1}^{2n} \omega_{ik}\, dx^k\Big).$$

Thus

$$dx^j = \sum_{k=1}^{2n} \Big(\sum_{i=1}^{2n} \omega_{ik}\, \pi^{ij}\Big)\, dx^k.$$

Since $\{dx^k\}_{k=1}^{2n}$ is a basis of T^*M on U, the coefficients of dx^k on both sides must agree, hence for all k,

$$\sum_{i=1}^{2n} \omega_{ik}\, \pi^{ij} = \delta_{jk}.$$

This shows the stated relation between the coefficients π^{ij}. Finally, let $\alpha = \sum_{j=1}^{2n} \alpha_j\, dx^j$ be an arbitrary 1-form on U. By linearity of $\omega^\sharp$,

$$\omega^\sharp(\alpha) = \omega^\sharp\Big(\sum_{j=1}^{2n} \alpha_j\, dx^j\Big) = \sum_{j=1}^{2n} \alpha_j\, \omega^\sharp(dx^j) = \sum_{j=1}^{2n} \alpha_j \Big(\sum_{i=1}^{2n} \pi^{ij}\, \partial_i\Big) = \sum_{i=1}^{2n} \sum_{j=1}^{2n} \pi^{ij}\, \alpha_j\, \partial_i.$$

□

Theorem 24. *Let (M,ω) be a symplectic $2n$-dimensional manifold and let $p \in M$. Then there exist an open neighbourhood $U \subset M$ of p and a chart*

$$(U,(q^1,\dots,q^n,p_1,\dots,p_n))$$

such that, on U,

$$\omega = \sum_{i=1}^{n} dq^i \wedge dp_i.$$

The coordinates $(q^1,\dots,q^n,p_1,\dots,p_n)$ are called Darboux coordinates for ω on U.

Definition 25. Let (M,ω) be a symplectic $2n$-dimensional manifold and let $f \in C^\infty(M)$ be a smooth function. The vector field associated to f is the unique vector field $X_f \in \mathfrak{X}(M)$ defined by

$$\omega^\flat(X_f) = df,$$

or equivalently

$$X_f := \omega^\sharp(df).$$

In local coordinates $(U,(x^1,\dots,x^{2n}))$

$$df\big|_U = \sum_{j=1}^{2n} \frac{\partial f}{\partial x^j}\, dx^j.$$

Then on U the vector field has the coordinate expression

$$X_f\big|_U = \omega^\sharp(df\big|_U) = \sum_{i=1}^{2n}\sum_{j=1}^{2n} \pi^{ij}\,\frac{\partial f}{\partial x^j}\,\partial_i,$$

where the functions $\pi^{ij} \in C^\infty(U)$ are those from Theorem 16.

Definition 26. Let (M,ω) be a symplectic $2n$-dimensional manifold and let $f,g \in C^\infty(M)$. The Poisson bracket of f and g is the smooth function $\{f,g\} : M \to \mathbb{R}$ defined by

$$\{f,g\} := \omega(X_f, X_g).$$

In local coordinates $(U,(x^1,\dots,x^{2n}))$ as in Theorem 16, using

$$X_f = \sum_{i=1}^{2n}\sum_{j=1}^{2n} \pi^{ij}\,\frac{\partial f}{\partial x^j}\,\partial_i, \quad X_g = \sum_{k=1}^{2n}\sum_{\ell=1}^{2n} \pi^{k\ell}\,\frac{\partial g}{\partial x^\ell}\,\partial_k,$$

one obtains on U the coordinate expression

$$\{f,g\} = \sum_{i=1}^{2n}\sum_{j=1}^{2n} \pi^{ij}\,\frac{\partial f}{\partial x^i}\,\frac{\partial g}{\partial x^j}.$$

For all $f,g,h \in C^\infty(M)$ and $\lambda,\mu \in \mathbb{R}$, the Poisson bracket satisfies:

(i) Bilinearity: $\{\lambda f + \mu g,\, h\} = \lambda\{f,h\} + \mu\{g,h\}$,
$\{f,\, \lambda g + \mu h\} = \lambda\{f,g\} + \mu\{f,h\}$,

(ii) Antisymmetry: $\{f,g\} = -\{g,f\}$,

(iii) Leibniz rule: $\{f,gh\} = \{f,g\}\,h + g\,\{f,h\}$,

(iv) Jacobi identity: $\{f,\{g,h\}\} + \{g,\{h,f\}\} + \{h,\{f,g\}\} = 0.$

A

Definition 27. Let (M, ω) be a symplectic manifold and let $H \in C^\infty(M)$ be a (time-independent) Hamiltonian function. The triple (M, ω, H) is called a Hamiltonian system. The Hamiltonian vector field $X_H \in \mathfrak{X}(M)$ associated to H is defined by

$$X_H := \omega^\sharp(dH).$$

An observable is a smooth function $f \in C^\infty(M)$. Its time evolution under the Hamiltonian system (M, ω, H) is defined by

$$\frac{d}{dt} f := X_H(f) = df(X_H) = \omega(X_f, X_H) = \{f, H\}.$$

Definition 28. Let M and N be smooth manifolds. A map $F : M \to N$ is called a diffeomorphism if it is smooth, a bijection and its inverse map F^{-1} is also smooth.

Definition 29. Let (M, ω) be a symplectic manifold and let $H \in C^\infty(M)$ be a (time-independent) Hamiltonian. The associated Hamiltonian vector field $X_H \in \mathfrak{X}(M)$ is

$$X_H := \omega^\sharp(dH).$$

A flow on X_H is defined as the smooth map

$$\varphi : I \times U \to M, \qquad (t, p) \mapsto \varphi_t(p),$$

where $I \subset \mathbb{R}$ is an interval containing 0 and $U \subset M$ is open, such that for every $p \in U$:

$$\frac{d}{dt}\varphi_t(p) = X_H\big(\varphi_t(p)\big), \qquad \varphi_0(p) = p.$$

For each fixed time $t \in \mathbb{R}$, the map φ_t moves each initial condition p along its trajectory to the point $\varphi_t(p)$. For each fixed $t \in I$, the map $\varphi_t : U \to \varphi_t(U) \subset M$ is a diffeomorphism. The family $\{\varphi_t\}_{t \in I}$ is called the Hamiltonian flow of H.

The differential (or derivative) of the flow at p is the linear map

$$(d\varphi_t)_p : T_pM \to T_{\varphi_t(p)}M$$

given by the first–order (linear) approximation of φ_t near p. Intuitively, a tangent vector $v \in T_pM$ represents an infinitesimal perturbation of the initial condition p, and $(d\varphi_t)_p(v)$ is the corresponding infinitesimal perturbation of the state $\varphi_t(p)$ at time t. A standard property of flows of vector fields is

$$(d\varphi_t)_p\big(X_H(p)\big) = X_H\big(\varphi_t(p)\big), \qquad t \in \mathbb{R}.$$

Definition 30. Let $F : M \to N$ be a smooth map between smooth manifolds, and let $\alpha \in \Omega^k(N)$ be a smooth k-form on N. The pullback of α by F is the k-form $F^*\alpha \in \Omega^k(M)$ defined by

$$(F^*\alpha)_p(v_1, \ldots, v_k) := \alpha_{F(p)}\big((dF)_p(v_1), \ldots, (dF)_p(v_k)\big),$$

for $p \in M$ and $v_1, \ldots, v_k \in T_pM$, where $(dF)_p : T_pM \to T_{F(p)}N$ is the differential of F at p.

Definition 31. Let $X \in \mathfrak{X}(M)$ be a smooth vector field and $\alpha \in \Omega^k(M)$ a k-form with $k \geq 1$. The interior product $i_X\alpha \in \Omega^{k-1}(M)$ is defined by

$$(i_X\alpha)(X_1, \ldots, X_{k-1}) := \alpha(X, X_1, \ldots, X_{k-1}), \qquad X_1, \ldots, X_{k-1} \in \mathfrak{X}(M).$$

For $k = 0$ we set $i_X\alpha := 0$.

The Lie derivative of differential forms along X is the operator $L_X : \Omega^k(M) \to \Omega^k(M)$ defined by Cartan's formula

$$L_X\alpha := d(i_X\alpha) + i_X(d\alpha).$$

Theorem 32. *Let (M, ω, H) be a Hamiltonian system with Hamiltonian flow $\{\varphi_t\}_{t\in I}$ generated by $X_H = \omega^\sharp(dH)$. Then for all $t \in I$,*

$$\varphi_t^*\omega = \omega.$$

In other words, the Hamiltonian flow φ_t preserves the symplectic form ω.

Proof. We first compute the Lie derivative of ω along X_H. By definition of X_H we have

$$i_{X_H}\omega = dH,$$

since $\omega^\flat(X_H) = dH$ and $\omega^\flat(X_H)(\cdot) = \omega(X_H, \cdot)$. Using Cartan's formula and the fact that $d \circ d = 0$ and $d\omega = 0$ (closedness of the symplectic form),

$$L_{X_H}\omega = d(i_{X_H}\omega) + i_{X_H}(d\omega) = d(dH) + i_{X_H}(0) = 0.$$

Let φ_t be the flow of X_H as in Definition 29. A standard result is

$$\frac{d}{dt}\,\varphi_t^*\alpha = \varphi_t^*(L_{X_H}\alpha)$$

for any differential form α. Applying this to $\alpha = \omega$, we obtain

$$\frac{d}{dt}\,\varphi_t^*\omega = \varphi_t^*(L_{X_H}\omega) = \varphi_t^*(0) = 0.$$

Hence $\varphi_t^*\omega$ is independent of t. At $t = 0$ we have $\varphi_0 = \mathrm{id}_M$, so

$$\varphi_0^*\omega = \mathrm{id}_M^*\omega = \omega.$$

Therefore $\varphi_t^*\omega = \omega$ for all $t \in I$, as claimed. □

Theorem 33. *Let (M, ω, H) be a $2n$-dimensional Hamiltonian system. Define the Liouville volume form*

$$\Omega := \frac{1}{n!}\,\omega^{\wedge n} = \frac{1}{n!}\,\underbrace{\omega \wedge \cdots \wedge \omega}_{n \text{ times}} \in \Omega^{2n}(M).$$

Let $\{\varphi_t\}$ be the Hamiltonian flow of H. For any measurable domain $D \subset M$ with compact closure,

$$\int_{\varphi_t(D)} \Omega = \int_D \Omega,$$

so the Hamiltonian flow preserves phase-space volume.

Proof. By Theorem 24 we have $\varphi_t^*\omega = \omega$ for all t. Using the properties of the pullback and the wedge product,

$$\varphi_t^*\Omega = \varphi_t^*\Big(\frac{1}{n!}\,\omega^{\wedge n}\Big) = \frac{1}{n!}\,\varphi_t^*(\omega^{\wedge n}) = \frac{1}{n!}\,\omega^{\wedge n} = \Omega.$$

Since Ω is a form of degree $2n$, it defines a volume form on M. For any measurable domain $D \subset M$ with compact closure, the change-of-variables formula for integrals under diffeomorphisms gives

$$\int_{\varphi_t(D)} \Omega = \int_D \varphi_t^* \Omega = \int_D \Omega.$$

Thus the Hamiltonian flow preserves the Liouville volume, proving Liouville's theorem. □

A.3. LYAPUNOV'S EXPONENTS

Definition 34. Let $\varphi_t : M \to M$ be a measurable flow. A Borel probability measure μ on M is invariant under φ_t if

$$\mu(\varphi_t^{-1}(B)) = \mu(B) \quad \text{for all Borel sets } B \subset M \text{ and all } t \in \mathbb{R},$$

equivalently,

$$\int_M f \circ \varphi_t \, d\mu = \int_M f \, d\mu \quad \text{for all } f \in L^1(M, \mu),\ t \in \mathbb{R}.$$

For a Hamiltonian system (M, ω, H), the Liouville measure associated to the volume form

$$\Omega := \frac{1}{n!} \omega^{\wedge n} \in \Omega^{2n}(M)$$

is invariant by Liouville's theorem, and can be normalized to a probability measure on any invariant set of finite volume.

Theorem 35. **[Via14, Theorem 4.2]** *Let (M, ω, H) be a $2n$-dimensional Hamiltonian system with Hamiltonian flow $\{\varphi_t\}$, and let μ be the associated Liouville measure and g a chosen Riemannian metric. Then there exists a φ_t-invariant Borel set $M_0 \subset M$ with $\mu(M_0) = 1$ such that for each $p \in M_0$ there exist:*

1. *unique real numbers*

$$\lambda_1(p) > \lambda_2(p) > \cdots > \lambda_{k(p)}(p),$$

called the Lyapunov's exponents at p, and

2. *a direct sum decomposition*

$$T_pM = E_1(p) \oplus \cdots \oplus E_{k(p)}(p),$$

with the following properties:

1. *Invariance:*

$$(d\varphi_t)_p\big(E_i(p)\big) = E_i\big(\varphi_t(p)\big) \quad \text{for all } t \in \mathbb{R},\ i = 1, \ldots, k(p).$$

2. *Exponential growth rates: for every $0 \neq v \in E_i(p)$,*

$$\lambda_i(p) = \lim_{t \to \infty} \frac{1}{t} \log\big(||(d\varphi_t)_p(v)||\big),$$

where the norm is induced by the Riemannian metric g.

If moreover μ is ergodic, then the numbers $k(p)$ and $\lambda_i(p)$ are constant for μ-almost every p; in this case we simply write $\lambda_1 > \cdots > \lambda_k$ for the Lyapunov spectrum of (M, ω, H, μ).

Theorem 36. [Via14, Proposition 4.17] *Let (M, ω, H) be a $2n$-dimensional Hamiltonian system with Hamiltonian $H \in C^2$, Hamiltonian flow $\{\varphi_t\}$ and Liouville volume form Ω. Let μ be the associated Liouville probability measure and let $M_0 \subset M$ be the full μ-measure set given by Theorem 35. For $p \in M_0$, let*

$$T_pM = E_1(p) \oplus \cdots \oplus E_{k(p)}(p)$$

be the Oseledets splitting with Lyapunov's exponents $\lambda_1(p) > \cdots > \lambda_{k(p)}(p)$. Listing these exponents with multiplicities $\dim E_i(p)$,

$$\underbrace{\lambda_1(p), \ldots, \lambda_1(p)}_{\dim E_1(p) \text{ times}}, \quad \ldots, \quad \underbrace{\lambda_{k(p)}(p), \ldots, \lambda_{k(p)}(p) \text{ times}}_{},$$

we obtain $2n$ real numbers which we denote by $\lambda_1^*(p), \ldots, \lambda_{2n}^*(p)$. Then for μ-almost every $p \in M$,

$$\sum_{i=1}^{2n} \lambda_i^*(p) = 0.$$

Proof. We provide a self-contained proof of this statement. Fix $p \in M_0$. Choose a basis

$$\{v_1, \ldots, v_{2n}\}$$

of T_pM such that each v_j lies in some Oseledets subspace $E_i(p)$. Thus there exist indices $i(1), \ldots, i(2n) \in \{1, \ldots, k(p)\}$ such that $v_j \in E_{i(j)}(p)$ and the Lyapunov's exponent of v_j is $\lambda_{i(j)}(p)$. By construction,

$$\lambda_1^*(p), \ldots, \lambda_{2n}^*(p)$$

is exactly the list

$$\lambda_{i(1)}(p), \ldots, \lambda_{i(2n)}(p),$$

so it suffices to show that

$$\sum_{j=1}^{2n} \lambda_{i(j)}(p) = 0.$$

Choose an inner product $\langle \cdot, \cdot \rangle_q$ on each tangent space T_qM such that the associated Riemannian volume form on T_qM coincides with Ω_q. Let $|| \cdot ||_q$ denote the corresponding norm on T_qM. For $w_1, \ldots, w_{2n} \in T_qM$, let

$$\mathrm{Vol}_q(w_1, \ldots, w_{2n})$$

denote the Riemannian volume of the parallelepiped they span. By construction,

$$\mathrm{Vol}_q(w_1, \ldots, w_{2n}) = \left|\Omega_q(w_1, \ldots, w_{2n})\right|.$$

Moreover, in any Euclidean space one has the standard inequality for the volume of a parallelepiped,

$$\mathrm{Vol}_q(w_1, \ldots, w_{2n}) \leq \prod_{j=1}^{2n} ||w_j||_q,$$

with constant 1 (this follows from the Gram determinant formula). For $t > 0$, set

$$w_j(t) := (d\varphi_t)_p(v_j) \in T_{\varphi_t(p)}M, \qquad j = 1, \ldots, 2n,$$

A

and define

$$V(t) := \mathrm{Vol}_{\varphi_t(p)}\big(w_1(t), \dots, w_{2n}(t)\big) = \big|\Omega_{\varphi_t(p)}\big((d\varphi_t)_p(v_1), \dots, (d\varphi_t)_p(v_{2n})\big)\big|.$$

By Theorem 29, for each j,

$$\lambda_{i(j)}(p) = \lim_{t\to+\infty} \frac{1}{t} \log ||(d\varphi_t)_p(v_j)||_{\varphi_t(p)}.$$

Hence for every $\varepsilon > 0$ there exists $T_\varepsilon > 0$ such that for all $t \geq T_\varepsilon$ and all j,

$$||(d\varphi_t)_p(v_j)||_{\varphi_t(p)} \leq e^{(\lambda_{i(j)}(p)+\varepsilon)t}.$$

Using the volume inequality for a parallelepiped, for $t \geq T_\varepsilon$ we obtain

$$V(t) \leq \prod_{j=1}^{2n} ||(d\varphi_t)_p(v_j)||_{\varphi_t(p)} \leq \prod_{j=1}^{2n} e^{(\lambda_{i(j)}(p)+\varepsilon)t} = \exp\Big(\big(\sum_{j=1}^{2n} \lambda_{i(j)}(p) + 2n\varepsilon\big)t\Big).$$

On the other hand, by Theorem 32 we have $\varphi_t^*\Omega = \Omega$ for all t, hence

$$\begin{aligned} V(t) &= \big|\Omega_{\varphi_t(p)}\big((d\varphi_t)_p(v_1), \dots, (d\varphi_t)_p(v_{2n})\big)\big| \\ &= \big|(\varphi_t^*\Omega)_p(v_1, \dots, v_{2n})\big| = \big|\Omega_p(v_1, \dots, v_{2n})\big| =: V_0 > 0, \end{aligned}$$

so $V(t)$ is actually independent of t. Thus for all $t \geq T_\varepsilon$,

$$V_0 \leq \exp\Big(\big(\sum_{j=1}^{2n} \lambda_{i(j)}(p) + 2n\varepsilon\big)t\Big).$$

Taking logarithms and dividing by t,

$$\frac{1}{t} \log V_0 \leq \sum_{j=1}^{2n} \lambda_{i(j)}(p) + 2n\varepsilon.$$

Letting $t \to \infty$ we obtain

$$0 \leq \sum_{j=1}^{2n} \lambda_{i(j)}(p) + 2n\varepsilon.$$

Since $\varepsilon > 0$ is arbitrary, this implies

$$\sum_{j=1}^{2n} \lambda_{i(j)}(p) \geq 0.$$

Consider now the reversed flow

$$\psi_t := \varphi_{-t}, \qquad t \in \mathbb{R}.$$

Its derivative at p is

$$(d\psi_t)_p = (d\varphi_{-t})_p.$$

For $t > 0$ define

$$\widetilde{w}_j(t) := (d\psi_t)_p(v_j) = (d\varphi_{-t})_p(v_j), \qquad j = 1, \dots, 2n,$$

and

$$\widetilde{V}(t) := \mathrm{Vol}_{\psi_t(p)}\big(\widetilde{w}_1(t), \dots, \widetilde{w}_{2n}(t)\big) = \big|\Omega_{\psi_t(p)}\big((d\psi_t)_p(v_1), \dots, (d\psi_t)_p(v_{2n})\big)\big|.$$

By Theorem 29 for the original flow $\{\varphi_t\}$, for $v_j \in E_{i(j)}(p)$ we have

$$\lambda_{i(j)}(p) = \lim_{s\to-\infty} \frac{1}{s} \log ||(d\varphi_s)_p(v_j)||.$$

Setting $s = -t$ with $t > 0$, this gives

$$\lambda_{i(j)}(p) = \lim_{t\to+\infty} \frac{1}{-t} \log ||(d\varphi_{-t})_p(v_j)|| = -\lim_{t\to+\infty} \frac{1}{t} \log ||(d\psi_t)_p(v_j)||.$$

Thus, for the reversed flow ψ_t, the Lyapunov's exponent of v_j is $-\lambda_{i(j)}(p)$, and as before this implies that for every $\varepsilon > 0$ there exists $T'_\varepsilon > 0$ such that for all $t \geq T'_\varepsilon$ and all j,

$$||(d\psi_t)_p(v_j)||_{\psi_t(p)} \leq e^{(-\lambda_{i(j)}(p)+\varepsilon)t}.$$

Using again the volume inequality for a parallelepiped, for $t \geq T'_\varepsilon$,

$$\widetilde{V}(t) \leq \prod_{j=1}^{2n} ||(d\psi_t)_p(v_j)||_{\psi_t(p)} \leq \prod_{j=1}^{2n} e^{(-\lambda_{i(j)}(p)+\varepsilon)t} = \exp\Big(\big(-\sum_{j=1}^{2n} \lambda_{i(j)}(p) + 2n\varepsilon\big)t\Big).$$

On the other hand, since $\psi_t = \varphi_{-t}$ and $\varphi_t^* \Omega = \Omega$ for all t, we also have $\psi_t^* \Omega = \Omega$ for all t, hence

$$\begin{aligned}\widetilde{V}(t) &= \big|\Omega_{\psi_t(p)}\big((d\psi_t)_p(v_1), \ldots, (d\psi_t)_p(v_{2n})\big)\big| \\ &= \big|(\psi_t^* \Omega)_p(v_1, \ldots, v_{2n})\big| = \big|\Omega_p(v_1, \ldots, v_{2n})\big| = V_0.\end{aligned}$$

Thus for all $t \geq T'_\varepsilon$,

$$V_0 \leq \exp\Big(\big(-\sum_{j=1}^{2n} \lambda_{i(j)}(p) + 2n\varepsilon\big)t\Big).$$

Taking logarithms and dividing by t,

$$\frac{1}{t} \log V_0 \leq -\sum_{j=1}^{2n} \lambda_{i(j)}(p) + 2n\varepsilon.$$

Letting $t \to \infty$ gives

$$0 \leq -\sum_{j=1}^{2n} \lambda_{i(j)}(p) + 2n\varepsilon,$$

hence

$$\sum_{j=1}^{2n} \lambda_{i(j)}(p) \leq 0$$

since $\varepsilon > 0$ was arbitrary. Combining the inequalities obtained thus far yields

$$0 \leq \sum_{j=1}^{2n} \lambda_{i(j)}(p) \leq 0,$$

so $\sum_{j=1}^{2n} \lambda_{i(j)}(p)) = 0$. This holds for every $p \in M_0$, hence for μ-almost every $p \in M$. □

Lemma 37. **[Via, Proposition 0.6.]** *Let (M, ω, H) be a $2n$-dimensional Hamiltonian system with Hamiltonian flow $\{\varphi_t\}$ and Liouville probability measure μ,*

A

and let $M_0 \subset M$ be the full μ-measure set given by Theorem 29. For $p \in M_0$ and for each Lyapunov's exponent $\lambda_i(p)$, define

$$E_\lambda(p) := \bigoplus_{\{i:\, \lambda_i(p)=\lambda\}} E_i(p).$$

Then for μ-almost every $p \in M$ the following holds: if $\lambda + \mu \neq 0$, then

$$\omega_p\big(E_\lambda(p), E_\mu(p)\big) = 0,$$

i.e. $\omega_p(v, w) = 0$ for all $v \in E_\lambda(p)$ and $w \in E_\mu(p)$.

Proof. Fix $p \in M_0$ and let λ, μ be Lyapunov's exponents at p. Choose nonzero vectors $v \in E_\lambda(p)$ and $w \in E_\mu(p)$. We claim that

$$\omega_p(v, w) \neq 0 \implies \lambda + \mu = 0.$$

This will imply the statement by contraposition.

By Theorem 32 we have $\varphi_t^* \omega = \omega$ for all t, so for every $t \in \mathbb{R}$,

$$\omega_p(v, w) = \omega_{\varphi_t(p)}\big((d\varphi_t)_p(v), (d\varphi_t)_p(w)\big). \tag{A.2}$$

Choose an inner product $\langle \cdot, \cdot \rangle_q$ on each tangent space T_qM such that the associated Riemannian volume form on T_qM coincides with the Liouville volume form Ω_q. Let $\|\cdot\|_q$ denote the corresponding norm on T_qM. Since ω is a smooth bilinear form on the finite-dimensional bundle TM, there exists a finite constant $C > 0$ such that for all $q \in M$ and $u_1, u_2 \in T_qM$,

$$|\omega_q(u_1, u_2)| \leq C \|u_1\| \|u_2\|. \tag{A.3}$$

Assume $\omega_p(v, w) \neq 0$. Using (A.2) and (A.3) for $t > 0$ we obtain

$$|\omega_p(v, w)| \leq C \|(d\varphi_t)_p(v)\| \|(d\varphi_t)_p(w)\|.$$

Taking logarithms and dividing by $t > 0$ gives

$$\frac{1}{t} \log |\omega_p(v, w)| \leq \frac{1}{t} \log C + \frac{1}{t} \log \|(d\varphi_t)_p(v)\| + \frac{1}{t} \log \|(d\varphi_t)_p(w)\|.$$

Letting $t \to \infty$ and using Theorem 35 we get

$$0 \leq \lambda + \mu.$$

Now consider the reversed flow $\psi_t := \varphi_{-t}$, which is also a measurable flow preserving μ. Applying Theorem 35 to $\{\psi_t\}$, the Lyapunov's exponent of v for ψ_t is $-\lambda$, and similarly the Lyapunov's exponent of w is $-\mu$. Thus

$$-\lambda = \lim_{s \to \infty} \frac{1}{s} \log \|(d\psi_s)_p(v)\| = \lim_{s \to \infty} \frac{1}{s} \log \|(d\varphi_{-s})_p(v)\|,$$

and analogously

$$-\mu = \lim_{s \to \infty} \frac{1}{s} \log \|(d\varphi_{-s})_p(w)\|.$$

Using (A.2) with $t = -s$ and (A.3) we obtain, for $s > 0$,

$$|\omega_p(v, w)| = \big|\omega_{\varphi_{-s}(p)}\big((d\varphi_{-s})_p(v), (d\varphi_{-s})_p(w)\big)\big| \leq C \|(d\varphi_{-s})_p(v)\| \|(d\varphi_{-s})_p(w)\|.$$

Taking logarithms and dividing by $s > 0$ yields

$$\frac{1}{s} \log |\omega_p(v, w)| \leq \frac{1}{s} \log C + \frac{1}{s} \log \|(d\varphi_{-s})_p(v)\| + \frac{1}{s} \log \|(d\varphi_{-s})_p(w)\|.$$

Letting $s \to \infty$ and using the limits above, we obtain

$$0 \leq -\lambda - \mu.$$

Combining the two inequalities gives $\lambda + \mu \geq 0$ and $\lambda + \mu \leq 0$, hence $\lambda + \mu = 0$, as claimed. Thus, if $\lambda + \mu \neq 0$ then necessarily $\omega_p(v, w) = 0$ for all $v \in E_\lambda(p)$ and $w \in E_\mu(p)$. □

Lemma 38. [Fis08, Theorem 1.1] *With notation as in Lemma 37, for every $\lambda > 0$ the restriction of ω_p to $E_\lambda(p) \oplus E_{-\lambda}(p)$ is nondegenerate, and*

$$\dim E_\lambda(p) = \dim E_{-\lambda}(p)$$

for μ-almost every $p \in M$.

Proof. Fix $p \in M_0$ and $\lambda > 0$, and consider the bilinear map

$$B_\lambda : E_\lambda(p) \times E_{-\lambda}(p) \to \mathbb{R}, \qquad B_\lambda(v, w) := \omega_p(v, w).$$

By Lemma 37, if $\mu \neq -\lambda$ then $\omega_p\big(E_\lambda(p), E_\mu(p)\big) = 0$, so $\omega_p(v, \cdot)$ can only be nonzero on $E_{-\lambda}(p)$.

First we show that B_λ is nondegenerate in the first argument. Let $v \in E_\lambda(p)$ and suppose $\omega_p(v, w) = 0$ for all $w \in E_{-\lambda}(p)$. For any $w \in T_pM$ write

$$w = \sum_\mu w_\mu, \qquad w_\mu \in E_\mu(p).$$

Then by bilinearity and Lemma 37,

$$\omega_p(v, w) = \sum_\mu \omega_p(v, w_\mu) = \omega_p(v, w_{-\lambda}),$$

which is zero by assumption. Hence $\omega_p(v, w) = 0$ for all $w \in T_pM$. Since ω_p is nondegenerate, this implies $v = 0$. Thus B_λ is nondegenerate in the first argument.

The same argument, exchanging the roles of λ and $-\lambda$, shows that B_λ is also nondegenerate in the second argument.

Now consider the linear map

$$T : E_\lambda(p) \to E_{-\lambda}(p)^*, \qquad T(v)(w) := \omega_p(v, w).$$

Bilinearity of B_λ in the first argument implies that T is linear. Nondegeneracy in the first argument shows that T is injective: indeed, if $T(v) = 0$, then $T(v)(w) = \omega_p(v, w) = 0$ for all $w \in E_{-\lambda}(p)$, and the argument above implies $v = 0$, thus $\ker(T) = \{0\}$.

Similarly, define

$$S : E_{-\lambda}(p) \to E_\lambda(p)^*, \qquad S(w)(v) := \omega_p(v, w).$$

This map is linear because B_λ is linear in the second argument. Nondegeneracy of B_λ in the second argument implies that S is injective: if $S(w) = 0$, then

$$\omega_p(v, w) = S(w)(v) = 0 \quad \text{for all } v \in E_\lambda(p),$$

and nondegeneracy in the second argument yields $w = 0$, thus $\ker(S) = \{0\}$.

Since $E_\lambda(p)$ and $E_{-\lambda}(p)$ are finite-dimensional vector spaces, using the rank–nullity theorem and the injectivity of T gives

$$\dim E_\lambda(p) \leq \dim E_{-\lambda}(p)^* = \dim E_{-\lambda}(p),$$

and injectivity of S gives

$$\dim E_{-\lambda}(p) \le \dim E_\lambda(p)^* = \dim E_\lambda(p).$$

Combining these inequalities we obtain

$$\dim E_\lambda(p) = \dim E_{-\lambda}(p).$$

□

Lemma 39. *With notation as in Lemma 37, the restriction of ω_p to $E_0(p)$ is nondegenerate for μ-almost every $p \in M$. In particular, $\dim E_0(p)$ is even.*

Proof. Fix $p \in M_0$ and let $\lambda = 0$. By Lemma 37 we have $\omega_p\big(E_0(p), E_\mu(p)\big) = 0$ whenever $\mu \neq 0$, so $\omega_p(v, \cdot)$ can only be nonzero on $E_0(p)$.

If $v \in E_0(p)$ satisfies $\omega_p(v, w) = 0$ for all $w \in E_0(p)$, then for any $w \in T_pM$ written as

$$w = \sum_\mu w_\mu, \qquad w_\mu \in E_\mu(p),$$

we have, using Lemma 38,

$$\omega_p(v, w) = \sum_\mu \omega_p(v, w_\mu) = \omega_p(v, w_0) = 0.$$

Thus $\omega_p(v, w) = 0$ for all $w \in T_pM$, and by nondegeneracy of ω_p we obtain $v = 0$. Hence the restriction of ω_p to $E_0(p)$ is nondegenerate, so $E_0(p)$ is a symplectic subspace of T_pM. In particular, $\dim E_0(p)$ is even.

□

Theorem 40. *Let (M, ω, H) be a $2n$-dimensional Hamiltonian system with Hamiltonian flow $\{\varphi_t\}$ and Liouville probability measure μ, and let $M_0 \subset M$ be the full μ-measure set given by Theorem 29. For $p \in M_0$ and for each Lyapunov's exponent $\lambda_i(p)$, define*

$$E_\lambda(p) := \bigoplus_{\{i:\, \lambda_i(p) = \lambda\}} E_i(p),$$

with the convention $E_\lambda(p) = \{0\}$ if λ does not occur. Then for μ-almost every $p \in M$ the Lyapunov's exponents come in pairs $\lambda, -\lambda$, and the multiplicity of 0 is even, in the following sense: if we list the Lyapunov's exponents at p with multiplicities as in Theorem 30,

$$\lambda_1^*(p), \dots, \lambda_{2n}^*(p),$$

then for every $\lambda \in \mathbb{R}$ the number of indices i with $\lambda_i^*(p) = \lambda$ equals the number of indices i with $\lambda_i^*(p) = -\lambda$, and the number of indices with $\lambda_i^*(p) = 0$ is even.

Proof. Fix $p \in M_0$. By Lemma 38, for every $\lambda > 0$ the restriction of ω_p to $E_\lambda(p) \oplus E_{-\lambda}(p)$ is nondegenerate and

$$\dim E_\lambda(p) = \dim E_{-\lambda}(p).$$

Thus each positive exponent λ occurs with the same multiplicity as $-\lambda$.

By Lemma 39, the restriction of ω_p to $E_0(p)$ is nondegenerate, so $E_0(p)$ is symplectic and $\dim E_0(p)$ is even. This means that 0 appears with even multiplicity in the Lyapunov spectrum.

Listing the exponents with multiplicities as in Theorem 30 and using these facts yields exactly the stated pairing of Lyapunov's exponents.

□

Theorem 41. *Let (M_0, ω, H) be a $2n$-dimensional Hamiltonian system with Hamiltonian flow $\{\varphi_t\}$ and Liouville probability measure μ. Assume that $E \in \mathbb{R}$ is a chosen value of H, so that the energy level*

$$\Sigma_E := H^{-1}(E)$$

is a smooth $(2n-1)$-dimensional submanifold of M_0, and suppose that Σ_E is compact. Then for μ-almost every $p \in \Sigma_E$ the Lyapunov spectrum of the Hamiltonian flow at p has at least two zero Lyapunov's exponents.

Proof. We provide a self-contained proof of this statement. By Definition 27,

$$\frac{d}{dt} H = \{H, H\} = 0,$$

so $H \circ \varphi_t = H$ for all $t \in \mathbb{R}$. In particular, if $p \in \Sigma_E$ then $H(\varphi_t(p)) = E$, so $\varphi_t(p) \in \Sigma_E$ for all t. Thus Σ_E is invariant under the flow.

Fix a Riemannian metric on M_0 and let $||\cdot||$ be the corresponding norm on tangent vectors. Since X_H is smooth (Definition 27 and the discussion before it) and Σ_E is compact, the function

$$F : \Sigma_E \to \mathbb{R}, \qquad F(q) := ||X_H(q)||$$

is continuous on a compact set, hence bounded above. Thus there exists $M < \infty$ such that

$$||X_H(q)|| \le M \qquad \text{for all } q \in \Sigma_E.$$

For $p \in M_0$ and $t \in \mathbb{R}$, recall that a property of the flow of a vector field is

$$(d\varphi_t)_p\big(X_H(p)\big) = X_H(\varphi_t(p)).$$

In particular, for all $t \ge 0$,

$$\big|\big|(d\varphi_t)_p(X_H(p))\big|\big| = ||X_H(\varphi_t(p))|| \le M.$$

Let $\lambda_H(p)$ denote the Lyapunov's exponent of $X_H(p)$ for the flow $\{\varphi_t\}$. By Theorem 35 this limit exists for μ-almost every p:

$$\lambda_H(p) := \lim_{t \to +\infty} \frac{1}{t} \log \big|\big|(d\varphi_t)_p(X_H(p))\big|\big|.$$

From the bound above we obtain, for all $t > 0$,

$$\frac{1}{t} \log \big|\big|(d\varphi_t)_p(X_H(p))\big|\big| \le \frac{1}{t} \log M,$$

hence letting $t \to \infty$ gives

$$\lambda_H(p) \le 0.$$

Now, consider the reversed flow

$$\psi_t := \varphi_{-t}, \qquad t \in \mathbb{R}.$$

The same argument as before shows that

$$\big|\big|(d\psi_t)_p(X_H(p))\big|\big| = ||X_H(\psi_t(p))|| \le M \qquad \text{for all } t \ge 0.$$

Let $-\lambda_H(p)$ be the Lyapunov's exponent of $X_H(p)$ for the reversed flow $\{\psi_t\}$:

$$-\lambda_H(p) := \lim_{t \to +\infty} \frac{1}{t} \log \big|\big|(d\psi_t)_p(X_H(p))\big|\big|.$$

From the same bound we obtain $-\lambda_H(p) \leq 0$. Together with $\lambda_H(p) \leq 0$ we conclude

$$\lambda_H(p) = 0 \qquad \text{for } \mu\text{-almost every } p \in \Sigma_E.$$

By Theorem 40, for μ-almost every $p \in M$ the Lyapunov's exponents come in pairs $\lambda, -\lambda$ and the multiplicity of 0 is even. Since we have just shown that 0 occurs at least once (because $X_H(p) \in E_0(p)$ is nonzero), it must in fact occur with multiplicity at least 2. Thus a $2n$-dimensional Hamiltonian system has at least two zero Lyapunov exponents at μ-almost every point $p \in \Sigma_E$. □

A.4. ADDITIONAL DATA / RESULTS

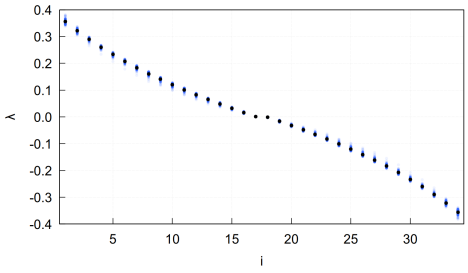

(a) Uniform, $\Gamma_{\max} = 1$ ($R = 0.5$).

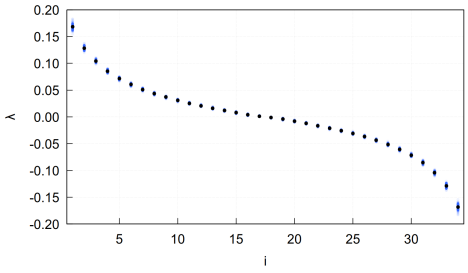

(b) $\Delta z = 0.01$, $\Gamma_{\max} = 1$ ($R = 0.5$).

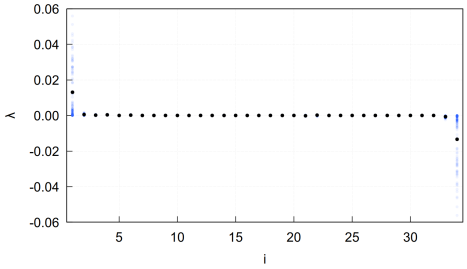

(c) $\Delta z = 0.01$, $\Gamma_{\max} = 4$ ($R = 0.2$).

Figure A.1.: Additional results associated with figure 5.14c. The Lyapunov's exponents are displayed for 100 trajectories (blue dots) from the uniform and z-focused ensemble and each exponent's average (black dot). The realization of disorder is #1. Chosen parameters are $N = 17$, $\Delta t = 10^{-3}$, $\tau = 500$, $\Delta_0 = 10^{-4}$ and $J_{\max} = 1$.

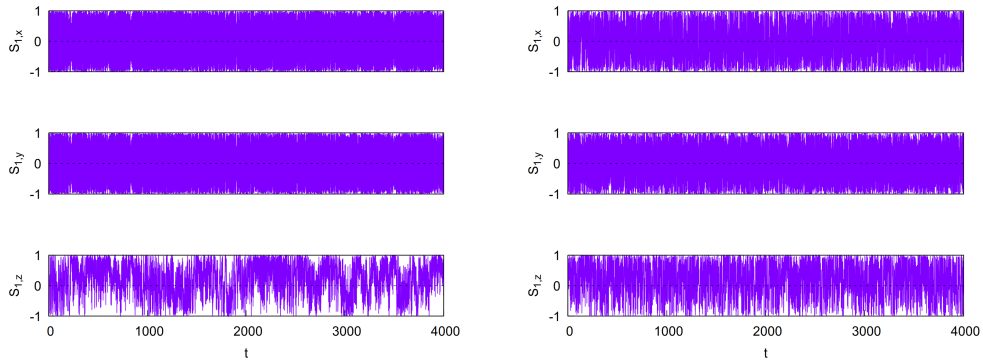

(a) Uniform, $\Gamma_{\max} = 4$ ($R = 0.2$). (b) Uniform, $\Gamma_{\max} = 1$ ($R = 0.5$).

Figure A.2.: Additional results associated with figure 5.12b. Spin coordinates of the first spin $\mathbf{S}_1$ over time are displayed for a trajectory from the uniform ensemble. Chosen parameters are $N = 17$, $\Delta t = 10^{-3}$, $\tau = 500$, $\Delta_0 = 10^{-4}$ and $J_{\max} = 1$.

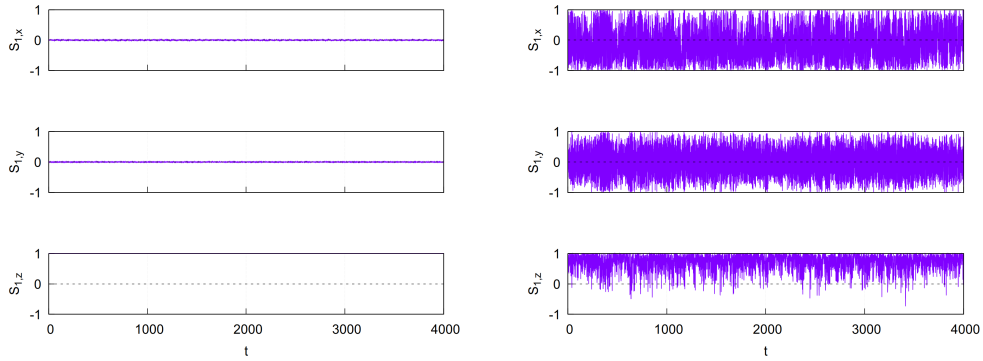

(a) $\Delta z = 0.01, \Gamma_{\max} = 4$ ($R = 0.2$). (b) $\Delta z = 0.01, \Gamma_{\max} = 1$ ($R = 0.5$).

Figure A.3.: Additional results associated with figure 5.13. Spin coordinates of the first spin $\mathbf{S}_1$ over time are displayed for a trajectory from the z-focused ensemble. Chosen parameters are $N = 17$, $\Delta t = 10^{-3}$, $\tau = 500$, $\Delta_0 = 10^{-4}$ and $J_{\max} = 1$.

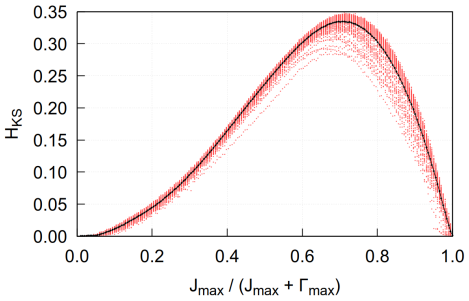

(a) Realization of disorder #2, uniform.

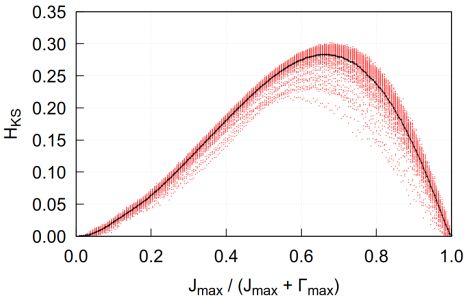

(b) Realization of disorder #3, uniform.

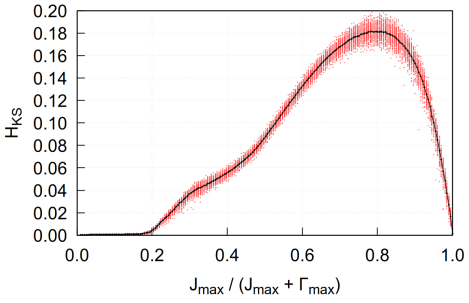

(c) Realization of disorder #2, $\Delta z = 0.05$.

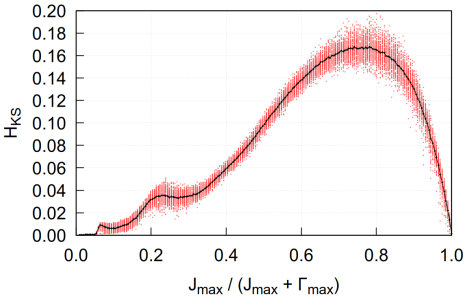

(d) Realization of disorder #3, $\Delta z = 0.05$.

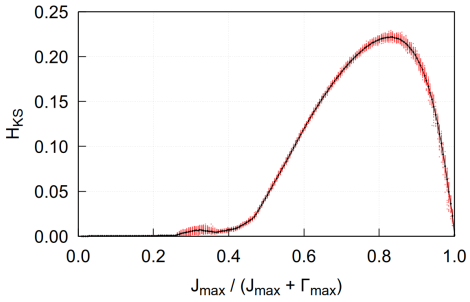

(e) Realization of disorder #1, $\Delta z = 0.01$.

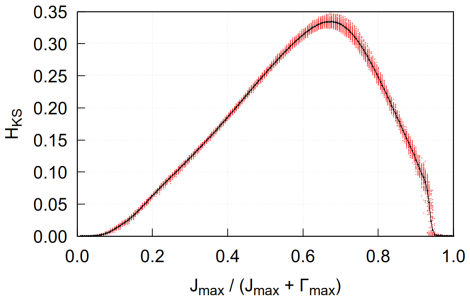

(f) Realization of disorder #1, $\Delta x = 0.01$.

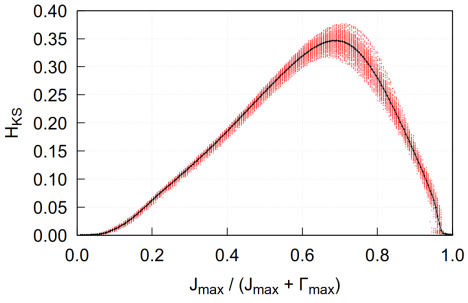

(g) Realization of disorder #1, $\Delta x = 0.10$.

Figure A.4.: Additional results associated with figures 5.16, 5.17 and 5.19. The Kolmogorov-Sinai entropy is displayed for 200 ratios of $J_{max}/(J_{max}+\Gamma_{max})$ (part 1).

Figure A.4.: The Kolmogorov-Sinai entropy for 200 ratios of $J_{max}/(J_{max} + \Gamma_{max})$ (continued). For each sampled ratio, 100 runs were executed (part 1). Each run was chosen from the x-focused ensemble. The realization of disorder for the chosen system is #1. Chosen parameters are $N = 17$, $T = 3 \cdot 10^4$, $\Delta t = 10^{-2}$, $\tau = 50$, $\Delta_0 = 10^{-4}$ and $J_{max} = 1$.

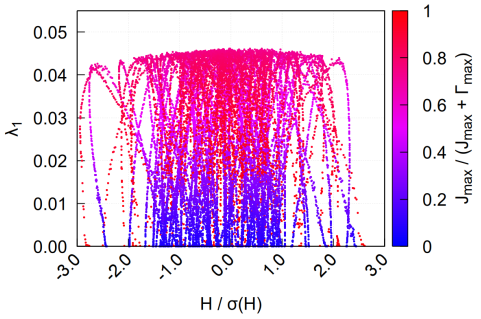

(a) Realization of disorder #2, uniform.

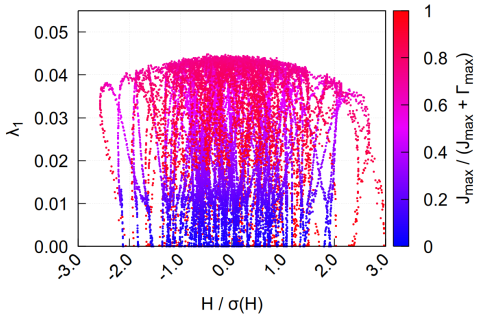

(b) Realization of disorder #3, uniform.

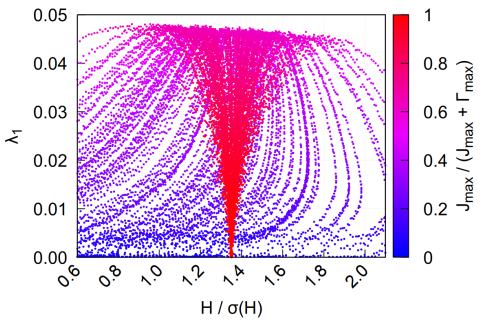

(c) Realization of disorder #1, $\Delta x = 0.05$.

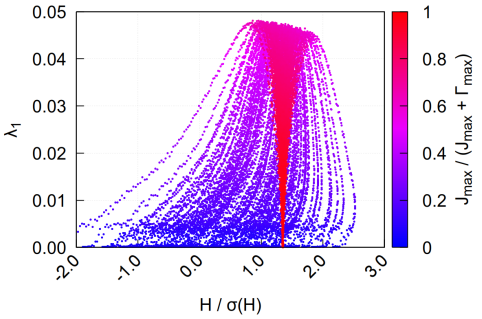

(d) Realization of disorder #1, $\Delta x = 0.05$. Zoomed out view of figure A.5c.

Figure A.5.: Additional results associated with figures 5.20 and 5.22. The maximum Lyapunov's exponent is displayed for various values of $H/\sigma(H)$. For each of the 200 sampled ratios $J_{max}/(J_{max} + \Gamma_{max})$ and ensemble choice, 100 runs were executed. Each run was chosen from the uniform. Chosen parameters are $N = 17$, $T = 3 \cdot 10^4$, $\Delta t = 10^{-2}$, $\tau = 50$, $\Delta_0 = 10^{-4}$ and $J_{max} = 1$.

A

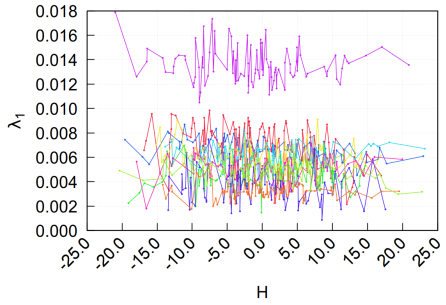

(a) $\Gamma_{max} = 5.66$ ($R = 0.15$).

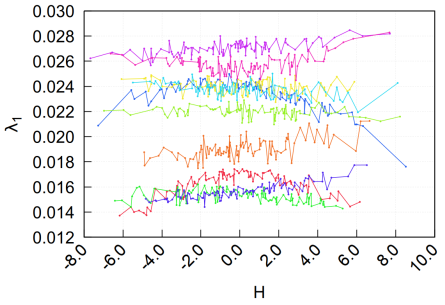

(b) $\Gamma_{max} = 2.03$ ($R = 0.33$).

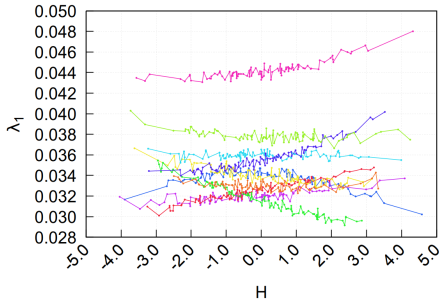

(c) $\Gamma_{max} = 1$ ($R = 0.5$).

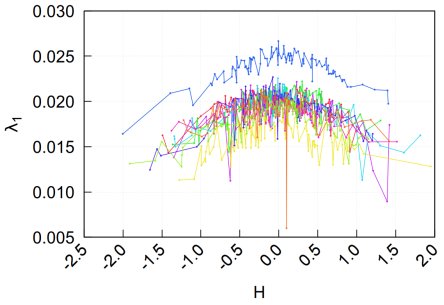

(d) $\Gamma_{max} = 0.0526$ ($R = 0.95$).

Figure A.6.: Additional results associated with figure 5.23. For multiple quenched realizations of disorder and values of H, the maximum Lyapunov's exponent is displayed. For each of the 10 shown realizations of disorder, shown in different colors, 100 runs were executed. Each run was chosen from the uniform ensemble. Chosen parameters are $N = 17$, $T = 3 \cdot 10^4$, $\Delta t = 10^{-2}$, $\tau = 50$, $\Delta_0 = 10^{-4}$, $J_{max} = 1$.